uOttawa

L'Université canadienne
Canada's university

FACULTÉ DES ÉTUDES SUPÉRIEURES ET POSTOCTORALES

uOttawa

L'Université canadienne
Canada's university

FACULTY OF GRADUATE AND POSDOCTORAL STUDIES

Julie Nkanta

AUTEUR DE LA THÈSE / AUTHOR OF THESIS

M.Sc. (Systems Science)

GRADE / DEGREE

School of Information Technology and Engineering

FACULTÉ, ÉCOLE, DÉPARTEMENT / FACULTY, SCHOOL, DEPARTMENT

Characterization and Simulations of Long Wavelength InAlGaAs/InP Lasers

TITRE DE LA THÈSE / TITLE OF THESIS

Trevor Hall

DIRECTEUR (DIRECTRICE) DE LA THÈSE / THESIS SUPERVISOR

Karin Hinzet

CO-DIRECTEUR (CO-DIRECTRICE) DE LA THÈSE / THESIS CO-SUPERVISOR

EXAMINATEURS (EXAMINATRICES) DE LA THÈSE / THESIS EXAMINERS

Dr. Henry Schriemer

Dr. Voicu Groza

Gary W. Slater

Le Doyen de la Faculté des études supérieures et postdoctorales / Dean of the Faculty of Graduate and Postdoctoral Studies

Characterization and Simulations of Long Wavelength InAlGaAs/InP Lasers

Julie Nkanta

Thesis submitted to the Faculty of Graduate and Postdoctoral Studies in partial fulfillment of the requirements for the M.Sc degree in Systems Science

September 2008

Systems Science Program
School of Information Technology and Engineering
University of Ottawa

Your file Votre référence
ISBN: 978-0-494-46491-5
Our file Notre référence
ISBN: 978-0-494-46491-5

Abstract

This thesis studies the characterization and simulation of long wavelength indium aluminium gallium arsenide (InAlGaAs) lattice-matched to indium phosphide (InP) diode laser, emitting between 1.648 to 1.7 μm in wavelength. The active region of one laser diode sample consists of six $In_{0.69}Ga_{0.31}As$ quantum wells (1.0% compressive strain) and seven $In_{0.52}Al_{0.36}Ga_{0.12}As$ unstrained barriers. The lasers are grown using digital alloy molecular beam epitaxy (MBE). The band diagram analysis shows a large conduction band offset which is typical of InAlGaAs lasers.

The geometry-dependent and temperature-dependent measurement as well as the laser optical gain, loss and spectral properties were carried out and comparison done for different ridge widths (1.2 to 2.8μm), cavity lengths (555 to 2200μm) and temperature range between 25 and 70°C. The output power as a function of current characteristics reveals threshold current increase with cavity lengths and ridge widths with thermal roll-off occurring at higher injection currents. The slope efficiency and external differential quantum efficiency increases for the narrowest and widest ridge widths within the same cavity length laser device but decreases with increase in cavity length.

The temperature analysis shows longer cavity length lasers exhibit better temperature characteristic than the shorter cavity length laser devices indicating the better thermal stability of the longer cavity lasers. Temperature elevations also caused increase in threshold current and decrease in efficiencies. The temperature distribution shows a higher temperature in the active region than the operating temperature due to self heating of the laser devices in continuous wave operation. The

optical spectrum exhibits red-shifting of the emission wavelength with increasing bias current and temperature.

Dedication:

Dr Trevor J. Hall

Acknowledgments

I am most grateful for the mentoring, support and understanding of my supervisors Dr. Trevor J. Hall and Dr Karin Hinzer. My sincere appreciation goes to my colleague Ron Millet for his assistance and guidance during the research. To Dr Henry Shreimer, Nic Olivieri and other members of the PTL research group.

This research was performed at the Photonics Technology Lab, School of Information Technology and Engineering (SITE), at the University of Ottawa, from September 2007 to August 2008. Financial support was provided by Natural Sciences and Engineering Research Council (NSERC), Ontario Centres of Excellence (OCE), Canada Research Chairs Program, Canadian Photonics Fabrication Research (CPFR), University of Ottawa through the Centre of Research for Photonics (CRPuO). We wish to thank Bookham Technology for the donation of the devices characterized in the thesis and Dr Anthony J. SpringThorpe for the crystal growth act.

I would like to thank Akwa Ibom State Government, Nigeria for presenting me with an opportunity that became the foundation. My heartfelt love goes to my family in Nigeria – Mama, Papa, Mayen, Koko, Maureen and Clement for their understanding and love, I miss you tremendously. My unwavering love and deep gratitude goes to my fiancé Akan Udoeyop for his love and encouragement. My appreciation goes to my roommates Amy and Collin for being so good and to my friends for their encouragement and support.

Table of Content

List of Figures

List of Tables

List of Abbreviations

1D	One-dimensional
2D	Two-dimensional
CW	Continuous wave
DUT	Device under test
FP	Fabry Perot
IR	Infra red
IV	Current-Voltage
L	Cavity Length
LAS2D	Laser-2-dimensional (Simulation software by Ecole Polytechnique)
LASER	Light Amplification by the Stimulated Emission of Radiation
L-I	Light-current
MBE	Molecular beam epitaxy
MOCVD	Metalorganic chemical vapour deposition
MQW	Multiple quantum well
OSA	Optical spectrum analyzer
PL	photoluminescence
QW	Quantum well
R	Ridge width or Reflectivity (when both facets have equal reflectivities)
RWG	Ridge waveguide
SCH	Separate confinement heterostructure
SRH	Shockley-Read-Hall
TE	Transverse electric
TEC	Thermo-electric Cooler
TM	Transverse magnetic

Chapter 1 Introduction

1.1 Overview

Semiconductor diode lasers are considered one of the most relevant innovations in the laser history. Due to their small sizes and higher energy efficiency their applications are quite novel especially in compact devices and systems. Diode lasers are categorized by their emission wavelength as well as the semiconductor materials from which they are made.

A quantum well device is formed by placing a narrow bandgap semiconductor material between two wider bandgap semiconductor materials, the two semiconductor materials are lattice matched to reduce the interface defects due to mismatch of crystal dimensions between the materials. It therefore implies that when layers of semiconductor materials of unequal band gaps are physically grown together, a semiconductor heterojunction is formed. Since the two or more semiconductor materials are different, there will be changes in the bandgap, E_g, at the interface resulting in discontinuities in conduction band (E_c) and valence band (E_v), this change will depend on the doping of the semiconductor materials[1].

Long wavelength multi quantum well (MQW) semiconductor laser diodes made in the AlGaInAs quaternary material system are of interest in optoelectronics applications because of their promising peak and differential gain performance, low transparency carrier density and good thermal properties[2]. In addition, AlGaInAs is an attractive material because its band gap can be tuned over communications wavelengths by

varying the composition, and can be easily grown on InP substrates[3]. The gain in the quantum well laser is embedded inside a large optical confinement region. Carriers in the quantum well are confined in one dimension and have discrete energy bands. The carrier and gain nonlinearities in quantum well are determined to a large extent by the properties of the confinement region[4].

The semiconductor lasers used in systems requires a robust temperature performance for application in ambient, uncooled environments where the device may be required to operate between 40°C and 85°C [5]. Therefore, to improve these laser devices, importance should be placed on studying their temperature dependent responses.

The continuous wavelength properties of multiple quantum well long wavelength lasers has focused heavily on the properties of the threshold current, specifically its reduction with changes in device structure and geometry and its temperature sensitivity. Increase in the above threshold efficiency is also advantageous in applications where CW operation with a minimum of current consumption is desired such a high power externally modulated sources for use as transmitters[6]. InAlGaAs material is employed for the realization of efficient lasers because of its promising peak, high differential gain and good thermal properties[2].

1.2 Aims and Objectives

The aim of this thesis is to use experimentation and simulation approaches to realize a working InAlGaAs/InP laser fit to be integrated into a system as an optical source. The device under study represent the long wavelength InAlGaAs laser devices, this permits us to understand

the operation of this material system in wavelengths further than the typical optical fiber communications range to find its uses in biological or environmental systems. The systematic measurement analysis of the laser properties and modeling of the material parameters through a series of simulations will meet system objectives while satisfying system constraints. Device simulation study is undertaken with focus on functionality to maintain a good performance laser. Detailed device characterization is conducted to understand the dependence of the performance of the InP-based InAlGaAs laser performance on the material, geometry and temperature parameters.

The objectives of the thesis are:

- To have a detailed working knowledge of the thesis topic
- To carry out a detailed experimental analysis of the already fabricated InAlGaAs/InP diode laser
- To carry out a systematic performance analysis of InAlGaAs/InP laser
- To describe the functional laser characteristics based on the results
- To identify and evaluate the applicability of the laser and come up with confirmatory reasons why this laser will be a useful alternative
- To publish a research paper based on the results

The outcome of the research work is comparable with existing relevant reports in literature. The results, conclusions and recommendations provide opportunities for further confirmatory research work and possibly future laser implementation and integration in active optoelectronics systems.

1.3 Brief Thesis Outline

This thesis is divided into seven chapters as follows:

The remaining sections of chapter 1 describe in detail the device structure, and the device fabrication technique using digital alloy molecular beam epitaxy (MBE) to grow the laser structures is also briefly discussed as well as the advantages of the InAlGaAs lasers.

Chapter 2 presents the theory of semiconductor diode lasers. The chapter explains various fundamental properties such as Fermi distribution and density of states, band gap, carrier recombination and generation mechanisms. The laser characteristics such as the light-current output, carrier consumption, threshold current and efficiencies are also explained. This chapter also discusses quantum well lasers as well as the $In_{1-x-y}Al_xGa_yAs/InP$ material system in terms of the energy dispersion and band gap engineering.

Chapter 3 delves briefly into the research work carried out on InAlGaAs semiconductor laser found in available relevant literatures.

Chapter 4 presents the experimental characterization of these lasers to include its light-current, optical, intrinsic dynamics as well as thermal characteristics. The measurement results present a critical assessment of InAlGaAs laser. This chapter also details the experimental procedures used.

Chapter 5 discusses the common considerations in laser material modelling to include some of the different aspects of material modelling as well as detailing the implementation of the InAlGaAs laser design in

the Las2D simulator. The analysis of the simulation shows its geometry and temperature dependency to include the optical modal gain and loss, carrier density, band structure, recombination rates etc.

Chapter 7 presents the overall conclusion based on the research. The chapter also discusses the future work with focus on the InAlGaAs design optimization to reduce its threshold current and improve the output power as well as the differential gain.

1.4 Device Structure

The InAlGaAs epitaxial structures were grown on a 3-inch sulphur-(n-)doped InP (100) substrate. The growth was performed in a V-80H MBE system equipped with soft action shutters and large capacity Veeco-EPI group V crackers[7,8]. The structure is grown by digital alloy molecular-beam-epitaxy (MBE). Fabry–Perot lasers are formed with cleaved facets and various cavity length and waveguiding ridge widths.

The laser MQW active region consists of six 5 nm thick $In_{0.69}Ga_{0.31}As$ quantum wells (1.0% compressive strain) separated by seven 10 nm thick unstrained $In_{0.52}Al_{0.36}Ga_{0.12}As$ barriers. The MQW region has a measured photoluminescence (PL) peak near 1.65 - 1.7 μm.

The undoped MQW region is sandwiched between four $In_{0.52}Al_{0.40}Ga_{0.08}As$ confinement layers with two layers each above and below the QW regions. The closest confinement layers to the upper and lower QW region are each undoped and 50 nm thick and the two farther ones are each doped p-type (Be: 5.0×10^{17} cm^{-3}) and n-type (Si: 5.0×10^{17} cm^{-3}) and each 100 nm thick. This completes the waveguide region.

The p-type (upper) and n-type (lower) cladding layers are each 150 nm p-$In_{0.52}Al_{0.48}As$ (Be: 5.0×10^{17} cm^{-3}) and n-$In_{0.52}Al_{0.48}As$ (Si: 5.0×10^{17} cm^{-3}). This waveguide region is grown on 150 nm thick n-$In_{0.52}Al_{0.40}Ga_{0.08}As$ (Si: $1.0\times10^{18}cm^{-3}$) infill layer and 50 nm n-InP (Si: 1.0×10^{18} cm^{-3}).

The waveguide region is covered by 25 nm p-InP. The last two p-InP layers of 200 nm and 1400 nm form the ridge waveguide. The upper part of the ridge is covered by a 200 nm heavily doped p- $In_{0.53}Ga_{0.47}As$ (Zn: 1.0×10^{19} cm^{-3}) top contact layer. The total device thickness including the substrate is ≈137 μm. The bandgap energy of the barrier layers as calculated in chapter 2 section 2.5.1 is ~1.268 eV (at 300K). The detailed layer structure is shown in Table 1-1.

Table 1-1 Epitaxial structure of the $In_{1-x-y}Al_xGa_yAs$/InP laser

Thickness	Material Composition	Doping type and level	Layer Comment
200nm	$In_{0.53}Ga_{0.47}As$	p = Zn (2e19/cm^3)	Contact layer
1400nm	InP	p = Zn (1e18/cm^3)	Ridge
200nm	InP	p = Zn (6e17/cm^3)	
5nm	1.3 Q etch stop	p = Zn (6e17/cm^3)	Etch stop
25nm	InP	p = Zn (4e17/cm^3)	Upper cladding
150nm	$In_{0.52}Al_{0.48}As$	p = Be (5e17/cm^3)	
150nm	$In_{0.52}Al_{0.48}As$	n = Si (5e17/cm^3)	Lower cladding
20nm	$In_{0.52}Al_{0.40}Ga_{0.08}As$ infill layer	n = Si (1e18/cm^3)	Buffer
50nm	InP	n = Si (1e18/cm^3)	
135 μm	S-doped InP 3" single sided	n = Si (1e18/cm^3)	Substrate

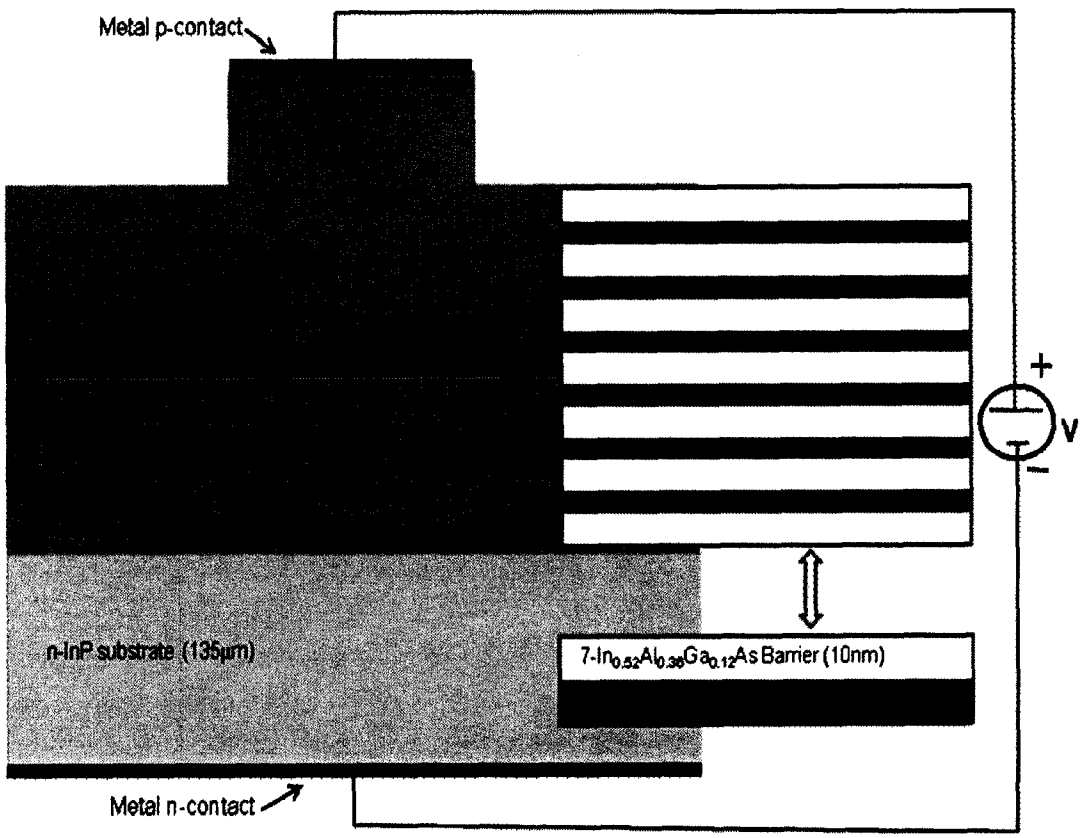

Fig. 1-1 Epitaxial structure of the $In_{1-x-y}Al_xGa_yAs/InP$ laser

Fig. 1-1 Epitaxial structure of the $In_{1-x-y}Al_xGa_yAs/InP$ laser illustrates the waveguide cross-section and Fig. 1-2 shows a top view picture of the laser physical structure through a microscope. Each bar has cleaved-cleaved facets and contains several devices depending on the bar length. The devices cavity lengths (equal to bar width) ranges between 555 and 2200 μm. The devices ridge widths are 1.2, 1.6, 2.0, 2.4, 2.8 and 50 μm. The 50 μm ridge width was excluded from the measurements.

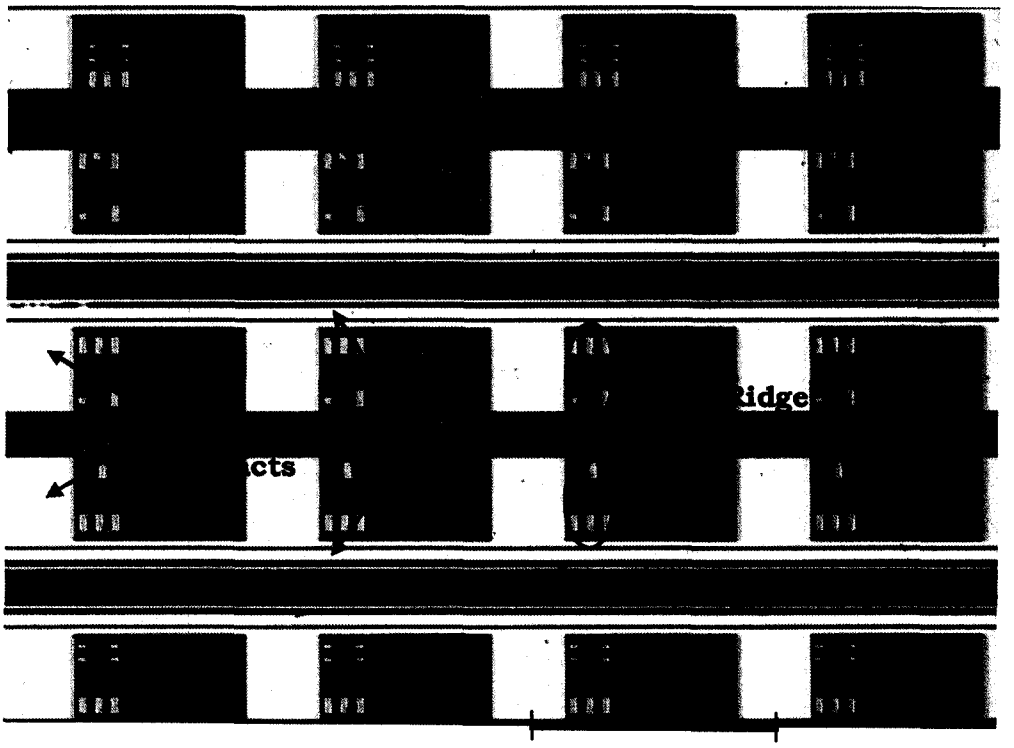

Fig. 1-2 Microscopic planar image of the laser devices on a bar.

The repetition of each set of ridge width on the same laser bar provides a good method to verify the measurement results since the same ridge widths would have similar properties. All devices have two cleaved facets.

1.5 Material Growth and Device Processing

Molecular beam epitaxy (MBE) and metal-organic chemical vapour deposition (MOCVD) are the two important techniques used in growing compressively strained laser. Both techniques have different growth methods. MBE is a physical deposition process carried out under ultra-high vacuum conditions in which beams of atoms are evaporated from diffusion cells and allowed to condense on a heated substrate. The substrate temperature has to be at a sufficient temperature in order for

condensation to occur, because Group III elements are less volatile, they tend to settle easily on the substrate unlike the volatile Group V elements which can easily evaporate unless there is a Group III element(s) to form compounds with[7] [8]. The ultrahigh vacuum condition and precise flux control allows MBE to grow high purity materials and uniform thin films. In MOCVD, the growth is carried out with a moderate gas pressure using toxic gases. The chemical reaction happens near equilibrium conditions. Because MOCVD can remove surface damage at the beginning of growth, it tends to provide defect-free high quality interface materials.

"Solid source MBE is at a disadvantage relative to the gas-based epitaxial techniques of chemical beam epitaxy (CBE) and MOCVD when it is necessary to grow complex structures in which there are a number of layers of different alloy compositions. This is due to the relatively small number of available group III sources on even the largest MBE systems. Although there is limited freedom in changing fluxes via source temperature changes, the time associated with these changes make it impractical for all but the simplest structures. However, this problem is readily circumvented using the digital alloy technique. By depositing sequential layers ranging in thickness from a fraction of to a few monolayers of binary and ternary alloys one can approximate the bulk alloys in their crystallographic and macroscopic electrical and optical properties. All lattice matched InAlGaAs alloys can be approximated using a digital alloy structure based on the lattice matched InAlAs and GaInAs ternaries. This is not possible for strained compositions, and some combinations of binary and ternary, and/or quaternary layers are needed to approximate the bulk alloy"[7].

For the laser devices, the 10 nm thick lattice matched InAlGaAs barrier layers, and 5 nm strained multiple-quantum-well active layers

were grown by digital alloy MBE, with the upper layer of the structure completed by MOCVD re-growth. InAlGaAs epitaxial structures were deposited on a 3-inch sulfur-doped InP substrates by solid source MBE. Substrate temperatures were measured using absorption band-edge spectroscopy, and controlled, for a given temperature, using constant power input to the substrate heater. The digital alloy MBE technique was used by depositing sequential layers of fractional thicknesses to a few monolayers of binary and ternary alloys. The binary and ternary layers were used to approximate the bulk alloy. The basic structure is a superlattice (SL) consisting of seven 10 nm barriers of lattice matched InAlGaAs and six 5 nm layers of ~1.0% compressively strained InGaAs.

1.6 Advantages of InAlGaAs Materials

A number of research papers have reported on the important properties InAlGaAs on InP laser each with a slightly different focus as explained in chapter 3 section 3.2. The InAlGaAs laser system seems to be advantageous over the much studied InGaAsP laser system.

InAlGaAs material system consists of only one group V element, and therefore does not suffer from the As/P control problem encountered in molecular beam epitaxy (MBE) of InGaAsP [9].

The advantages of InAlGaAs lasers originate from the conduction band and the band alignment to InP, larger conduction band offset of $\Delta E_c/\Delta E_g$ = 0.7, in comparison to $\Delta E_c/\Delta E_g$= 0.4 for InGaAsP material system, thus providing better electron confinement in the conduction band, that suppresses thermal-induced carrier leakage[10].

The spectral range covered by $In_{1-x-y}Al_yGa_xAs$ quaternary system when lattice matched to InP is 1630-850nm which is slightly larger than $In_{1-x}Ga_xAs_yP_{1-y}$ system at 1630-920nm[11].

InAlGaAs laser diodes have low temperature sensitivity of the threshold current (higher T_0) compared to InGaAsP lasers thus reducing the temperature sensitivity of devices[12]. Higher differential gain and lower threshold current density has been reported in theoretical studies for strained InGaAs/InAlGaAs QW lasers, than those obtained for InGaAs/InGaAsP lasers[13].

1.7 Summary

This chapter introduced the laser material composition and structure in details as well as the device fabrication technique using digital alloy molecular beam epitaxy (MBE) and MOCVD. The advantages of the InAlGaAs was also discussed.

Chapter 2 Theory of Semiconductor Diode Lasers

2.1 Introduction

This chapter reviews the important aspects of semiconductor diode lasers such as the Fermi distribution and density of states, band gap energy, and carrier recombination and generation mechanisms. Laser characteristics such as light-current, threshold, slope and external efficiencies, optical gain and loss, temperature characteristics are discussed. The quantum well structures and the effect of strain in them are also briefly described. The $In_{1-x-y}Al_xGa_yAs/InP$ material system is also covered with emphasis on the energy dispersion and band gap engineering. The device fabrication technique using digital alloy molecular beam epitaxy (MBE) and metal-organic chemical vapour deposition (MOCVD) to grow the laser structures is also briefly discussed which in this case preludes this thesis work (previously developed at Nortel Networks and bought over by Bookham Technology).

2.2 Properties of III-V Semiconductors

2.2.1 Electrons, Holes, Fermi Distribution and Density of States

The conduction of electrical current is a result of the flow of electrons. Some electrons are free to jump from the valence band to conduction band separated by an energy gap E_g, a valence electron needs at least the bandgap energy in order to successfully move to the conduction band

leaving behind holes. Both electrons and holes can carry electrical current and thus are called carriers.

Based on electrical conductivity, there are three forms of solid-state materials; metals, semiconductors and insulators. Metals are good conductors because they produce a large amount of free electrons with an applied electrical field and as such there is no band gap energy required. Insulators are poor conductors and because of the large energy bandgap between the conduction band and the valence band, a large amount of electrical current is required to overcome the bandgap which in most cases destroy the material. Semiconductors as the name implies has electrical properties between a conductor and an insulator, the conductivity of semiconductors varies with the temperature and material properties. The energy bandgap, E_g, is in the order of 1 eV, thereby electrons can easily be excited to the conduction band.

The carrier concentration depends on the density of electron states, $D(E)$, and the probability that an electron occupies a certain state. The probability of finding an electron at an energy, E, is given by the Fermi distribution function[14]:

$$f(E) = \frac{1}{1 + \exp\left[\frac{E - E_F}{k_B T}\right]} \qquad 2\text{-}1$$

where E_F is the Fermi energy, k_B is the Boltzmann constant and T is the temperature in Kelvin. At T = 0K, the Fermi energy separates occupied from the unoccupied energy levels, as T increases more electrons move from the valence band to the conduction band. In intrinsic (pure) semiconductors, E_F is in the middle of the band gap thereby balancing the electron and hole concentrations. It is the opposite in extrinsic

(doped) semiconductors and E_F will be either close to the valence band (p-type) or to the conduction band (n-type).

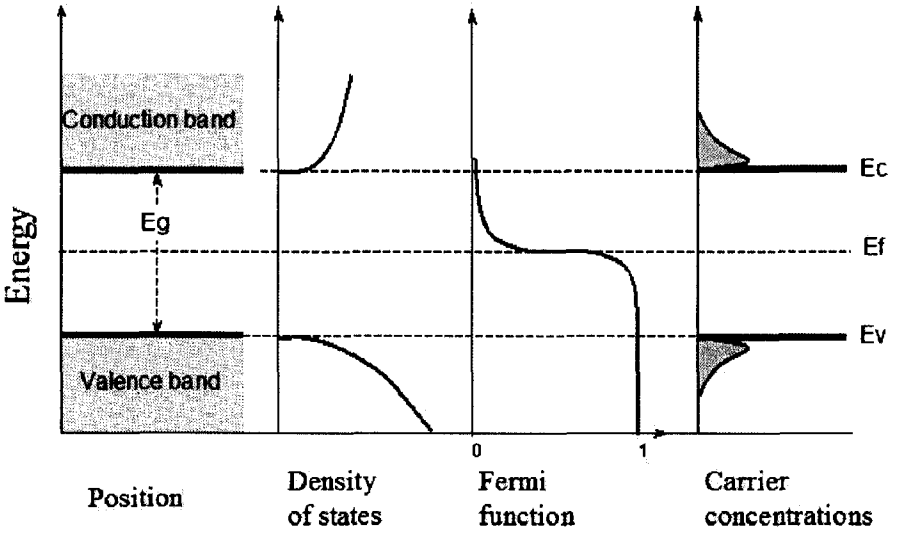

Fig. 2-1 The energy bands, density of states, Fermi distribution function and the carrier concentrations as a function of energy[15].

The density of electron state is determined by the energy dispersion function, $E(k)$ as illustrated in Fig. 2-1 in which case the electrons and holes are considered to be (quasi-) free particles. The density of states in both bands thereby becomes a parabolic function of the energy E :

$$D_c(E) = \frac{1}{2\pi^2}\left(\frac{2m_c}{\eta^2}\right)^{3/2}\sqrt{E - E_c} \qquad (E > E_c) \qquad 2\text{-}2$$

and

$$D_v(E) = \frac{1}{2\pi^2}\left(\frac{2m_v}{\eta^2}\right)^{3/2}\sqrt{E - E_v} \qquad (E < E_c) \qquad 2\text{-}3$$

for the conduction band and the valence band respectively, where m_c and m_v are the effective masses of electrons and holes. E_c and E_v are the energy of conduction and valence band edges. The carrier density as a function of energy is given by:

$$n(E) = D_c(E)f(E)$$
$$p(E) = D_v(E)[1 - f(E)] \qquad 2\text{-}4$$

Integrating $D_c(E)f(E)$ over the energy from the band edges results in the total carrier concentrations:

$$n \approx N_c \exp\left(\frac{E_F - E_c}{k_B T}\right)$$
$$p \approx N_v \exp\left(\frac{E_F - E_v}{k_B T}\right) \qquad 2\text{-}5$$

where $N_c = 2\left(\frac{m_c k_B T}{2\pi\eta^2}\right)^{3/2}$ and $N_v = 2\left(\frac{m_v k_B T}{2\pi\eta^2}\right)^{3/2}$ are the effective density of states for the conduction and the valence band, respectively. n and p are valid for only low carrier concentrations $(n << N_c, p << N_v)$.

The energy dispersion relation of semiconductors strongly depends on the crystal lattice structure because in semiconductors the atoms in the crystal lattice have built up a periodic lattice potential. $E(k)$ therefore deviates from the parabolicity at large electron momentum values. To calculate energy dispersion for specific compounds, the multi-band $K \cdot P$ method is used. Fig. 2-2 illustrates the InP band structure in the first Brillouin zone (where the wavevector, k is between $-\pi/a_0 < k_x < \pi/a_0$, and

a_0 is the lattice constant) showing the different conduction band valleys, *X*, Γ, and *L*. The direct band gap, E_g of the Γ-valley exists at the center of the first Brillouin zone Γ where the important minima of the conduction band and maxima of the valence band is present. In light-matter interaction, the band gap determines the wavelength of the light.

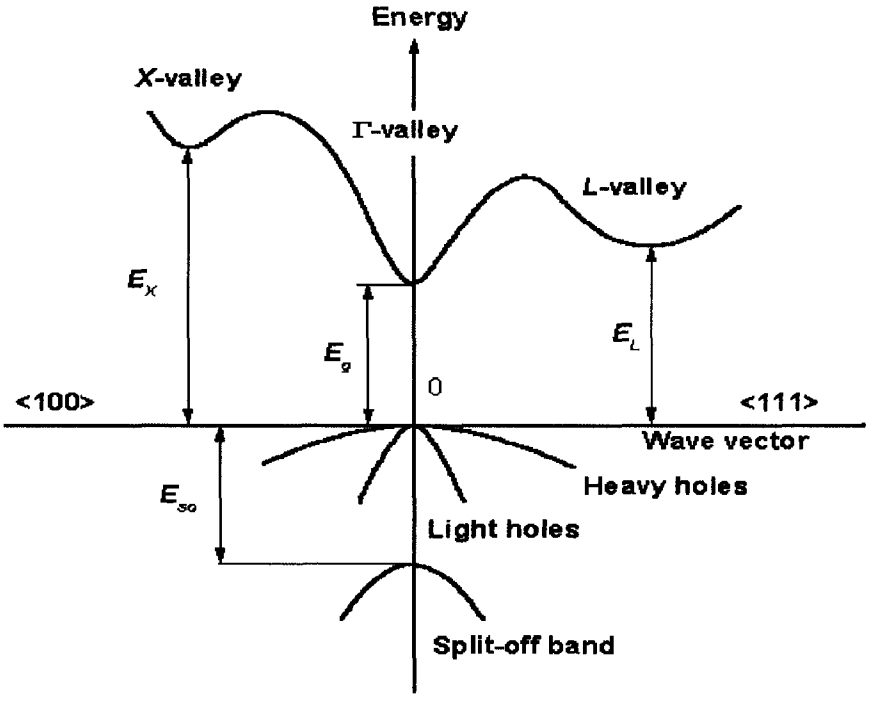

Fig. 2-2 Band Structure of InP at 300K (E_g = 1.34eV, E_L =1.93eV, E_{so} = 0.11eV)

2.2.2 Band Gap of III-V Semiconductors and Alloys

III-V semiconductors are important for optoelectronics applications because they are mostly direct bandgap materials as such carriers can transfer between the conduction and valence bands with no change in momentum emitting light in the process. III-V semiconductors can also form alloys with more than one element, these alloy compositions can be changed in order to adjust the bandgap parameters to meet specific

requirements. They are compounds from a mixture of both Group III and Group V elements and their crystal is of the zinc-blende type exhibiting a so-called face-centered cubic (fcc) lattice. To produce quality device materials, the lattice constant confines ternary and quaternary alloys to certain binary compounds (substrates). A comprehensive compilation of band parameters for most III-V compounds can be found in reference[16].

2.2.3 Carrier Recombination and Generation Mechanisms

Carriers in semiconductor lasers are created by forward biasing the p-n junction thus creating excitation for the onset of lasing. The photons generated do so by the recombination (destruction of an electron-hole pair due to electron jump from the conduction to valence band) of both the majority and minority carriers. The injected carriers recombine in different forms, the radiative recombination which uses band-to-band transition between energy levels to release energy corresponding to the bandgap of the semiconductor, and the non-radiative recombinations Shockley-Read-Hall via centers in the forbidden gap or Auger recombinations in which the energy is released as a phonon. The emission efficiency of the laser and subsequent threshold condition therefore relies heavily on these recombinations

In laser operation the stimulated emission is very necessary and the spontaneous emission occurs naturally thereby dominating the carrier recombination paths. Fig. 2-3 shows the photon absorption and generation through band-to-band radiative transitions.

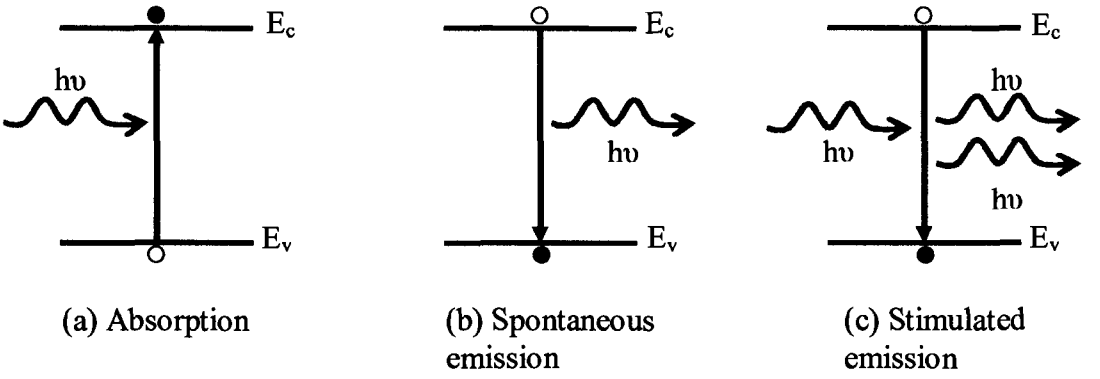

(a) Absorption

(b) Spontaneous emission

(c) Stimulated emission

Fig. 2-3 Photon absorption and generation through band-to-band recombination

The different recombination mechanisms are illustrated in Fig. 2-4 below

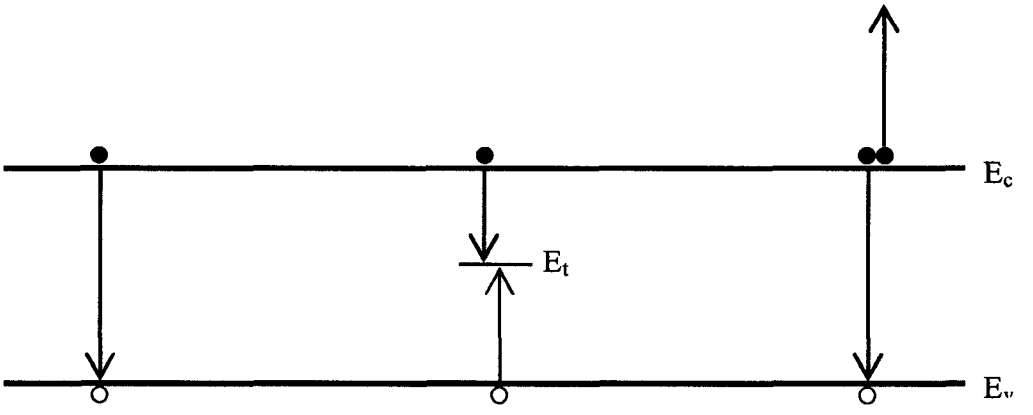

(a) band-to-band recombination

(b) Shockley-Read-Hall (trap-assisted) recombination

(c) Auger recombination

Fig. 2-4 Carrier recombination mechanisms

Note: For illustrative purposes the energy bands are assumed to be flat and single level but realistically each is made up of different energy levels and they are rather curved.

Band-to-Band (Spontaneous)	**SRH (trap-assisted)**	**Auger**
$R_{spon} = B(np + n_0 p_0)$	$R_{SRH} = \frac{np - n_0 p_0}{\tau_p (n + n_1) + \tau_n (p + p_1)}$	$R_{Aug} = (C_n n + C_p p)(np - n_0 p_0)$

where

n_0, p_0 = carrier densities at thermal equilibrium

n_1, p_1 = intrinsic carrier density

τ_n = non-radiative electron lifetime

τ_p = non-radiative hole lifetime

B = radiative recombination constant

C_n and C_p = Auger recombination constants

The density of states in the conduction and valence bands, which is material dependent, and the carriers in the available energy states affects the rate of the radiative processes. The net photon generation rate is therefore:

$$R_{st} = R_{21} - R_{12} = R_r (f_2 - f_1) \qquad 2\text{-}6$$

where R_{st}, R_{21} and R_{12} are the recombination rates for stimulated emission, spontaneous emission and absorption respectively.

$$f_1 = \frac{1}{e^{(E_1 - E_{Fv})/kT} + 1}, \quad f_2 = \frac{1}{e^{(E_2 - E_{Fc})/kT} + 1}, \qquad 2\text{-}7$$

where E_{Fc}, E_{Fv} are the conduction and valence band quasi-Fermi levels.

When voltage is applied across the junction in forward bias, a value slightly lower than the applied voltage separates the quasi-Fermi levels. If this value increases such that it is greater than the photon energy it will subsequently increase the stimulated emission rate and the optical gain. To achieve positive material gain we must therefore equalize the photon energy and the band gap energy

$$\Delta E_F = E_{Fc} - E_{Fv} > E_{21} = h\nu > E_g \qquad 2\text{-}8$$

thereby resulting in the very important population inversion relation which must be satisfied.

2.3 Laser Characteristics

2.3.1 Light-Current

The light-current (L-I curve) is a very important tool in laser characterization. It is a plot of the light power emitted as a function of the injection current for a specific laser device at a specific temperature. The L-I measurements are obtained by varying the injection current and simultaneously measuring the light output power using a photodetector. Several laser parameters can be derived from the L-I graph such as the maximum power, threshold current and the slope efficiency of the laser device.

At very low current, the spontaneous emission dominates and the output power stays at very low levels. When the current passes threshold, the stimulated emission dominates and there is abrupt increase in the light output power.

2.3.2 Carrier Consumption at Threshold

Threshold current density in diode lasers is controlled by the amount of currents by Shockley-Read-Hall (SRH) recombination, spontaneous emission, Auger recombination, vertical leakage, and lateral leakage:

$$I_{th} = I_{SRH} + I_{spon} + I_{Auger} + I_{vleak} + I_{lleak} \qquad 2\text{-}9$$

Usually, lateral leakage and spontaneous emission consume most of the injection carriers below threshold. SRH and Auger recombination are weak due to the high purity material and the relatively wide band gap hetero-junctions.

Ridge waveguide (RWG) lasers performance is highly dependent on current flow to the active region[17,18]. Lateral current spreading in this region can significantly affect the device performance and can result in a reduced efficiency above threshold[19], a degradation of operation in the fundamental transverse mode operation, a perturbation of the longitudinal mode through the lateral mode instability[20], and a rise in intermodulation distortion under direct modulation[21 22].

The lateral leakage current is mainly caused by diffusion and drift of holes through the p-doped cladding layer under the ridge. Hence one can write the following statement:

$$I_{th} = J_{th} L_c W + I_{lleak} = J_{th} L_c \cdot W + J_{lleak} t \cdot L_c \qquad 2\text{-}10$$

where J_{lleak} is the lateral leakage current density, J_{th} is the threshold current density, L_c is the cavity length, W is the ridge width and t is the thickness that the lateral leakage current passes through. I_{lleak} is obtained from the intercepts of the linear fits. Applying a linear fit of I_{lleak} to cavity length L_c, the lateral leakage current density can be estimated.

Current density in a p-type semiconductor can be described by the one-dimensional charge continuity equation:

$$\frac{\partial p}{\partial t} = -p\mu_p \frac{\partial \varepsilon}{\partial y} - \mu_p \varepsilon \frac{\partial p}{\partial y} + D_p \frac{\partial^2 p}{\partial y^2} + G - R + \frac{j_p}{qd} \qquad 2\text{-}11$$

Where j_p is the injection current of a volume with thickness d. μ_p and D_p are the hole effective mobility and effective diffusion coefficient.

Laterally, carrier generation and recombination are not likely to occur underneath the ridge, and the injection current density, j_p, is small. Therefore the last three terms in equation 2-11 can be neglected. Effective hole mobility is the dominant parameter in equation 2-11 and it strongly affects the lateral leakage current. Such parameter like the spontaneous emission rate through the hole spatial distribution does not play a dominant role. Therefore it can be concluded that the effective hole mobility largely determines the intercepts of the linear fit – this is the lateral leakage current at threshold as the laser ridge width goes to zero.

Vertically, equation 2-11 describes the hole dynamics. All effects from the carrier generation and recombination sum up to gain or loss until the carrier density reach the threshold value.

An analysis using carrier transport and continuity theories proves that the lateral leakage current is a function of laser ridge width[23]. Therefore the threshold current seems to extend away from the linear trend when the ridge width gets narrower than 4 μm[15]. Depending on the band structure, material, and operating temperature an injected carrier can dissipate in the form of a radiative or non-radiative recombination. Therefore the carrier consumption for each recombination mechanism can be determined as a function of current as well as the carrier leakage as a function of current.

2.3.3 Threshold Current

For lasing to occur, the injection current must reach a certain minimum value called the threshold current. At this current there are enough carriers to compensate for all the losses in the laser cavity, such as the leakage current and recombination processes.

The lasing process is a steady-state phenomenon and therefore gain should clamp at the threshold gain even as current is increased[24]. This is illustrated by the linear behaviour that the graph exhibits after threshold. The value of the threshold current in the simplest form is the intercept of the x-axis (current axis), considering only the linear part of the graph. A more accurate method of determining the threshold current is through the second derivative of the LI curve. The maximum value of the second derivative of the LI curve is used to calculate the threshold current.

A wider and longer laser requires more injection current to start lasing. Therefore when comparing the threshold current values of different laser devices, it is more accurate to consider threshold current density rather than threshold current. Threshold current density is denoted by the symbol J_{th}, it is determined by dividing the experimentally obtained threshold current value, I_{th} by the area of the laser. In a RWG laser, the area of the laser device is the multiplication of the cavity length and the ridge width values.

The threshold current can be approximated as the sum of two parts as explained in equation 2-10, where I_{leak} is the lateral leakage current, L_c is the laser cavity length, W is the ridge width of the RWG laser and J_{th} is the threshold current density. It implies that the intercept of the linear regression when the threshold current is plotted as a function of the ridge width gives the lateral leakage current. The slope of the linear regression can also give the threshold current density at the specified cavity length.

Threshold current is therefore an important characteristic since it is the minimum current value at which a laser turns on. Low threshold currents are usually desirable because if a threshold current is low it minimizes the input power needed to operate a laser, low current implies low internal temperatures which means less expensive thermoelectric coolers needed in packaging the laser devices thereby lowering the cost, a high threshold current on the other hand can heat up the laser device which will degrade the device performance.

However, threshold current depends on the quality of the semiconductor material from which the device is fabricated and the

geometry of the laser device. Thus, when comparing the threshold current values of different devices, it is more appropriate to refer to threshold current density (J_{th}). Threshold current density is a direct indication of the quality of the semiconductor material from which the laser device is fabricated.

2.3.4 Threshold Condition

Lasing threshold occurs when the gain in the active region overcomes the propagation and mirror losses. The electric field exactly replicates itself after one round-trip in the cavity. Increase in the gain occurs as a result of increase in the injection current density and subsequent increase in the carrier concentration. A threshold condition is thereby reached when the carrier concentration is at a threshold value.

The equivalent mathematical expression is

$$\left(g_{th}\Gamma = \alpha_i + \alpha_m\right) \qquad 2\text{-}12$$

$$\alpha_i = \alpha_0\left(1-\Gamma\right)+\alpha_g\Gamma \qquad 2\text{-}13$$

$$\alpha_m = \frac{1}{2L}\ln\frac{1}{R_1R_2} \qquad 2\text{-}14$$

$$R_1R_2\exp\{(\Gamma g_{th}-\alpha_i)L\} = 1 \qquad 2\text{-}15$$

where Γ is the mode confinement factor, g_{th} is the threshold gain, α_i is the intrinsic propagation loss, α_m is the transmission losses at the two end facets, L is the cavity length and R_1 , R_2 are the mirror reflectivities.

Solving for the threshold gain, we obtain:

$$\Gamma g_{th} = \alpha_i + \frac{1}{L}\ln\left(\frac{1}{R_1 R_2}\right) \qquad 2\text{-}16$$

Below threshold, the output light consist of mainly spontaneous emission, increasing the injection current density J above threshold results in light emission through stimulated emission process. When the laser is operating above the threshold, due to gain saturation, the steady-state gain in the laser cavity equals its threshold value, $g = g_{th}$.

The threshold current density can be derived from the equation 2-16

$$\ln(J_{th}) = \ln(J_{tr}/\eta_i) + \left(\frac{\alpha_i + \alpha_m}{\Gamma g_0}\right) \qquad 2\text{-}17$$

where η_i is the internal quantum efficiency and α_m and is the mirror loss.

2.3.5 Output Power

All laser devices have maximum power at certain current level in which they can operate before saturation, and most times the power output then starts to decrease even if the injection current keeps increasing. The maximum power can also be affected by temperature elevation of the device.

2.3.6 Slope Efficiency

As it is desirable to have a low threshold current, it is also important to have rapid increase in output light emission for a small change in the input current above the threshold current. This measurement of the change in the output power versus injected current ($\Delta P/\Delta I$) above the threshold current is termed the slope efficiency; it is the slope of the linear portion of the L-I characteristic in units of mW/mA. This parameter indicates the device efficiency and show how much more output power can be expected out of a laser device given a certain amount of increase in current above threshold. The slope efficiency is dependent on the cavity length; usually longer cavity length lasers have lower slope efficiency.

2.3.7 External and Internal Quantum Efficiency

The external quantum efficiency (η_d) (converted to a percentage) indicates the efficiency of laser device in converting the injected electron hole pairs into photons emitted from the device. Theoretically, the recombination of each electron-hole pair results in the generation of one photon and the photon survives its travel through the laser waveguide structure to be emitted from the device. In reality, not all electron-hole pair recombination results in the generation of photons, some result in the generation of other undesirable forms of energy, such as heat[25]. Also, not all photons are emitted from the device, as some of them are reabsorbed by the structure.

The value of the external quantum efficiency is calculated from the slope efficiency value using 2-18 equation. For cleaved-cleaved facets, the reflectivities of both facets are assumed to be identical and a factor of two is incorporated. The external quantum efficiency is equal to

$$\eta_d = 2\frac{\Delta P}{\Delta I}\cdot\frac{\lambda q}{hc} \qquad 2\text{-}18$$

where;

λ is the wavelength of the laser,

h is Planck's constant = 6.62606896 x 10^{-34} Js,

q is the fundamental electronic charge = 1.602176487 x 10^{-19} C,

and c is the speed of light = 3 x 10^{8} m/s.

The amount of current that generates carriers in the active region determines the internal quantum efficiency. This is because of leakage of the injected current. Like η_d, the internal quantum efficiency (η_i) is a measure of the efficiency of a laser in converting electron-hole pairs (injected current) into photons within the laser structure. However, unlike the external quantum efficiency, the internal quantum efficiency is independent of the geometry of the laser device such as the cavity length or the ridge width. This parameter is used for the comparison of material properties of the laser devices.

The optical loss is a coefficient that relates the number of existing photons to the number of photons that will remain inside the cavity after having propagated a certain distance[24]. The losses could be caused by lateral spreading of carriers, carrier escape from the active region, and by recombination losses within the active layers. All these loss mechanisms contribute to the internal efficiency.

The internal and external quantum efficiency and optical loss can be extracted by doing measurements on identical devices of different cavity lengths and fitting the measurement data into the following equation:

$$\frac{1}{\eta_d} = \frac{1}{\eta_i}\left[1 + \frac{\alpha_i}{\ln(1/R)}L\right] \qquad 2\text{-}19$$

where

α_i is the net internal optical loss,

η_d is the external quantum efficiency,

η_i is the internal quantum efficiency,

R is the reflectivity,

and L is the cavity length.

A straight line can be obtained by plotting the reciprocal of the measured device efficiency (η_d) versus cavity length (L). The y-intercept of the straight line gives the inverse of the internal quantum efficiency and then used in the above equation to obtain the net optical loss. The value of η_d is less than the value of η_i. And the ratio of η_d/η_i gives the ratio of the number of photons emitted from the laser to the number of photons generated within the laser.

2.3.8 Characteristic Temperature

The ability of the laser to perform well at elevated temperatures is of great interest because heat generated in the test environment can cause the laser device temperature to rise significantly thus degrading the device if it does not have a good characteristic temperature. In order to understand the stability of laser performance when subjected to temperature it is necessary to determine the characteristic temperature of the laser.

The characteristic temperature (T_0) is a measure of the temperature sensitivity of the laser device[1]. It is a parameter that relates laser

operating temperature (laser local temperature) to its threshold current defined by the Arrhenius relationship of diode laser:

$$I_{th} = I_0 e^{T/T_0} \quad \text{or} \quad J_{th} = J_0 e^{T/T_0} \qquad 2\text{-}20$$

where T_0 can be obtained by the linear regression of the nature log of the threshold current over the temperature. T_0 is largely determined by the dominant recombination mechanism, which varies greatly with temperature. The temperature range of the measurement must be specified for a meaningful T_0 value.

$$\frac{\Delta \ln(I_{th})}{\Delta T} = \frac{1}{T_0} \quad \text{or} \quad \frac{\Delta \ln(J_{th})}{\Delta T} = \frac{1}{T_0} \qquad 2\text{-}21$$

where

I_{th} is the threshold current,

J_{th} is the threshold current density,

T is its operating temperature in Kelvin (K),

T_0 is its characteristic temperature in K,

Equation 2-20 shows that the threshold current is highly dependent on both its operating and characteristic temperatures. It is therefore preferable for a laser to have a high characteristic temperature so that its threshold current does not increase much even with a large increase in its operating temperature. This exponential relationship is related to the temperature effect on gain and loss within a laser. Temperature sensitivity of the threshold current is dominated by Auger recombination at lower temperatures and by vertical leakage at higher temperatures.

Carrier losses increase at higher temperatures due to higher carrier density which is mainly as a result of gain reduction[14].

Higher values of T_0 imply that the threshold current density and the differential quantum efficiency of the device increase less rapidly with increasing temperatures. This translates into the laser being more thermally stable.

The wavelength of a laser diode is directly proportional to its operating temperature. There is a linear relationship in which the temperature increases with wavelength. This is a red-shift characteristic which is useful in spectroscopic applications, where the wavelength of emission of the laser diode can be accurately temperature tuned to the specific properties of the material with which the laser diode is interacting[26].

2.3.9 Optical Gain and Loss

As the photon density propagates along the laser cavity, the material gain grows proportionally and the maximum gain is determined by the density of states of the material. Optical gain can be determined by considering the multiple reflections of a photon in a laser cavity at a sub-threshold current. Assuming that only the fundamental mode is excited in a laser cavity, the electric field at facet one is F_1, where F_1 is the fundamental mode field. When the reflected $\sqrt{R_1}F_1$ field propagates back along the cavity, it gets reflected at the second facet and when it returns back to the first facet, the electrical field will change to $\sqrt{R_1R_2}F_1\exp(-2\alpha(\lambda)L)$, where $\alpha(\lambda)$ is the mode propagation gain or loss in the cavity. Considering multiple reflections occurring at the two facets, the total field of the constructive wave at the first facet is[15 27]:

$$F_1^+ = F_1 \sum_{n=0}^{\infty} \left(\sqrt{R_1 R_2}\right)^n \exp(-n\alpha L) = \frac{F_1}{1-\sqrt{R_1 R_2}\exp(-\alpha L)} \qquad 2\text{-}22$$

the total field of the destructive wave at the same facet is:

$$F_1^- = \frac{F_1}{1+\sqrt{R_1 R_2}\exp(-\alpha L)}$$

The constructive and destructive waves can be measured outside the laser cavity by intensity variation. The ratio of the maximum and minimum intensity is:

$$r(\lambda) = \frac{P^+}{P^-} = \left(\frac{1+\sqrt{R_1 R_2}\exp(-\alpha(\lambda)L)}{1-\sqrt{R_1 R_2}\exp(-\alpha(\lambda)L)}\right)^2 \qquad 2\text{-}23$$

Therefore, the modal gain or loss can be calculated as:

$$\alpha(\lambda) = \frac{1}{L}\ln\left(\frac{\sqrt{r(\lambda)}+1}{\sqrt{r(\lambda)}-1}\right) + \frac{1}{2L}\ln R_1 R_2 \qquad 2\text{-}24$$

and the material gain $G(\lambda)$ is related to $\alpha(\lambda)$ and the confinement factor Γ by:

$$\Gamma G(\lambda) = \alpha(\lambda) \qquad 2\text{-}25$$

The laser internal loss can be measured based on the principles of Fabry-Perot cavity resonance. In a F-P resonant cavity, the steady-state output intensity at the end of a laser can be approximated as [28]:

$$I^{\pm}(\nu)=\frac{B(1+R_{\mu}G_s)(1-R_{\pm})}{(1+RG_s)^2-4RG_s\sin^2(\theta)} \qquad 2\text{-}26$$

where $R\pm$ are the reflectivities of the mirrors, G_s is the single-pass intensity gain, and B is the total amount of spontaneous light at frequency ν coupled into the laser mode.

For a symmetrical laser cavity, $\theta=2\pi L\nu/c$, where $c/2L$ is the free spectral range of the resonator. At $\theta=0$ and $\theta=\pi/2$, the intensity of the output reaches its minimum and maximum, respectively. The intensity ratio between the adjacent peak, I_p, and valley, I_v, can be calculated as:

$$r=\frac{I_p}{I_v}=\left(\frac{1-G_sR}{1+G_sR}\right)^2 \qquad 2\text{-}27$$

At transparency, a single pass gain relates to the internal loss by

$$G_s=e^{-\alpha_i L} \qquad 2\text{-}28$$

where L is the cavity length. The internal loss, α_i, can be found using equation 2-27 and 2-28 once the intensity ratio r is determined.

The facet reflectivity can be calculated using the effective index of reflection, n_{eff}, and the Fresnel's reflectivity formula

$$R = \left(\frac{n_{eff} - 1}{n_{eff} + 1} \right)^2 \qquad 2\text{-}29$$

n_{eff} is estimated by:

$$\Delta\lambda = \frac{\lambda^2}{2Ln_{eff}} \qquad 2\text{-}30$$

where λ is the lasing wavelength and $\Delta\lambda$ is the mode spacing in the F-P cavity.

2.4 Quantum Well Structures

2.4.1 Single and Multi-Quantum Well Structure

A quantum well device is formed by placing a narrow bandgap semiconductor material between two wider bandgap semiconductor materials, the two semiconductor materials are lattice matched to reduce the interface defects due to mismatch of crystal dimensions between the materials. It therefore implies that when layers of semiconductor materials of unequal band gaps are physically grown together, a semiconductor heterojunction is formed. Since the two or more semiconductor materials are different, there will be changes in the bandgap, E_g at the interface resulting in discontinuities in conduction band (E_c) and valence band (E_v). And this change will depend on the doping of the semiconductor materials[1].

The schematic diagram of a quantum well is shown below in the Fig. 2-5. Note that the wavelength emitted from the quantum well of a

semiconductor device is not the same with the respective bandgap energies of the individual semiconductor materials.

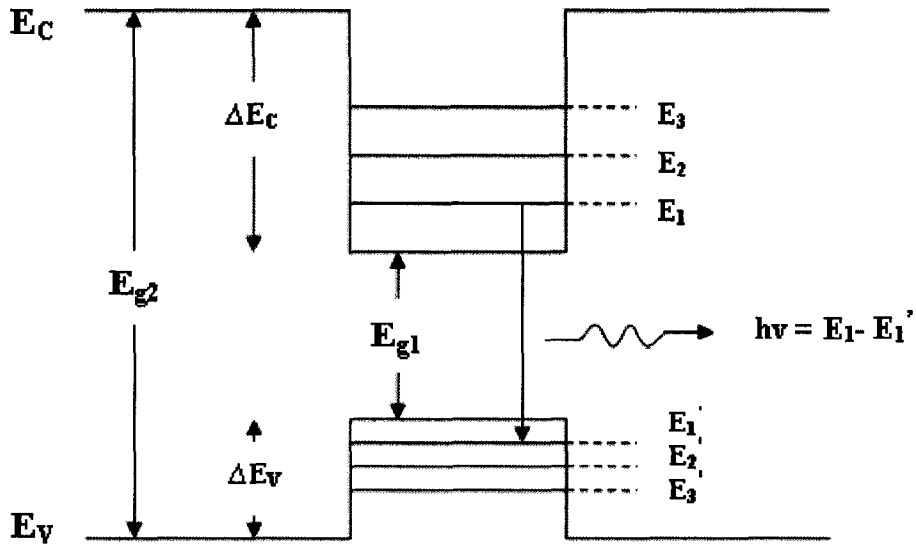

Fig. 2-5 Schematic of a single quantum well (SQW)

There is an effective carrier confinement in the quantum wells as well as lower threshold currents due to the density of electron states. The discrete transition energy levels present in quantum wells allow tuning of the desired wavelength of emission. The gain region in a quantum well in contrast with a bulk laser is a thin region and is embedded inside a larger optical confinement region[2].

The carriers in the quantum wells are confined in one dimension and have discrete energy bands; therefore to model the complete carrier injection, there needs to be examinations of the nature of its confinement, QW regions and the coupling. The carrier and gain nonlinearities in QW lasers are determined largely by the properties of the confinement region[29,30,31]. Thus in order to design a good QW structure, a thorough understanding of the carrier confinement in quantum well is necessary.

A multi quantum well (MQW) laser moves a step further in the advantage of providing higher output powers as well as providing better internal and differential quantum efficiencies for all cavity lengths. However single quantum well (SQW) lasers still exhibit higher threshold current than MQW lasers, but the small width of the gain region in a SQW lasers can cause poor optical confinement. A solution is using a MQW gain region and introducing a separate confinement heterostructure (SCH) – in some cases graded refractive index (GRIN)-SCH is used to enhance the optical confinement factor as well as lower threshold current.

The lower threshold current achieved in a QW laser as opposed to a bulk semiconductor laser is that with a QW laser the electrons are spread over a smaller energy range with a higher density at the band edge thereby giving rise to population inversion at low injected carrier density as compared to a conventional bulk laser diode in which the carriers are distributed over a wide range in the band and with relatively smaller density at the band edges[2]. In general, lasers with low threshold current are quite useful when a need to minimize power consumption is desired.

2.4.2 Strain in Quantum Wells

Strain effectively changes the band structure of the heterostructure thereby affecting the optical properties of the laser. This occurs when there is lattice mismatch at the interface of the heterojunction. The strain created does not cause serious defects if it is kept below a minimum value rather they are manipulated for better laser designs.

There are two types of strain that can be applied; compressive and tensile.

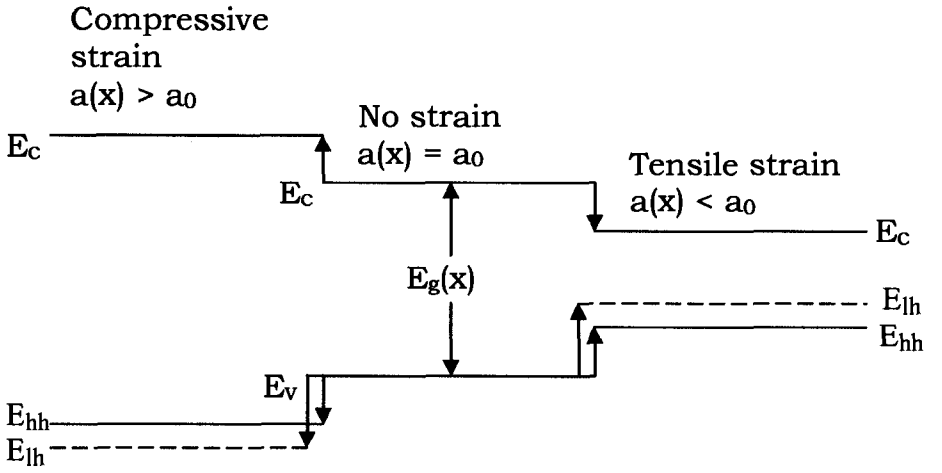

Fig. 2-6 Conduction and valence band edges for semiconductors under compressive strain, no strain and tensile strain.

a(x) is the lattice constant of the unstrained alloy, x is the mole fraction and a_0 is the lattice constant of the substrate and $E_g(x)$ is the bandgap of the unstrained alloy. At x = 0.468, a(0.468) = a_0 and the strain is zero, if x < 0.468, the lattice constant increases i.e., a(x) > a_0 resulting in compressive strain, when x > 0.468, the lattice constant decreases i.e., a(x) < a_0 resulting in tensile strain[32].

The magnitude of strain ε_{ij} is proportional to the relative change of lattice period $\varepsilon_{ij} = \Delta a_i / a_j$. The amount of energy shifts in the conduction and valence band edges are related to hydrostatic deformation potentials a_c, a_v and the shear deformation potential b as:

$$E_{hh}(0) = E_v^0 + a_v(\varepsilon_{xx} + \varepsilon_{yy} + \varepsilon_{zz}) + \frac{b}{2}(\varepsilon_{xx} + \varepsilon_{yy} - 2\varepsilon_{zz})$$

2-31

$$E_{lh}(0) = E_v^0 + a_v(\varepsilon_{xx} + \varepsilon_{yy} + \varepsilon_{zz}) - \frac{b}{2}(\varepsilon_{xx} + \varepsilon_{yy} - 2\varepsilon_{zz})$$

in valence bands, and

$$E_c(0) = E_c^0 = E_v^0 + E_g + a_c(\varepsilon_{xx} + \varepsilon_{yy} + \varepsilon_{zz}) \qquad 2\text{-}32$$

in the conduction band

In the conduction band the strain shifts the position of the band edge and has a small effect on the effective mass but it affects the valence band structure. In addition to the change in the band gap the energy difference between the light and heavy hole band also changes. Compressive strains moves the bands apart while tensile strain tends to push the bands closer to degeneracy.

In compressive strain, the hole band associated with the lasing transition has a relatively low effective mass. Also, the well depth confining the electrons is deeper in compressive strain. MQW lasers with a compressive strain have been demonstrated experimentally to have low threshold current density significantly higher differential gains both at 1.55μm and 1.3 μm thus resulting in higher modulation speed than bulk lasers[33].

The separation between the band edge and the split off band can be changed by strain as well as the threshold current density and the carrier concentration[4]. Since the Auger rate is proportional to the cube of carrier concentration, the strain changes the Auger rates as well by suppressing the Auger recombination channels in strained quantum well structure which in turn reduces the temperature sensitivity and aids in the design of long wavelength lasers[34].

The gain spectrum of the light for TE polarization is always higher than the TM polarization in an unstrained quantum well, this is the same for the compressive strain but the TM polarization seem to dominate the TE polarization in the tensile strained QW [32]. This might make the compressive strain QW an advantage over tensile strain in some applications.

2.5 InAlGaAs/InP Band Gap Engineering

The $In_{1-x-y}Al_xGa_yAs$ material system lattice matched to InP has been of interest because of the good performance report by researchers (see chapter 3). The $In_{1-x-y}Al_xGa_yAs$ alloy can be grown lattice matched to InP based substrates[32,35], where x and y are parameters defining the composition of aluminium and gallium respectively in the InAlGaAs alloy.

2.5.1 $In_{1-x-y}Al_xGa_yAs$ Quartenary

The energy bandgap and band offset structure of alloys used in the active region of a QW material is the basis of the operational wavelength and the device performance. Therefore, it is necessary to extensively study it during band gap engineering of the InGaAs/InAlGaAs/InP material system.

A schematic presentation of an InGaAs/InAlGaAs QW is shown in Fig. 2-7 below.

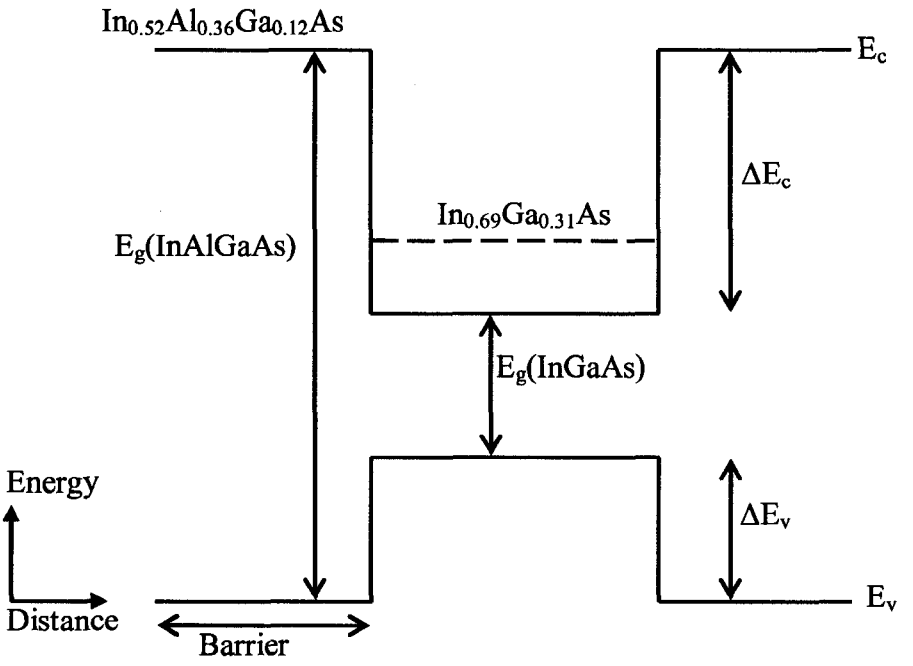

Fig. 2-7 Schematic presentation of an $In_{0.69}Ga_{0.31}As/In_{0.52}Al_{0.36}Ga_{0.12}As$ QW structure.

The energy gap of $In_{1-x-y}Al_xGa_yAs$ lattice matched quaternary system, at 300K, is dependent on the Al and Ga fraction of the alloy, and is expressed using the following equations [14,35]:

$$E_g(x,y) = 0.36 + 2.093x + 0.629y + 0.577x^2 + 0.436y^2 + 1.013xy - 2.0xy(1-x-y) \quad (eV) \quad 2\text{-}33$$

Or

$$E_g(x,y) = 1.424 + 1.455x + 0.191x^2 - 1.614(1-x-y) + 0.55(1-x-y)^2 + 0.043x(1-x-y) \quad (eV) \quad 2\text{-}34$$

Or

The band gap of the quaternary material could be determined if the operating wavelength is given and using the formula:

$$E_g = \frac{hc}{\lambda} \qquad (eV) \qquad 2\text{-}35$$

where c is the speed of light and h is the planks constant.

Using equations 2-33 and 2-35 above to plot the energy bandgap of $In_{0.52}Al_{0.36}Ga_{0.12}As$ as a function of Al composition x and shown in Fig. 2-8. The energy bandgap increases almost linearly with Al composition. The bandgap energy for Al composition of x = 0.36, used in this research for the InAlGaAs barrier layers, is ~1.268eV (at 300K).

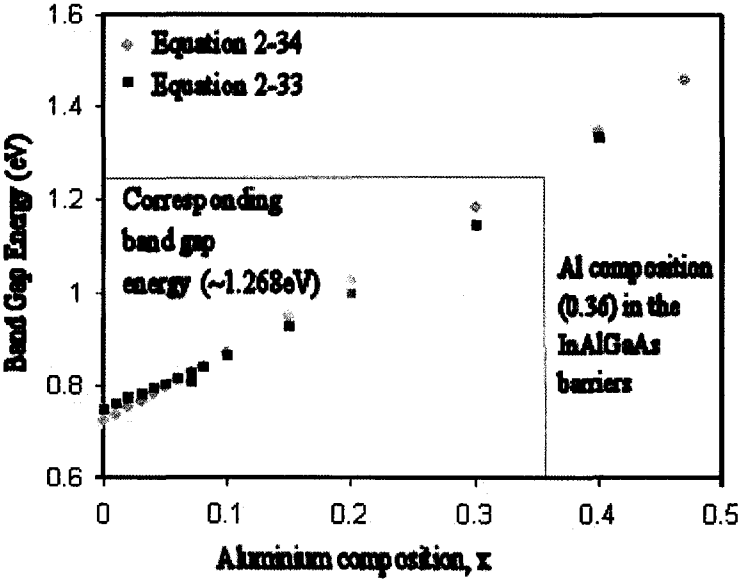

Fig. 2-8 The energy bandgap of $In_{1-x-y}Al_xGa_yAs$ at 300K as a function of Al composition[36]

The lasers studied in this thesis do not contain aluminium in the QWs, so that the emission wavelength can be observed in the longest possible range

Another method to calculate the energy bandgap for the $In_{1-x-y}Al_yGa_xAs$ quaternary system and lattice matched to InP substrate, at 300K is as follows

$$E_g(z) = 0.76 + 0.49z + 0.20z^2 \quad (eV) \qquad 2\text{-}36$$

$$z = \frac{x}{0.48}$$

To obtain some of the other parameters for the $In_{1-x-y}Al_yGa_xAs$ material system, a linear interpolation between three different binary semiconductors, InAs, AlAs and GaAs is used, which can be used to calculate all physical parameters P used in the calculation of the band edge, except for the bandgap[37]:

$$P(In_{1-x-y}Al_yGa_xAs) = P(InAs)(1-x-y) + P(AlAs)x + P(GaAs)y \quad (eV) \qquad 2\text{-}37$$

The material parameters of the binary semiconductors InAs, AlAs and GaAs can be found in the references [14,38].

2.5.2 $In_{1-x}Ga_xAs$ Ternary

Energy bandgap E_g for $In_{1-x}Ga_xAs$ is given as follows[38]:

$$E_g(In_{1-x}Ga_xAs) = 0.36 + 0.505x + 0.555x^2 \ (eV) \qquad 2\text{-}38$$

Ga composition of x = 0.31, used in this research for the InGaAs QW layers, is ~0.57eV (at 300K).

The material parameters, *M*, of $In_{1-x}Ga_xAs$ are interpolated using those for InAs and GaAs by using the following formula:

$$M(In_{1-x}Ga_xAs) = (1-x)M(InAs) + xM(GaAs) \quad (eV) \quad 2\text{-}39$$

2.5.3 InP Binary

InP is a direct bandgap binary alloy commonly used as a substrate for the InAlGaAs/InGaAs material system. The energy bandgap for InP is given below, using a temperature, T, dependent equation:

$$E_g(T) = 1.421 - \frac{T^2 \times 3.63 \times 10^{-2}}{T + 162} \quad (eV) \quad 2\text{-}40$$

The energy bandgap calculated at room temperature is 1.351eV.

2.6 Summary

This chapter reviews the fundamental properties and lasing characteristics in semiconductor diode lasers, as well as the quantum well structure and the band gap analysis of the InAlGaAs material system.

Chapter 3 Background

3.1 Introduction

Short wavelength (~0.7-0.9 μm) GaAs-based lasers and long wavelength (~1.3-1.65 μm) InP-based lasers are currently in production. Advancement in fabrication techniques and device technology has paved way for continuous development of lasers made with new and novel materials to be used for emerging applications.

The application of quantum well structures to semiconductor laser diodes has received good attention because of its small physical footprint and as well as its superior laser characteristics[39]. By controlling the width of the quantum wells, the electron and hole wave function can be adjusted to modify laser characteristics as well as introduce new concepts to optical devices[4]. To achieve better confinement and temperature stability quantum well lasers with more than one well were used.

Though the InGaAsP based laser technology has been extensively studied. The InAlGaAs material has been under active research as an alternative to the conventional phosphorus quaternary lasers because of advantages like higher temperature performance and larger conduction band discontinuity in comparison to phosphorus quaternary lasers[40 41].

The practical use of phosphorus quaternary lasers is impaired by an extreme sensitivity of threshold current to temperature. At room temperature and above, non-radiative Auger recombination is the dominant physical mechanism responsible for such sensitivity. It was

therefore recommended that strained quantum well lasers should show reduced temperature sensitivity due to suppression of Auger recombination channels in these structures[42].

High temperature affects a number of key physical mechanisms in laser diodes, including the optical gain, optical losses, and non-radiative recombination mechanisms[43]. It also reduces the bandgap and the carrier mobility[21].

3.2 Literature Review

Y. Zhang *et al* used Harrison's model and the anisotropic parabolic approximation to calculate the band structure of $In_{1-x-y}Ga_yAl_xAs$ compressively strained quantum wells (QWs) in 1.55 μm wavelength lasers. They investigated the relations between the well width, gain, and composition in a 0.78% compressively strained QW structure and obtained the optimized well number (6) and (7), and the optimized cavity length (850–900 μm) [44]. The well number and the cavity length were optimized to obtain a low threshold and high maximum operating temperature (550–560 K) QW laser[44].

R. Rajasekaran studied the trade-off in the performance of semiconductor lasers with the increase in well number using experimental analysis and numerical simulations with a mode solver to compare the optical confinement in five and seven quantum well InAlGaAs lasers operating at an optical communication wavelength of 1.3 μm. In his thesis work, he also investigated the dependence of laser performance on the waveguide structure and the geometry of the laser device. The seven quantum well InAlGaAs lasers showed better optical

confinement and characteristic temperature compared to the five quantum well lasers. The increase in well number aids in lowering threshold current and improving the optical confinement factor, characteristic temperature, net gain, material gain and d-factor with trade off in slope efficiency, differential quantum efficiency and cavity loss[4]. Seven quantum well InAlGaAs lasers exhibited low threshold current of 13.8mA and high characteristic temperature of 71°C. The five quantum well lasers showed high slope efficiency of 0.198W/A and a low cavity loss of 18/cm.

J. Piprek *et al* investigated what limits the maximum output power of long-wavelength AlGaInAs/InP laser diodes. They analyzed the high-temperature continuous-wave performance of 1.3 μm AlGaInAs/InP laser diodes grown by digital alloy molecular-beam epitaxy using Crosslight laser software - that self-consistently combines quantum-well bandstructure and gain calculations with two-dimensional simulations of carrier transport, wave guiding, and heat flow. Excellent agreement between simulation and measurements was obtained by careful adjustment of material parameters in the model. Joule heating was shown to be the main heat source; quantum-well recombination heat was almost compensated for by Thomson cooling and Auger recombination was the main carrier loss mechanism at lower injection current. Vertical electron escape into the p-doped InP cladding dominates at higher current and caused the thermal power roll-off. They showed quantitatively that this roll-off was caused by an escalation of the electron leakage from the active region due to self-heating. The reduction of optical gain with temperature elevation was the triggering mechanism of this leakage escalation[21]. Modification of facet coating, p-doping, and waveguide design, as well as the inclusion of an electron-stopper layer, lead to a significant increase of the maximum output power. They showed that a detailed study of laser performance and

limitations can be successful by using a combination of measurement and simulations[21].

There have been efforts to quantify the amount of lateral current spreading present and originating from the epitaxial layers of laser devices. G. Letal *et al* developed an analytical model to evaluate the impacts of lateral current spreading on the performance of MQW InGaAsP/InP RWG lasers. They reported that the lateral current spreading in narrow ridge width lasers of less than 5 μm is significant and about 42% of the injected current leaks from the from the index-guided region at threshold for a 2 μm ridge width laser[45]. Belenky *et al* measured gain/loss and modelled the optical confinement in buried Heterostructure lasers with different widths, they concluded that about 30% of threshold current in single mode devices does not contribute to active region pumping[46]. D. Ban *et al* reported results of a two-dimensional local voltage measurement of the transverse cross section of operating multi-quantum well ridge RWG lasers using scanning voltage microscopy technique. They observed a lateral non-uniformity of local voltage in the n-cladding layers of the laser and attributed the voltage variation to 2D carrier transport effect within the RWG lasers. The quantitative evaluation of this effect indicated the local vertical current density to be ~40% smaller at the edge of the ridge than at its center[47].

M. Jain *et al* investigated the spectral gain measurements for two InGaAs-InAlGaAs multiple width quantum well structures, with inverse-configured active regions. Using two structures, one consisted of wide quantum wells near the p-side and narrow quantum wells near the n-side of the active region while the other structure consisted of narrow quantum wells near the p-side of the active region with wider quantum wells near the n-side. They showed that for the same operating

conditions, the structure with wide quantum wells on the p-side of the active region provided a 15% broader gain spectrum in comparison to the structure with narrow quantum wells on the p-side of the active region. The analysis of the results also showed non-uniform carrier distribution across the active region of the structures, where the structure with wide quantum wells near the p-side of the active region provided 65% more gain in comparison to the structure with narrow quantum wells near the p-side of the active region[48]. They compared the gain distribution result with that obtained for the phosphorous quaternary structures in other literature and came up with the conclusion that the gain distribution is more uniform in aluminium quaternary than phosphorous quaternary material[48].

A multisection device technique was employed by M. Jain to carry out internal optical loss measurements in two types of InGaAs–InAlGaAs quantum wells structures. One structure consists of conventional identical-width quantum wells (IWQW) and the other, a broader spectral-width material, consists of multiple-width quantum wells (MWQW) in the active region. The results showed a small increase in internal loss obtained for the MWQW structure, in comparison to the IWQW structure[49], implying that the internal optical loss does not show a significant increase by inclusion of multiple-width wells in its active region. Both structures showed losses being temperature dependent below the band edge[49].

Characterization of temperature sensitivity of gain and recombination mechanisms in 1.3-μm AlGaInAs MQW lasers was carried out by T. J. Houle *et al,* they investigated the potential of 1.3-μm AlGaInAs multiple quantum-well (MQW) laser diodes for uncooled operation in high-speed optical communication systems experimentally by evaluating the temperature dependence of key parameters such as the threshold

current, transparency current density, optical gain and carrier lifetime. Detailed measurements performed in the 20 – 100 °C temperature range indicated a localized T_0 value of 68 K at 98 °C for a device with a 2.8 μm ridge width and 700-μm cavity length. The transparency current density was measured for temperatures from 20 to 60 °C and found to increase at a rate of 7.7 $A.cm^{-2}.°C^{-1}$. Optical gain characterizations showed that the peak modal gain at threshold is independent of temperature, whereas the differential gain decreases linearly with temperature at a rate of 3 x 10^{-4} $A^{-1}.°C^{-1}$. The differential carrier lifetime was determined from electrical impedance measurements and found to decrease with temperature. From the measured carrier lifetime they derive the monomolecular (A), radiative (B), and nonradiative Auger (C) recombination coefficients and determined their temperature dependence in the 20 – 80 °C range[50]. Their study showed that A is temperature independent, B decreases with temperature – since thermal broadening drives the temperature down, and C exhibits a less pronounced increase with temperature[50].

To investigate the uneven carrier distribution in multi quantum wells, Tessler *et. al.* theoretically presented a carrier dynamic model with the consideration of electron-hole interaction [29,51]. The model yielded a non-uniform carrier distribution along the crystal growth axis. Hangleiter *et. al.* further improved the understanding of carrier dynamics in QWs [52]. They indicated that the slow transport of hole between individual QW leads to a strong inhomogeneous carrier distribution, they also compared the carrier unevenness in InGaAsP and InGaAs QWs and suggested that the InGaAs/InGaAlAs QWs is better in terms of performance due to its band discontinuity that can speed up hole transport[29,51].

3.3 Summary

This chapter reviewed relevant researches in the field of InAlGaAs semiconductor laser to include but not limited to threshold density, gain, loss, thermal effects and efficiencies.

Chapter 4 InAlGaAs Characterization

4.1 Introduction

Laser devices are characterized using the device station facilities available in the Photonics Technology Lab at the school of Information Technology (SITE 3040), University of Ottawa. The computer-controlled device test station allows for geometry and temperature dependent characterization of the calibrated power output and also current, spectra, loss, gain, resistance and other measurements.

This chapter analyzes and examines the quality, performance and characteristics of the InAlGaAs laser devices being researched. The first section briefly describes the device structure as well as the analytical methods and measurement techniques used during the laser parametric tests. The later sections present the results of the analysis.

The light current (L-I) characteristic is measured for laser devices with different cavity lengths and ridge widths. The geometry-dependent L-I analysis is used to extract other parameters such as the threshold current density, slope efficiency, and external and internal quantum efficiency. The thermal stability of the laser is studied by measurements taken at various temperatures.

Optical spectroscopy of the laser is used to analyze emission characteristics of the laser devices. From the spectra, wavelength red-shift over bias current and temperature are analyzed. The spectra measurements were taken at different bias currents and temperatures.

The non-uniformity in the data plots could be an indication of fabrication variations and imperfections across the wafer, spontaneous emission noise, vibration of the test setup, noise in the instruments, coupling inefficiencies and human error.

4.2 Experimental Setup

The experimental setup is composed of laser stage, optical spectrum analyzer, photo detector/power meter, lensed fiber, thermoelectric cooler (TEC) and TEC controller, rotational stages/positioners, source meter, piezoelectric controller, infra-red viewer, microscope, GPIB cables and a computer for data acquisition.

The laser stage is a combination of heat sink, probes and a microscope. The heat sink stage is composed of a XYZ stage, copper plate, brass sample holder and thermoelectric cooler. A thermo epoxy resin was used to bond the copper plate and the TE cooler. The stage is built so that when the temperature is varied there is a uniform distribution of heat on the copper plates where the brass sample holder is placed. The lasers were injected with currents between 0 – 200 mA using the Keithley 2400 source meter through tungsten needle probes directly applied to the contact above and through alligator clips to the brass sample holder below.

Light from the laser device is either incident on a power detector or averaged to obtain a precise power measurement, or focused into a single mode lensed fiber connected to an optical spectrum analyzer (OSA) for spectral measurement. The lensed fiber is used to optimize maximum

coupling of light, as loss due to coupling of light through the fiber is a major drawback in the setup.

All measurements are collected through a GPIB bus and automatically processed using a specifically built in VI (Virtual Instrument) LabVIEW 8.0 program to acquire data. Further graphical analysis is done by exporting the data into Matlab.

The optical power detector used is a wide area Ge detector and a Newport 818-IR, and the OSA is an HP 70950B. During the measurement, temperature was actively controlled by a Melcor thermoelectric cooler (TEC) controller and a Keithley 2510-AT auto-tuning TEC source meter. A Keithley 2400 multi-meter measured the applied bias current and voltage across laser diodes and a Newport 1830-C power head measured the power from the front facet. The lensed fiber is 1 m single mode fiber (SMF) with a coupling efficiency of 45% at 1550 nm and connecterized to a FC/PC connector. The temperature of the stage was varied from 25°C to 70°C, with the temperature fluctuation in the laser stage determined to be ±1°C.

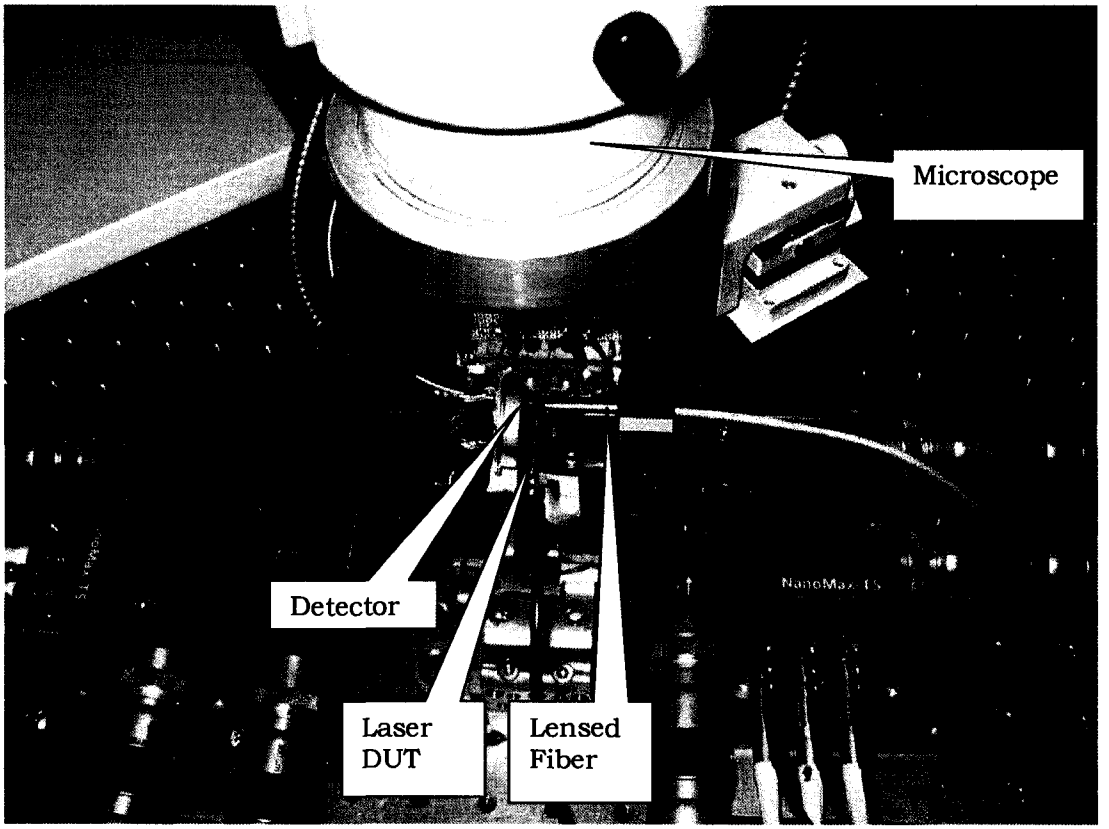

Fig. 4-1 Picture of the experimental setup.

The drawbacks of the experimental setup are that the laser is not isolated from the ambient light, temperature and vibrations, and there are losses incurred due to coupling of light through the lensed fiber. The ambient light detected on the wide area detector however is negligible between at 62 nW. Care was taken to optimize the alignment of the setup. Piezo-electric controllers were used to control the nano-positioning and alignment of the experimental setup.

The experiment is carried out for laser devices on bars with cavity lengths – 555, 1270, 1524 and 2200 μm. Each bar consists of different sets of ridge widths – 1.2, 1.6, 2.0, and 2.4 μm.

Fig. 4-1 and Fig. 4-2 shows the pictorial and the simplified schematic of the experimental setup respectively.

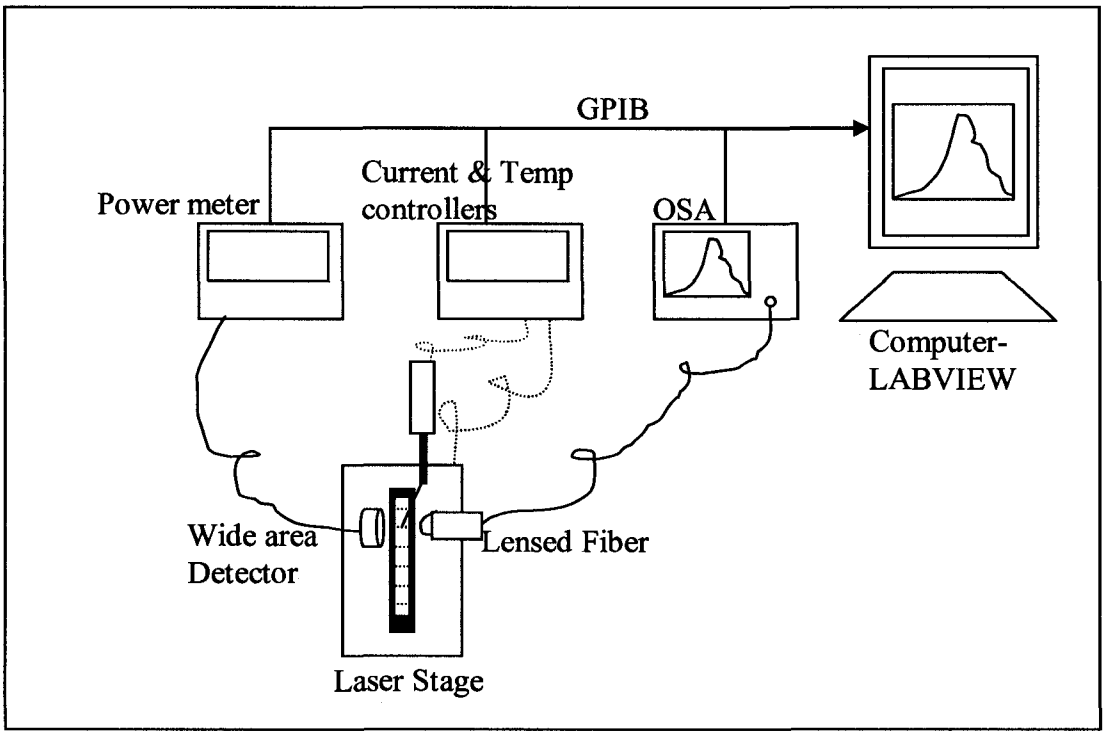

Fig. 4-2 Schematic of the experimental setup.

4.3 Light-Current Characteristics

L-I measurements are carried out for devices with different ridge widths and cavity lengths on selected laser bars. The devices were measured under continuous wave current injection state. A germanium based calibrated wide area detector collects the output light from the front facet of laser device under test.

From here the slope efficiency of each facet and the corresponding external quantum efficiency are calculated. The threshold current increases linearly with cavity length and roughly linearly with ridge width

and slope efficiency increases within the same cavity length. The resistance is evaluated from the IV characteristic. Injection currents of 0 – 200 mA are used but some of the laser devices saturate at lower injection currents. This demonstrates a strong dependence of threshold current and output power on the cavity length and ridge width. The ratio of total optical power over the total applied electrical power equals the wall plug efficiency.

The intercept of the linear regressions derived by plotting the threshold current as a function of the ridge width gives the lateral leakage current. The slope of the same linear regressions gives the threshold current density. L-I measurements based on the laser cavity lengths are used to determine the laser external quantum efficiency, internal quantum efficiency, internal loss and optical gain.

Laser temperature dependent analysis is based on the variation of a laser threshold current and the slope efficiency over temperature. The threshold current increases with temperature. However, the temperature range is limited by the capacity of the TEC (70°C) used in the test station and most importantly the characteristic temperature of the laser devices.

4.3.1 Geometric Dependent Characteristics

LI characteristics measured at three different wavelength settings (1675, 1700 and 1725 nm) of the optical power meter for the 1270 μm device with 1.6 μm ridge width at 25°C show slight differences at the different wavelengths.

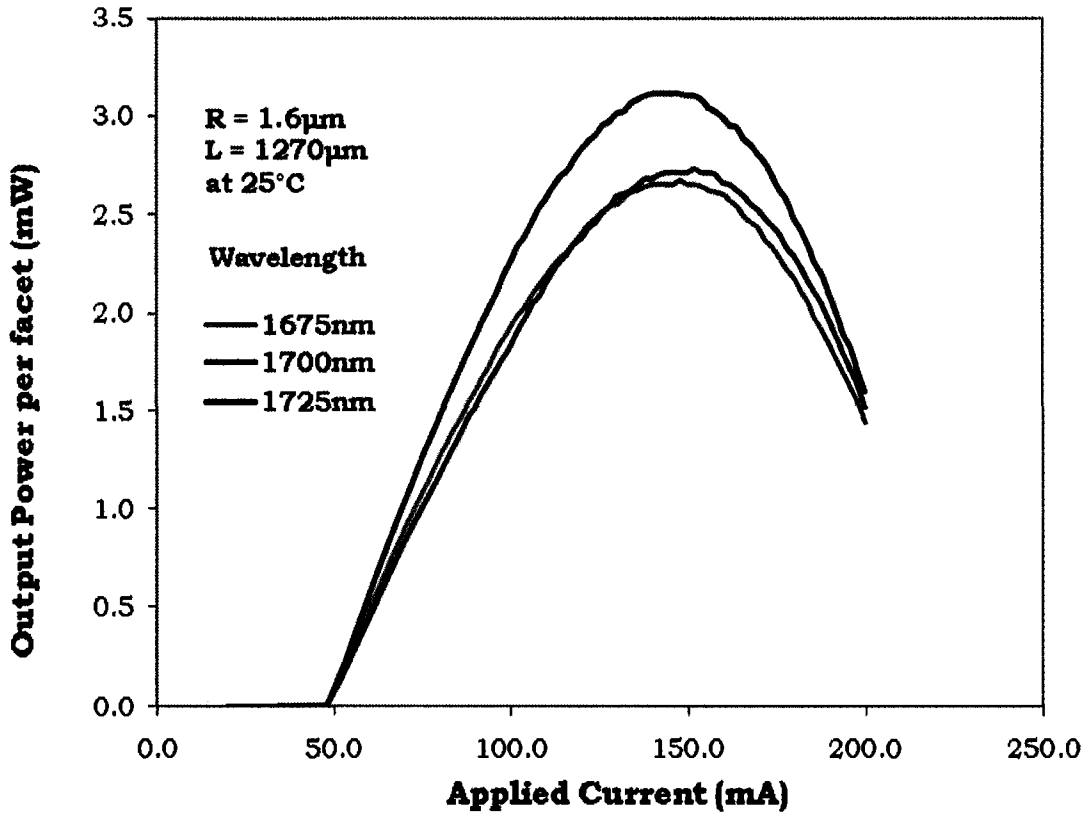

Fig. 4-3 L-I characteristics of 1.6 x 1270 μm device measured under three different wavelength settings of the power meter

Fig. 4-3 shows the LI characteristic at the different wavelength settings. The threshold current remains the same 48 mA at all wavelength settings but the output power per facet varies, with the highest power recorded using the 1725 nm wavelength setting due to variation in modal confinement. The 1675 nm and 1725 nm wavelengths saturate at 2.67 mW and 2.73 mW respectively.

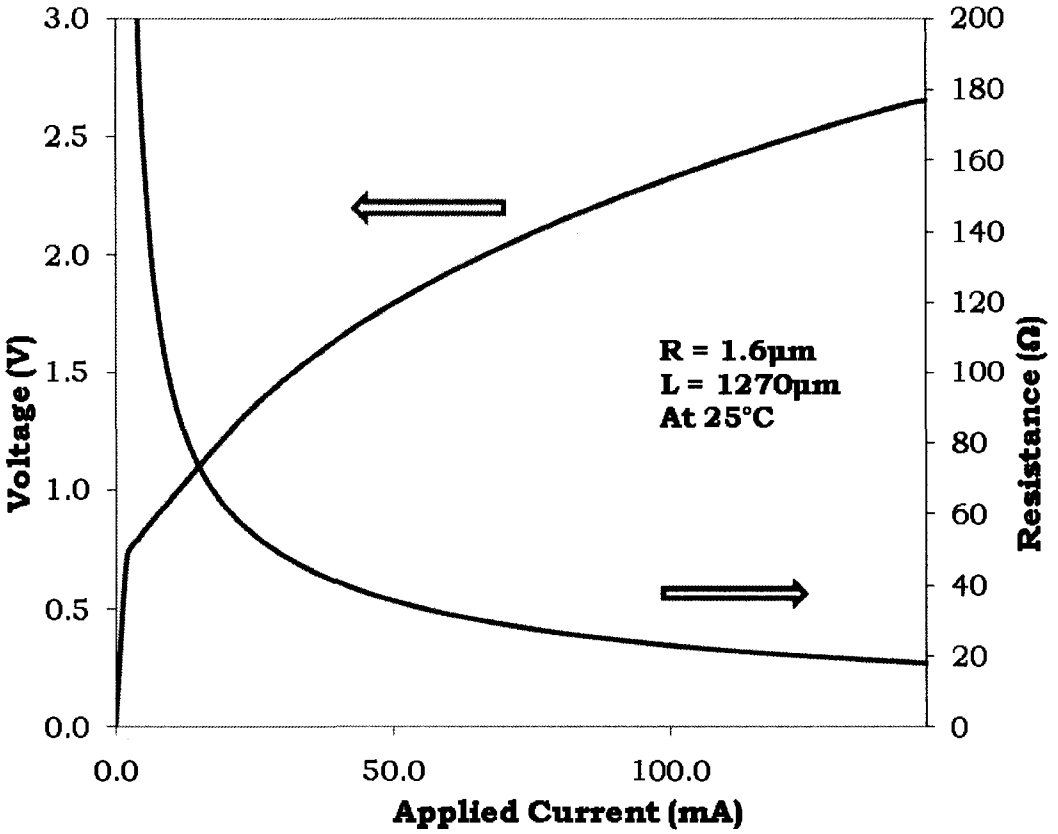

Fig. 4-4 R-I-V characteristics of 1.6 x 1270 μm device

The output power at the 1725 nm wavelength setting saturates at an applied current of 148 mA, with a maximum power of 3.11 mW. At an injected current of 148 mA, the voltage is 2.72 V, for an electrical input power of 403 mW, giving a wallplug efficiency of 0.77% for a single facet and 1.55% for both facets. The wall plug efficiency is calculated using the ratio of total optical power over the electrical power. The series resistance saturates at about 18 Ω as shown in Fig. 4-4

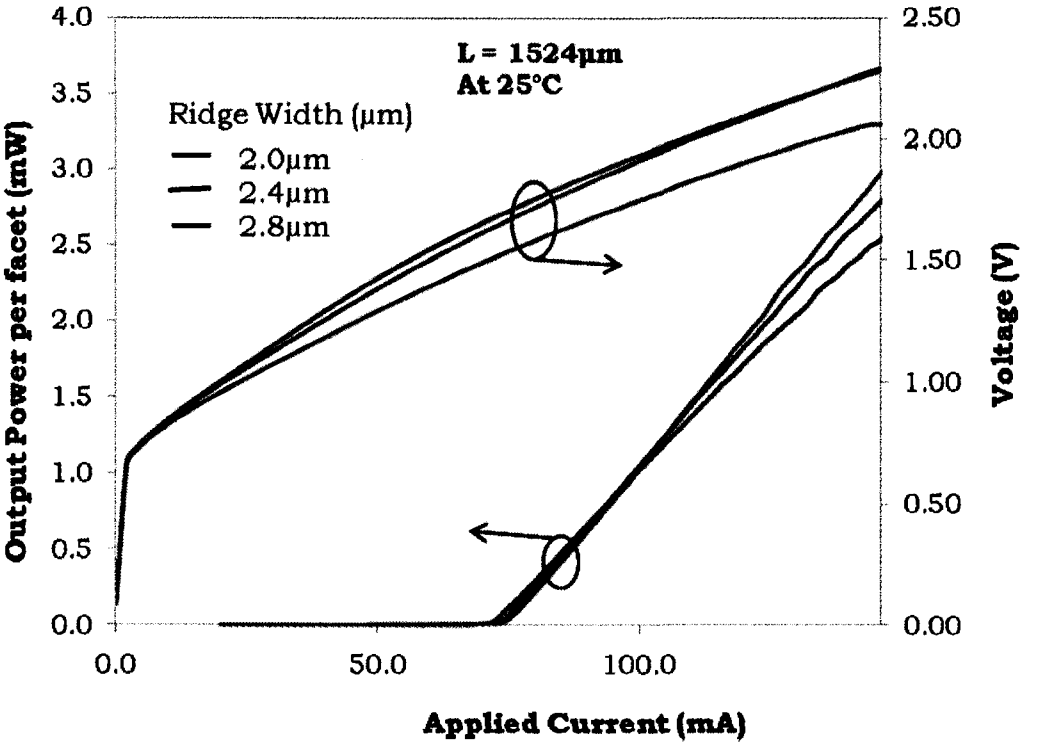

Fig. 4-5 L-I characteristics measured for 1524 µm laser device with varying ridge widths.

Fig. 4-5 shows the L-I-V characteristic at 1700 nm for a 1524 µm laser at 2.0 µm, 2.4 µm and 2.8 µm ridge widths (excluding the very narrow 1.2 µm and 1.6 µm ridge widths). The threshold current as a function of ridge widths varies from 69 mA (2.0 µm), 74 mA (2.4 µm) and 82 mA (2.8 µm) respectively.

For the 2.8 µm ridge width, at an injected current of 100 mA, voltage is 1.75 V, for electrical input power of 175 mW and output power of 1mw, giving a wallplug efficiency of ≈ 1.2% for both facets. At injection currents of 120 mA and 146 mA, voltages are 1.9 V and 2.06 V with electrical input power of 228 mW and 308 mW respectively and output powers of 1.9 mW and 3.0 mW, giving wallplug efficiencies of approximately 1.7% and 2.0% (for both facets). It therefore shows a small

but significant increase in wallplug efficiency for increasing applied current.

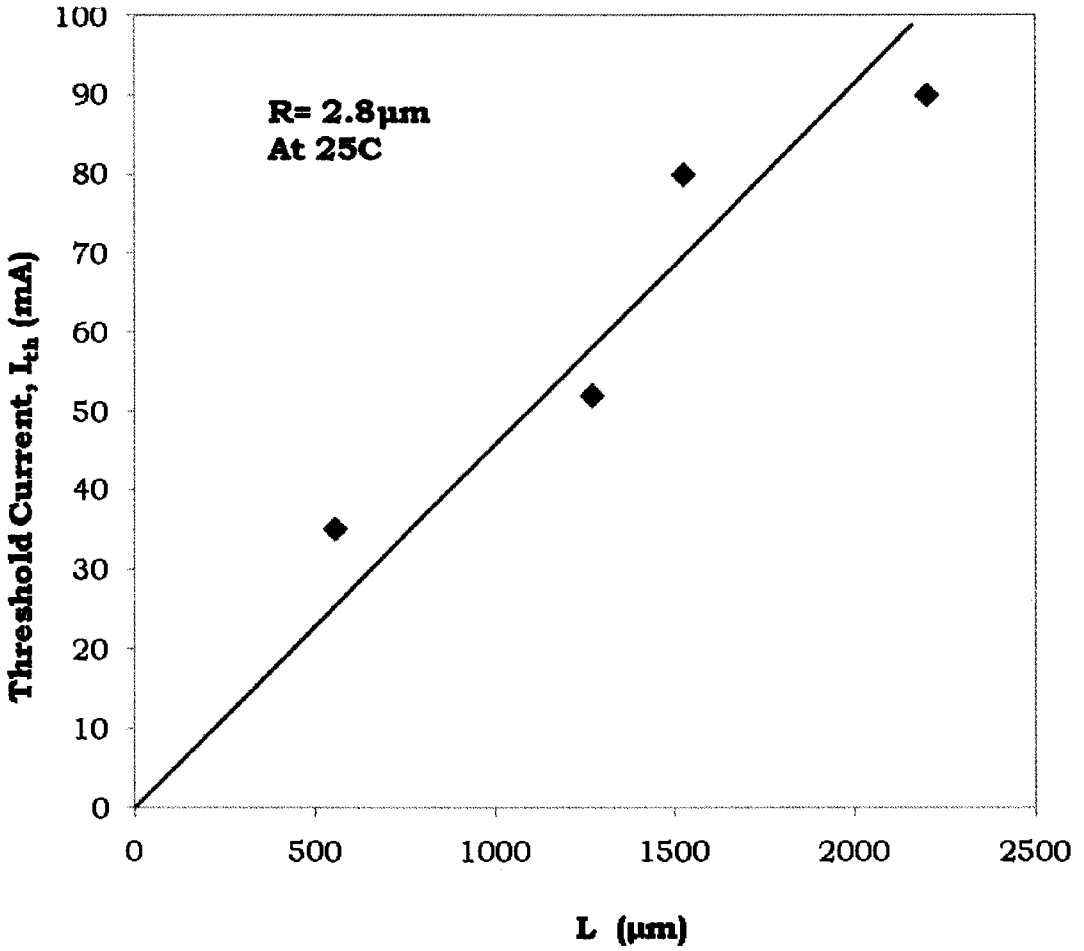

Fig. 4-6 Threshold current as a function of the cavity length for 4 different cavity length laser devices.

The threshold current increases linearly with the cavity length (Fig. 4-6), the uncertainties is between ±5 mA. The increase in threshold current with cavity length agrees with theory because longer cavity lengths implies longer time for facet-to-facet reflection and thus require higher injection current for gain to equal the losses.

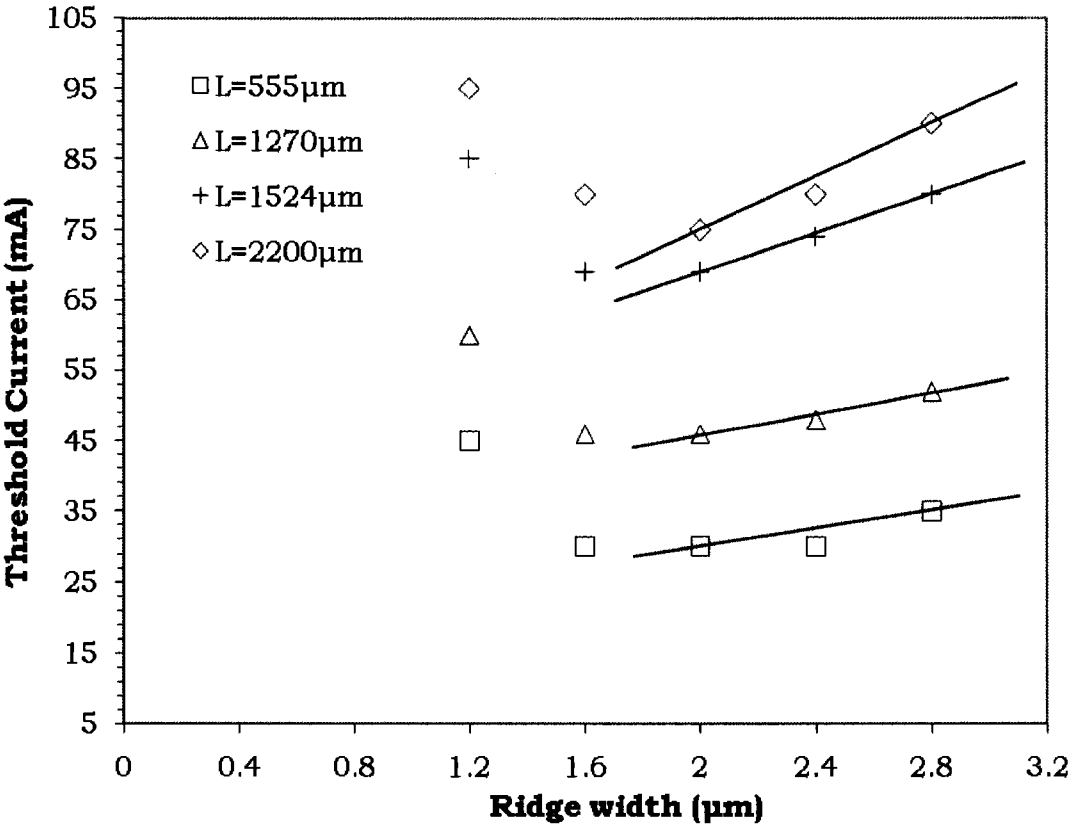

Fig. 4-7 Threshold currents as a function of the laser ridge width for different cavity length lasers.

The threshold current increases almost linearly with ridge width (Fig. 4-7) excluding the 1.2 μm and 1.6 μm ridge widths. However, better linearity is observed between the 2.0 and 2.8 μm ridge widths for longer cavity lasers (1524 and 2200μm). The very narrow 1.2 μm and 1.6 μm ridge width data plots are not taken into account for the fitting because of their high threshold current which is due to non-optimal waveguiding in the active region and self heating of the devices. The ridge widths in the laser devices for this thesis are quite narrow and therefore analysis is based on narrow ridge width lasers.

In Fig. 4-7 the intercept of the linear regressions gives the lateral leakage current, and the slope of the line gives the threshold current

density with leakage correction, using the approximate formula for ridge lasers (equation 2-10). Table 4-1 presents the results of the estimated lateral leakage currents and the threshold current densities with and without leakage corrections.

Table 4-1 The calculated lateral leakage current and threshold current density for different cavity lengths and ridge widths.

R (μm)	L (μm)	1/L (cm^{-1})	I_{th} (mA)	With leakage correction			Without leakage correction	
				I_{leak} (mA)	J_{th} (Acm^{-2})	Ln(J_{th})	Jth (Acm^{-2})	Ln(J_{th})
2.0	555	18.0	30	12	1620	7.39	2700	7.90
	1270	7.87	46	18	1100	7.00	1810	7.50
	1520	6.56	69	27	1380	7.23	2260	7.72
	2200	4.55	75	30	1020	7.07	1710	7.44
2.4	555	18.0	30	8	1650	7.41	2250	7.72
	1270	7.87	48	15	1080	6.99	1580	7.36
	1520	6.56	74	24	1370	7.22	2020	7.61
	2200	4.55	80	28	985	6.89	1520	7.32
2.8	555	18.0	35	8	1740	7.46	2250	7.72
	1270	7.87	52	15	1040	6.95	1460	7.29
	1520	6.56	80	24	1310	7.18	1880	7.54
	2200	4.55	90	28	1010	6.91	1460	7.30

The results show that threshold current density decreases with increasing cavity length and the leakage current increases with longer cavity length laser devices.

The threshold current density as a function of the reciprocal cavity length is shown in Fig. 4-8 with and without the leakage current correction. The natural log of the threshold current density increases with the inverse of the cavity length. Without leakage current correction, the threshold current density is higher. As observed in the Fig. 4-8 and

in Table 4-1, the device with a cavity length of 1270 and 1524 μm deviates a bit from the linear trend, it could be due to fabrication imperfections.

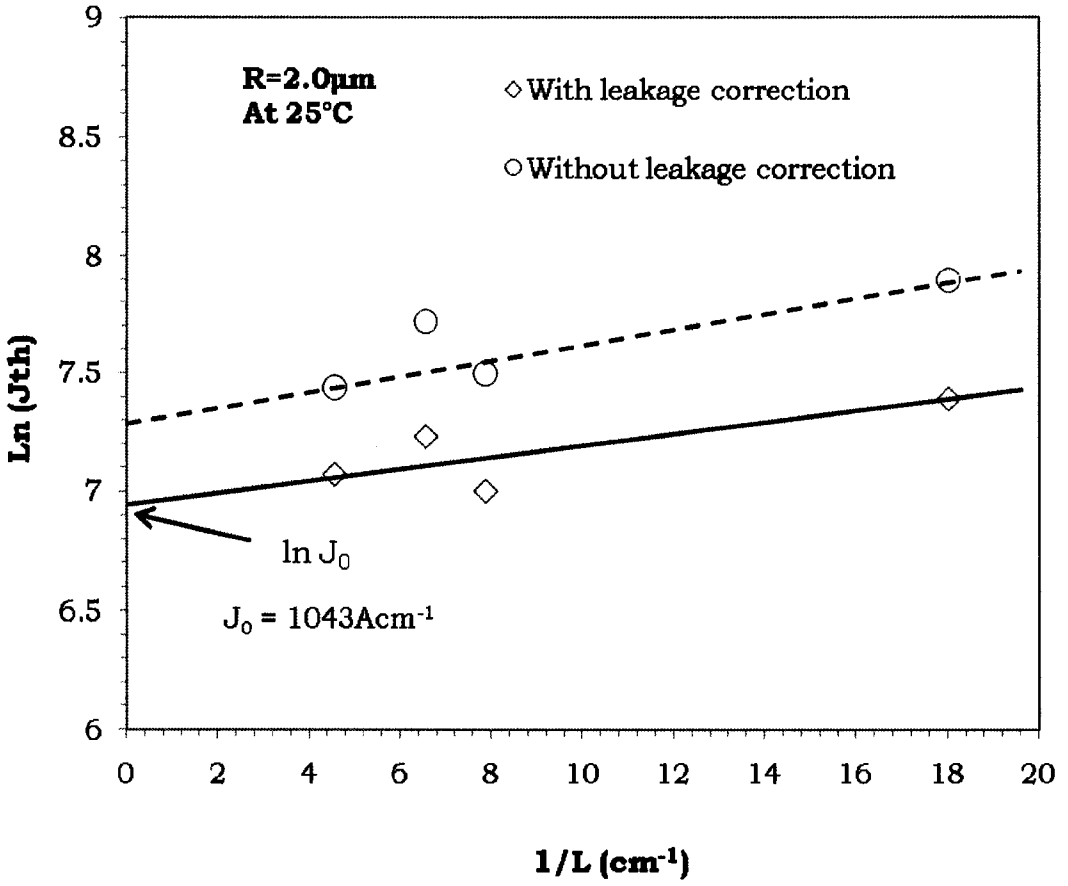

Fig. 4-8 The threshold current density as a function of the reciprocal cavity length.

Two sets of results are presented in Fig. 4-8, one has a leakage current correction, meaning the threshold current density is the difference between the measured value and the lateral leakage current density. The intercept of the linear regression gives the transparency threshold current density J_o which is 1043 Acm^{-1}.

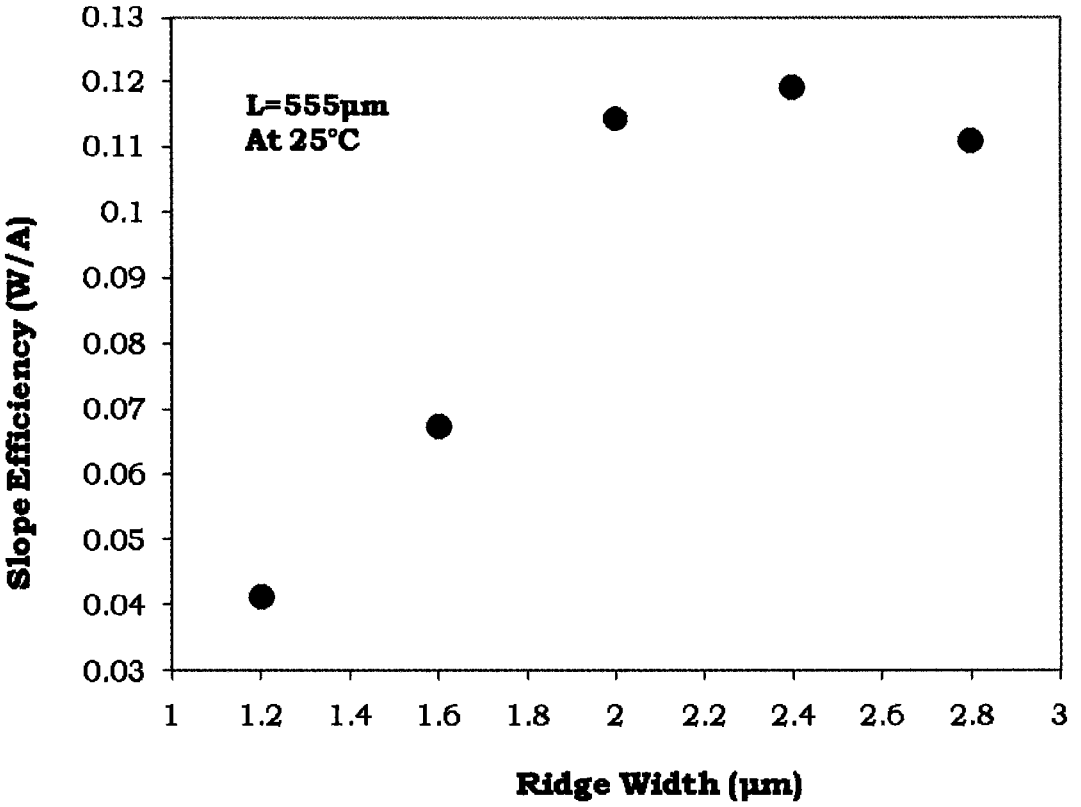

Fig. 4-9 The slope efficiency as a function of ridge width for the 555 µm cavity length lasers.

For the 555 µm cavity length device, the slope efficiency varies in the cavity length for different ridge widths as shown in Fig. 4-9. The slope efficiency is estimated from the linear regression of the L-I plot.

To compare the slope efficiencies for different cavity lengths, the slope of the linear part of the L-I plots are used. Equation 2-19 is then utilized to calculate the external quantum efficiency for the four MQW laser devices. The results for the 2.0, 2.4 and 2.8 µm ridge widths are tabulated in Table 4-2 below.

Table 4-2 The calculated slope efficiency and external quantum efficiency for varying cavity lengths.

Ridge Width, R(μm)	**Cavity Length, L(μm)**	**Slope Efficiency,** $2\frac{\Delta P}{\Delta I}$ **(A/W)**	**External Differential Quantum Efficiency, η_d (%)**	**1/ η_d**
2.0	555	0.114	15.5	6.43
	1270	0.092	12.6	7.97
	1520	0.086	12.0	8.52
	2200	0.060	8.20	12.3
2.4	555	0.119	16.2	6.18
	1270	0.103	14.0	7.17
	1520	0.082	11.1	9.01
	2200	0.081	11.0	9.11
2.8	555	0.111	15.1	6.64
	1270	0.080	10.9	9.20
	1520	0.078	10.6	9.43
	2200	0.072	9.80	10.3

The results show a decrease in slope efficiency as well as external quantum efficiency with longer cavity lengths but there is no trend when comparing with the different ridge widths, a trend would be observed if the very narrow ridge widths (1.2 and 1.6μm) were included in the table. Fig. 4-9 had earlier compared the slope efficiency for all the ridge widths in a 555 μm laser bar.

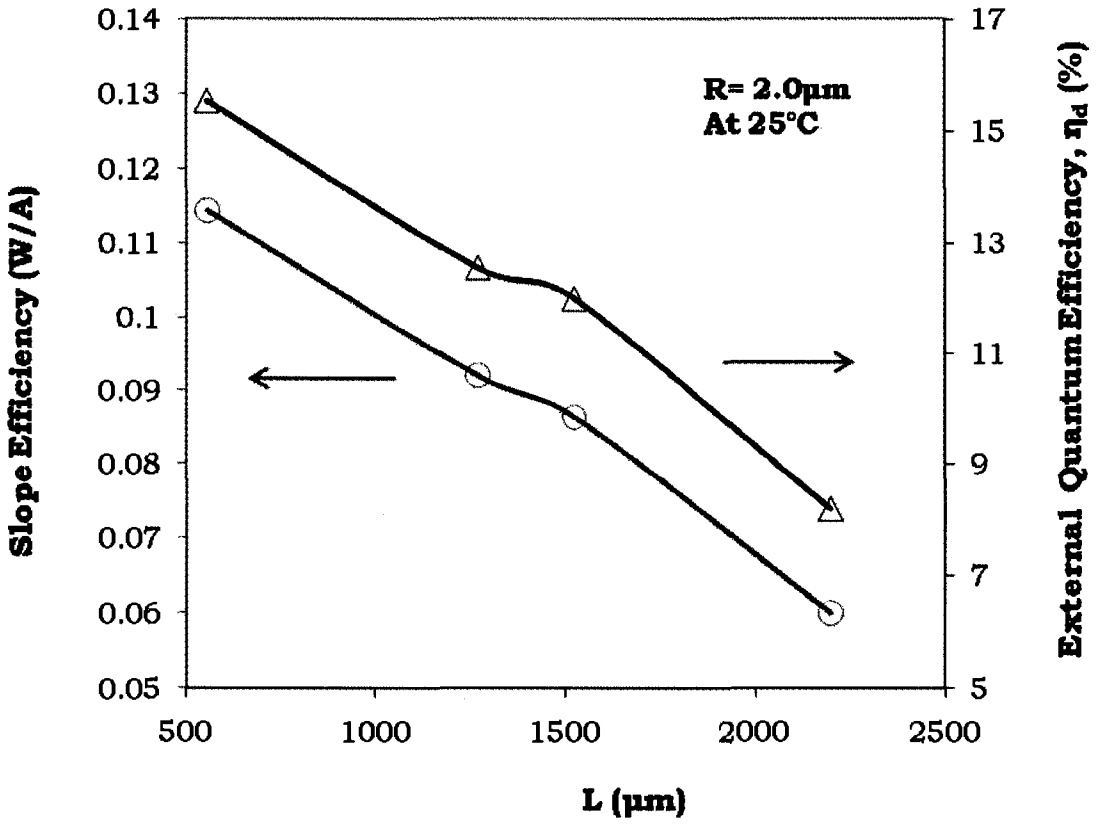

Fig. 4-10 The slope efficiency and external differential quantum efficiency as a function of cavity length for the 2.0 μm ridge width laser devices.

Fig. 4-10 shows a plot of the slope efficiency and the external differential quantum efficiency as a function of the cavity length. The efficiencies as shown in Table 4-2 and Fig. 4-10 decreases with increased cavity length because photons in longer cavity lasers tend to remain inside the cavity for a longer period of time, rather than being emitted from the laser.

The analysis shows that the shorter cavity length lasers have better response to lasing, apart from the lower threshold current it exhibits, it has better slope efficiency showing that for small increase in the injection current it exhibits rapid increase in the output light emission in order

words it has a good conversion rate of input electric power to output light power.

The external differential quantum efficiency, η_d indicates the percentage of the injected current that has been converted to the output light being emitted from the laser, this is done by comparing the slope of the measured L-I plots above threshold current with the slope of the L-I curve of the perfect (100% efficient) theoretical device as explained in equation 2-19.

The highest quantum efficiency calculated is between 15% - 16% for 555 μm devices indicating that most of the electron-hole pair recombinations does not result in the generation of photons but other unwanted forms of energy such as heat, it could also mean that due to design or fabrication imperfections some of the photons are being re-absorbed by the laser structure.

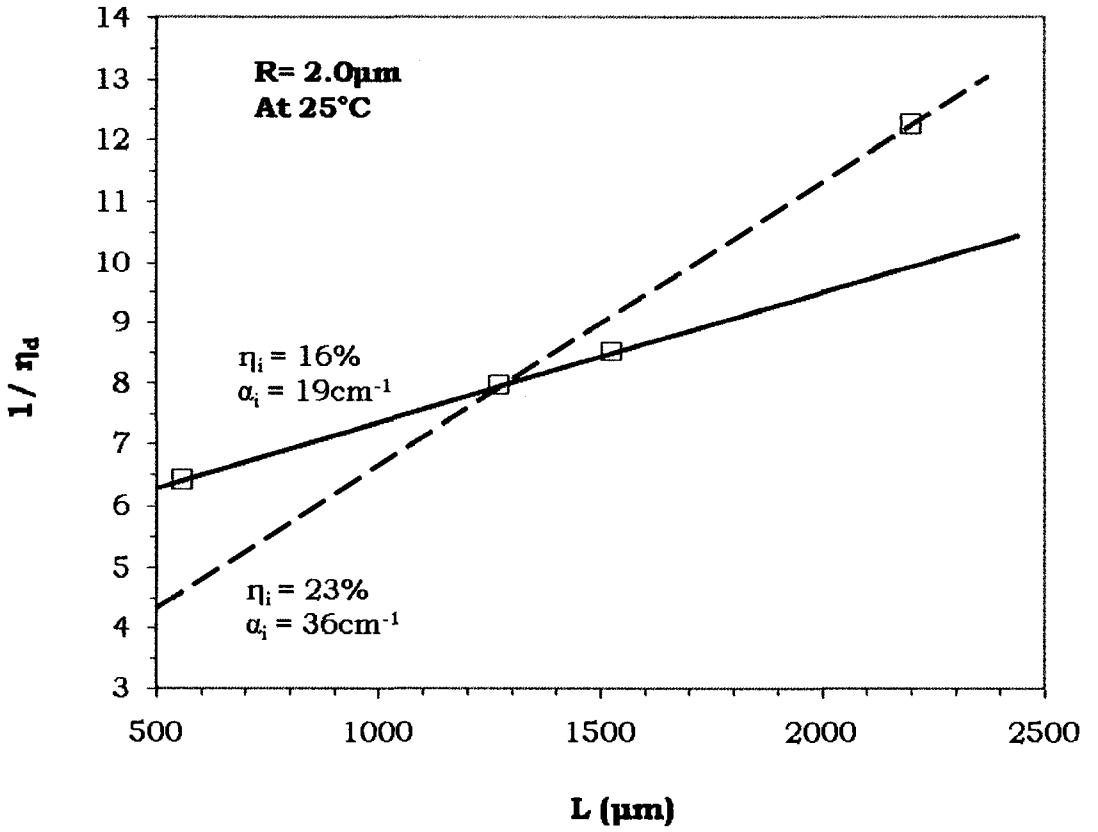

Fig. 4-11 The reciprocal of external quantum efficiency as a function of cavity length for the 2.0 μm ridge width laser devices.

Fig. 4-11 plots the inverse external quantum efficiency as a function of the laser cavity length. As explained in equation 2-19, the linear regression of the reciprocal external quantum efficiency ($1/\eta_d$) to cavity length (L) results in the laser internal quantum efficiency, η_i, and internal loss, α_i. The y-intercept of the linear line gives the inverse of the internal quantum efficiency, the internal loss, α_i is equal to the slope of the line multiplied by (η_i)ln(1/R).

The internal quantum efficiency parameter is a measure of the efficiency of a laser in converting injected current into light within the laser diode structure. From the analysis η_i is determined to be 16% (bold line) and 23% (dashed line), this difference is because of the fitting, the

bold line does not take into account the longest cavity length (2200 μm) while the dashed line excludes the shortest cavity length (555 μm). From the estimation, the bold line seems to be a better fit and including the longest cavity over estimates the internal quantum efficiency and the internal loss. These implies that only these percentages of the electron-hole pairs generated within the laser is actually converted into photons, and therefore the internal loss (made up of many loss mechanisms) is quite high at a value of 19 cm^{-1} and 36 cm^{-1}. All these further indicate the poor laser structure design and fabrication. From theory the internal quantum efficiency should have a higher value than the external quantum efficiency and this is confirmed with our experimental results.

4.3.2 Temperature Dependent Characteristics

In order to measure the characteristic temperature of a laser it is necessary to experimentally measure the LI characteristic of a laser at various temperatures. The same experimental setup described in the above section is employed. The temperature is varied and monitored using the TEC controller. The copper plate heat sink stage assembled provides a uniform distribution of temperature on the surface of the stage. The temperature is varied from (25°C – 70°C) and the corresponding characteristic L-I curve for each laser device is plotted. From these experimentally measured L-I curves the characteristic temperature of the device is determined by plotting the natural logarithm of threshold current density J_{th} versus the temperature, and then measuring the slope of the linear regression.

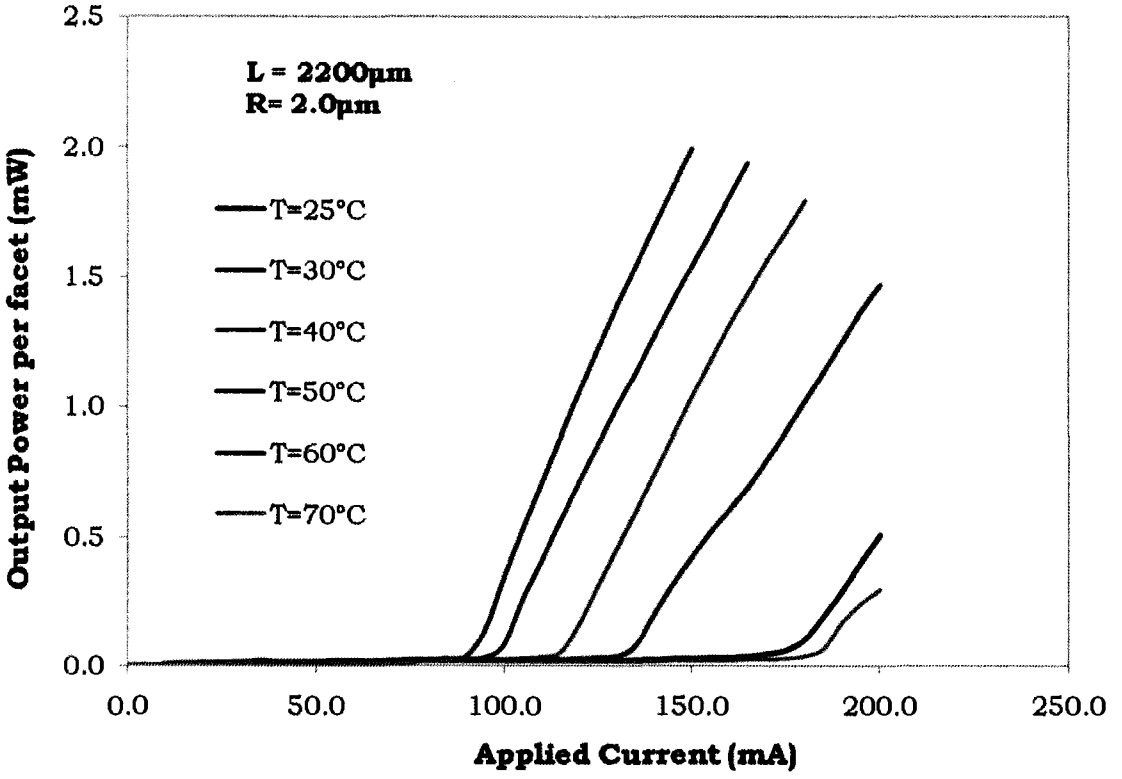

Fig. 4-12 L-I characteristics measured at varying temperature for 2.0 x 2200 µm laser device.

Fig. 4-12 and Fig. 4-13 clearly shows an increase in threshold current with the increase in temperature and the maximum power as shown decreases with increasing temperature and the linearity of the output powers at higher temperatures are also limited. The longer 2200 µm device survived the heating up to the 70°C temperature unlike the smaller 555 µm device that degraded completely after 40°C.

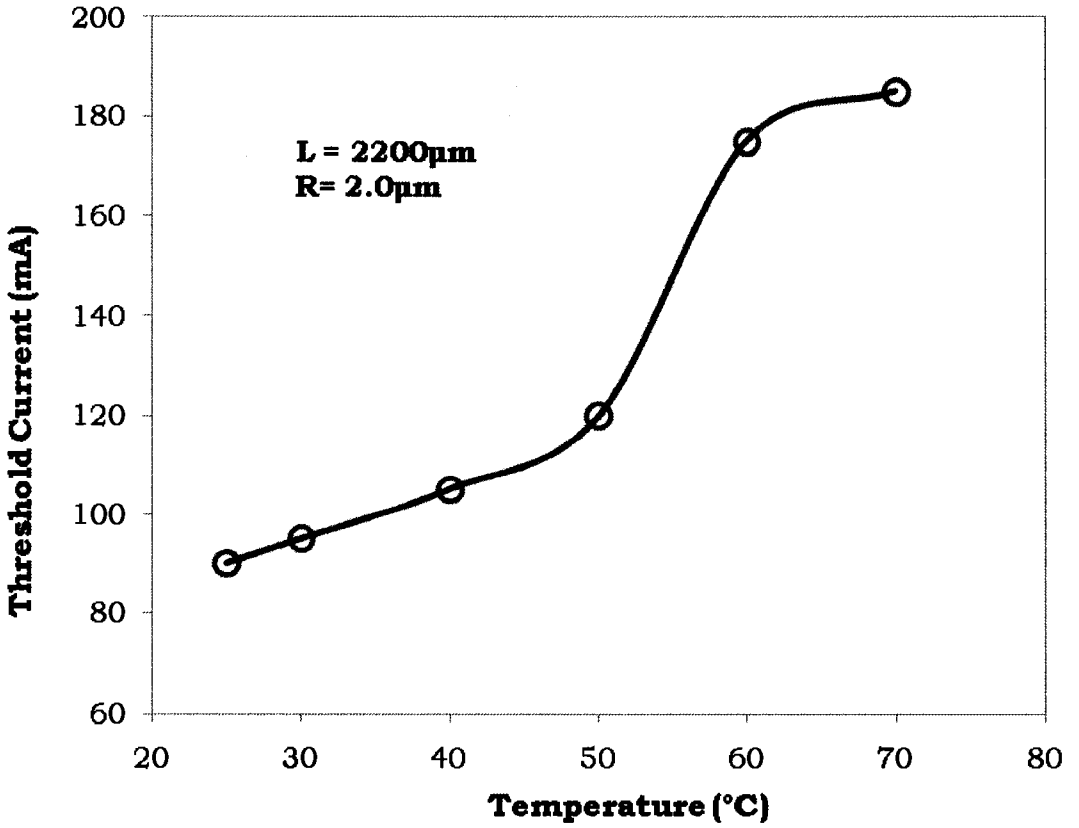

Fig. 4-13 Threshold current as a function of temperature for 2.0 x 2200 µm laser device.

Table 4-3 The calculated threshold current density for varying temperatures in the 2.0 µm ridge width of the 2200 µm and 555 µm laser devices.

	2200µm			555µm		
Temp (°C)	**I_{th} (mA)**	**J_{th} (Acm^{-2})**	**Ln J_{th}**	**I_{th} (mA)**	**J_{th} (Acm^{-2})**	**Ln J_{th}**
25	90	2050	7.62	25	2250	7.72
30	95	2160	7.67	30	2700	7.9
40	105	2390	7.78	40	3600	8.19
50	120	2730	7.91	-	-	-
60	175	3980	8.29	-	-	-
70	185	4210	8.34	-	-	-

The characteristic temperature, T_0 of the laser diode measures the temperature sensitivity of the device. Higher values of T_0 imply that the

threshold current, threshold current density and the external differential quantum efficiency of the device will increase less rapidly with increasing temperatures meaning the device is thermally stable.

To determine the characteristic temperature (T_0), the natural logarithm of threshold current density as a function of temperature and the slope of the linear regression is measured as explained numerically by equations 2-20 and 2-21.

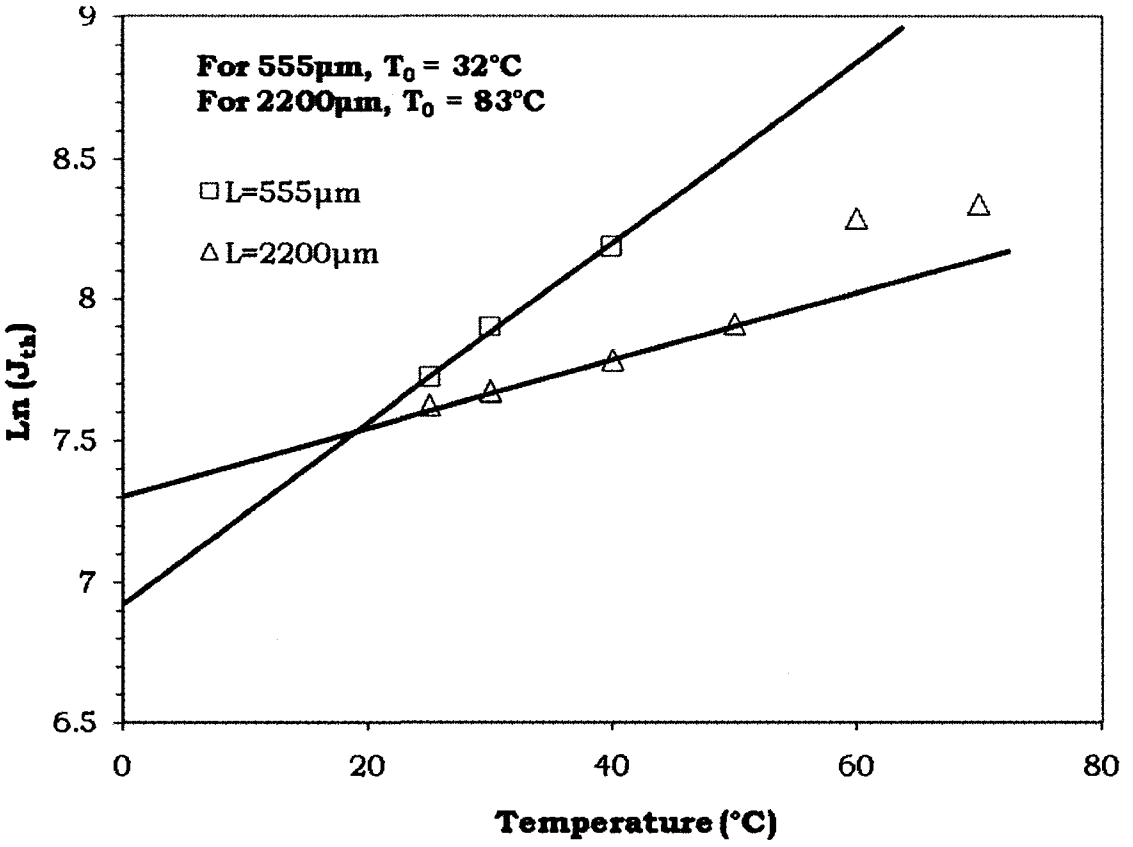

Fig. 4-14 The natural log of threshold current density as a function of temperature for the 2.0 x 555µm and 2.0 x 2200 µm devices.

Fig. 4-14 shows the plot of the natural logarithm of threshold current density versus temperature. The characteristic temperature values for

the 555 μm and 2200 μm are calculated from the plot to be 32°C and 83°C respectively. The higher temperature values are not included in the linear fit because of the high threshold current and degraded output power observed at these high temperatures. A much better characteristic temperature value is obtained for the 2200 μm lasers compared to 555 μm lasers. Higher T_0 indicates reduced threshold current density dependence on temperature thereby exhibiting superior temperature stability of the 2200 μm laser devices. Therefore longer cavity lasers have better temperature stability because of its wider area since the geometry allows better thermal dissipation of heat compared to shorter cavity lasers.

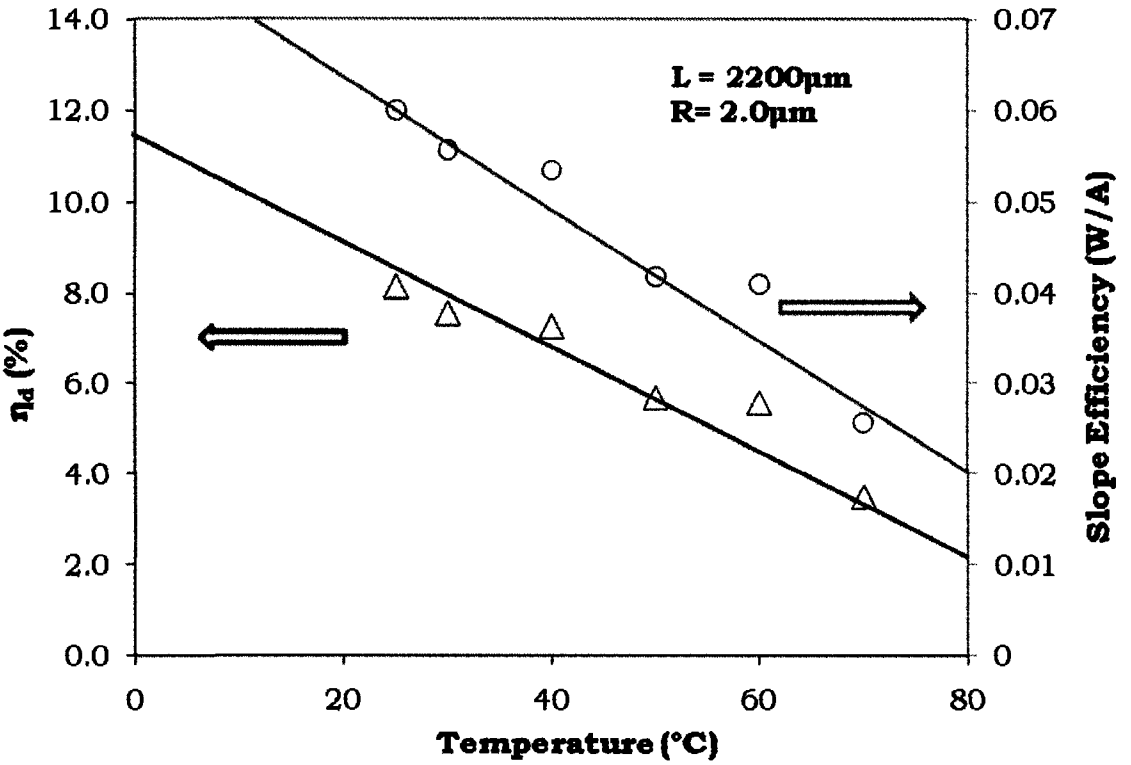

Fig. 4-15 The external quantum efficiency and slope efficiency as a function of temperature for the 2.0 x 2200 μm device

Fig. 4-15 shows the relationship between the slope efficiency and the external quantum efficiency, η_d, with temperature for the 2.0 x 2200 μm laser devices. The increasing temperature decreased the efficiency of the laser devices. The slope efficiency decreased from 0.06 at 25°C to 0.026 at 70°C, the external quantum efficiency decreased from 8.2% at 25°C to 3.5% at 70°C. This degradation of efficiencies was also observed for the 555 μm laser devices.

4.4 Optical Characteristics

The optical spectrum analyzer (OSA) has a dynamic range between 600 nm to 1700 nm wavelength. The dynamic range however limits some of the spectral analysis. The spectra was taken over a 100 nm (or less) span with a high sensitivity and resolution. The 1270 and 1524 μm devices were used for the spectra measurements.

4.4.1 Gain and Loss

The carrier distribution in the active layer strongly depends on the injection current below threshold. The below-threshold spectra are useful because the broad spectrum of spontaneous emission clearly shows the FP-modes of the cavity better than narrow-linewidth stimulated emission as well as lower carrier heating effects. At currents higher than threshold current, stimulated emission predominantly occurs and below threshold it is predominantly spontaneous emission[29].

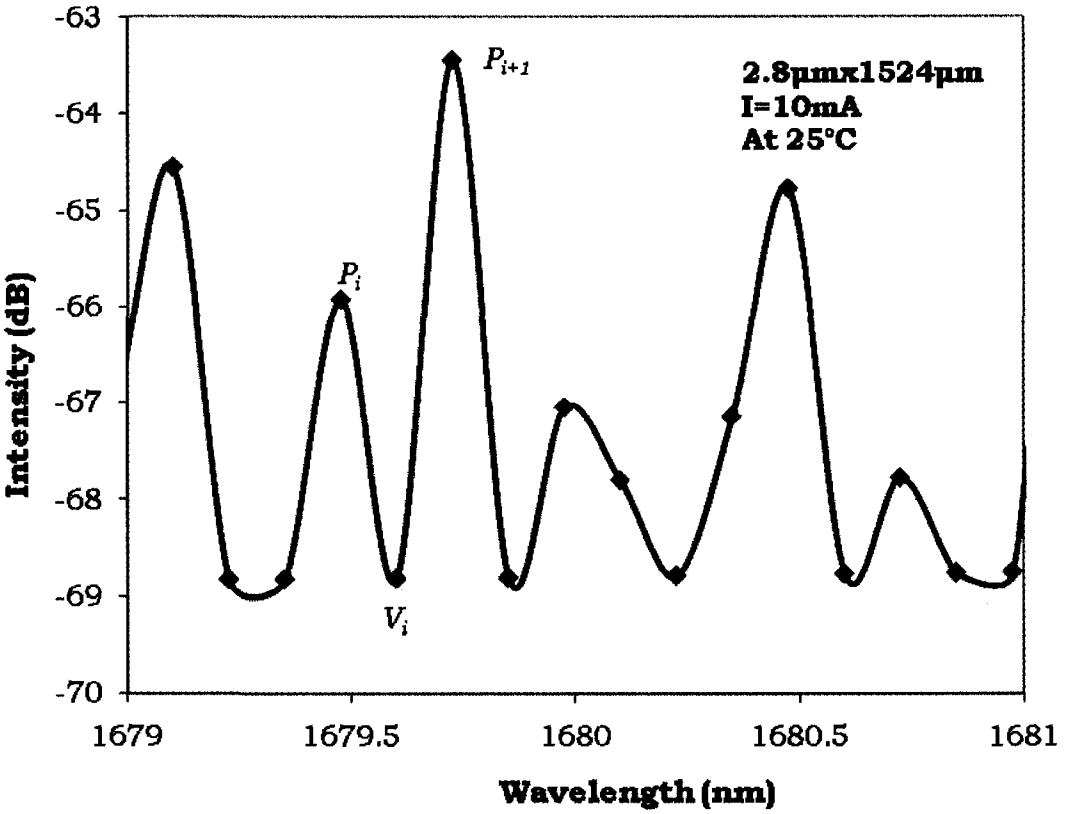

Fig. 4-16 The Fabry-Perot resonance of the spontaneous emission from 2.8 x 1524 μm laser device taken by a high resolution OSA at 25°C. The laser was biased at 10 mA

Fig. 4-16 displays the spontaneous emission spectrum below threshold biased at 10 mA and zoomed in to show the F-P resonance mode. The gain spectra are obtained by measuring the depth of modulation caused by the Fabry-Perot resonance in the emission spectrum.

The intensity peaks (maximum) and valleys (minimums) are determined in order to calculate the gain and loss. To increase the accuracy of gain extraction, algorithms such as the mode sum minimum method [53] and the nonlinear least-squares fitting method [54] have been introduced. An averaging method that computed the intensity contrast,

$r(\lambda)$, at any wavelength is used by first averaging the intensities of adjacent peak, $\frac{1}{2}(P_i + P_{i+1})$, and then dividing by the intensity of the intermediate valley, V_i [55] :

$$r_i = \frac{P_i + P_{i+1}}{2V_i} \qquad 4\text{-}1$$

The 2.8 × 1524 μm devices were selected for the gain spectra measurements. As shown in Fig. 4-16 the mode spacing $\Delta\lambda$ is 0.25 nm. At the lasing wavelength of 1686nm, the calculated effective index n_{eff} is 3.73 and the mirror reflectivity calculated using Fresnel's equation is 0.333 for the 1524 μm devices. The intensity contrast is determined to be 0.938. For the 1524 μm device the internal loss, α_i is about 19 cm^{-1}. The mirror loss is given by equation ($\alpha_m = \frac{1}{2L}\ln\frac{1}{R_1R_2}$) and it is calculated for the cavity length L = 1524 μm and R = 0.33 as α_m = 7.2 cm^{-1}. The optical loss is a sum of the cavity (internal) loss and the mirror loss. Therefore the optical loss is 26.2 cm^{-1}.

The modal gain measured is given by the equation $(G = g_{th}\Gamma - \alpha_i + \alpha_m)$. Using the confinement factor $\Gamma = 0.043$ calculated in LAS2D software, the net material gain is extracted to be about 609.3 cm^{-1}.

Fig. 4-17 is the modal gain spectra as a function of wavelength measured at 25°C.

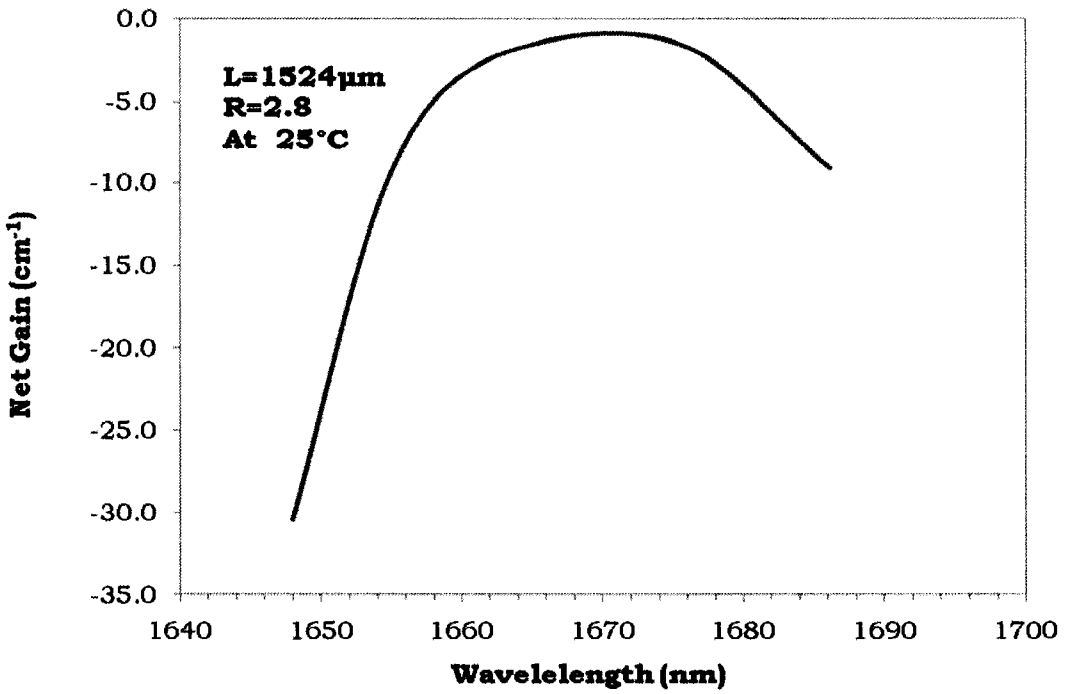

Fig. 4-17 The gain spectra measured at 25°C for 2.8 x 1524 µm laser device.

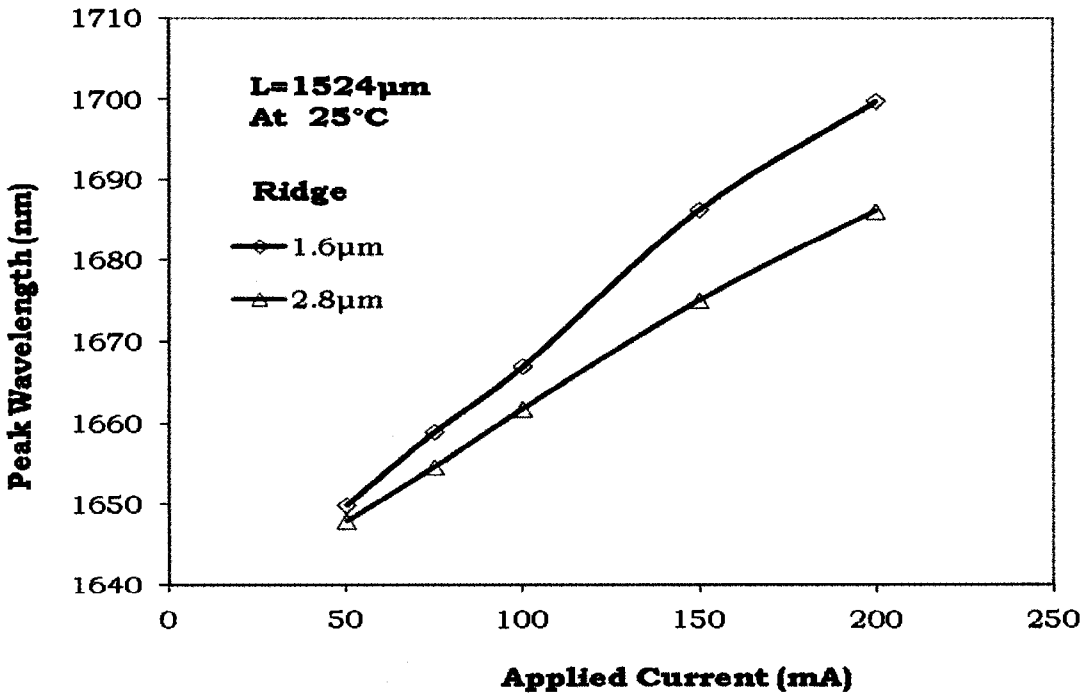

Fig. 4-18 The peak wavelength as a function of the biased current of the 1.6 x 1524 µm and 2.8 x 1524 µm laser devices at 25°C.

Fig. 4-18 shows the peak wavelengths of the 1.6 x 1534 μm and 2.8 x 1524 μm laser devices at different bias currents. As observed 1.6 μm ridge width devices is shifting more in wavelength than the 2.8 μm ridge widths devices because of the higher (anomalous) threshold current it exhibited in Fig. 4-7

4.4.2 Spectral Properties

Fig. 4-18 shows the near-threshold spectra for a 2.8 x 1270 μm device measured at 25°C. The spectra indicate transverse mode emission at the wavelength of 1650 nm.

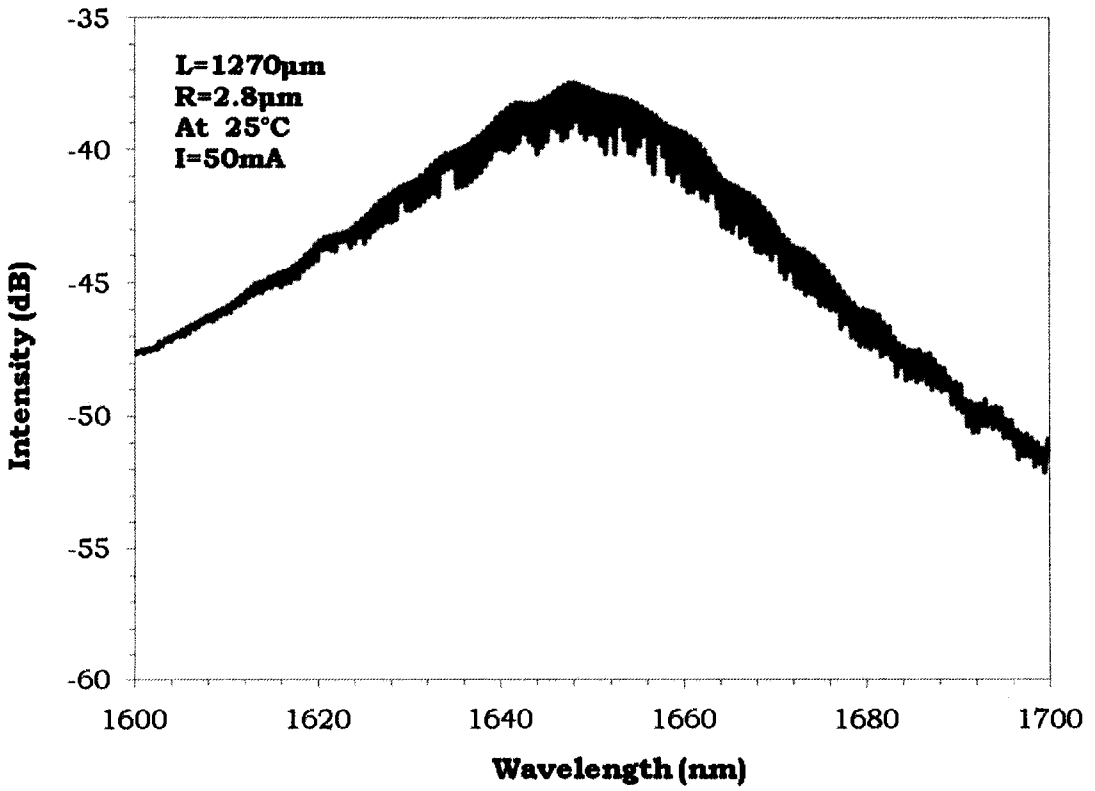

Fig. 4-19 The sub-threshold spontaneous emission spectrum of the laser.

Single mode lasers exhibit a phenomenon called mode hopping in which the peak wavelength of the laser diode hops over discrete wavelength bands and does not show continuous tuning over a broad range[56]. This hopping occurs with bias current changes, increasing the bias current cause red-shift in the centre wavelength which is as a result of the shift in gain spectra caused by reduction in the band gap. Fig. 4-20 and Fig. 4-21 show the emission spectra as bias current increases. It demonstrates that the laser is excited by transverse mode and weak mode-hopping to the long-wavelength side is observed due to increasing bias current. Broadening of the spectrum is observed as more current is injected due to thermal effect and as the energy levels are filled up (density of states)

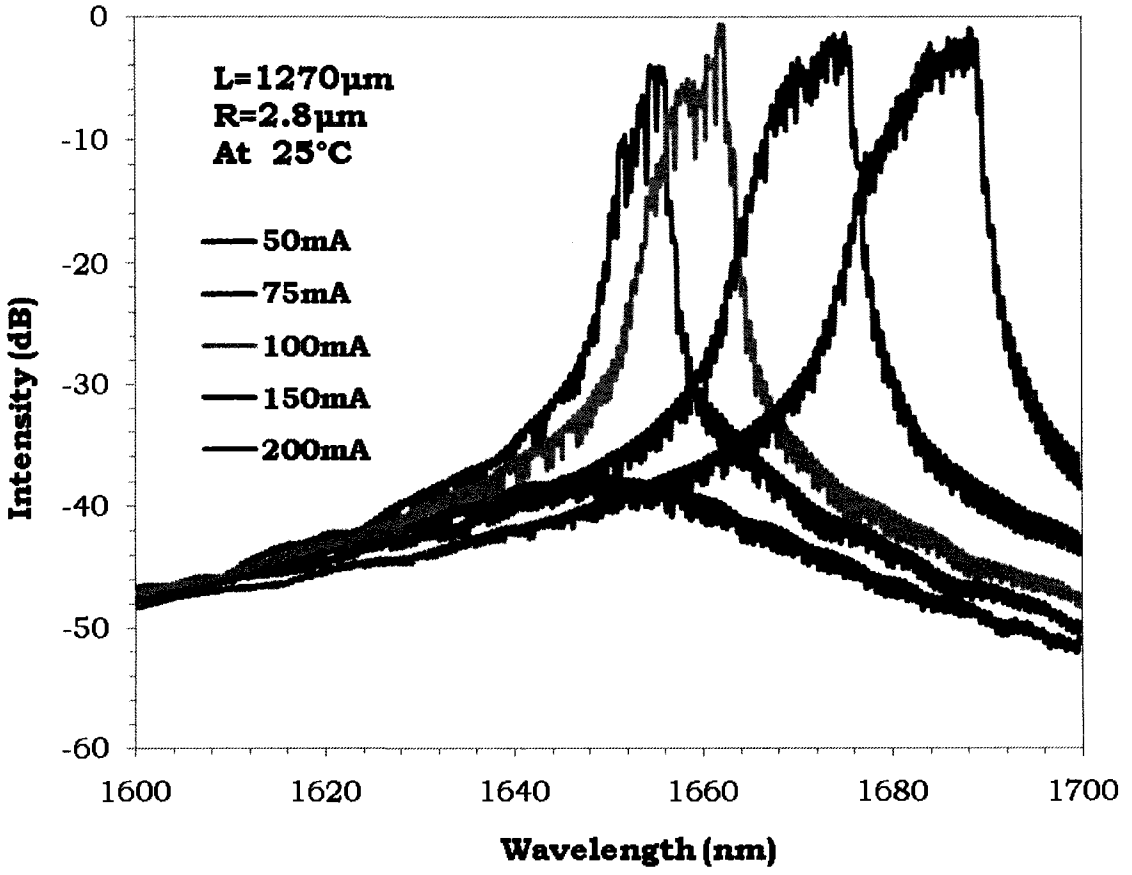

Fig. 4-20 The emission spectra from a 2.8 x 1270 μm laser device at 50 to 200 mA.

Fig. 4-20 shows the increase of emission wavelength from 1648 nm at 50 mA to 1686 nm at 200 mA. Fig. 4-21 shows the increase of emission wavelength from 1650 nm at 50 mA to > 1700 nm at 200 mA.

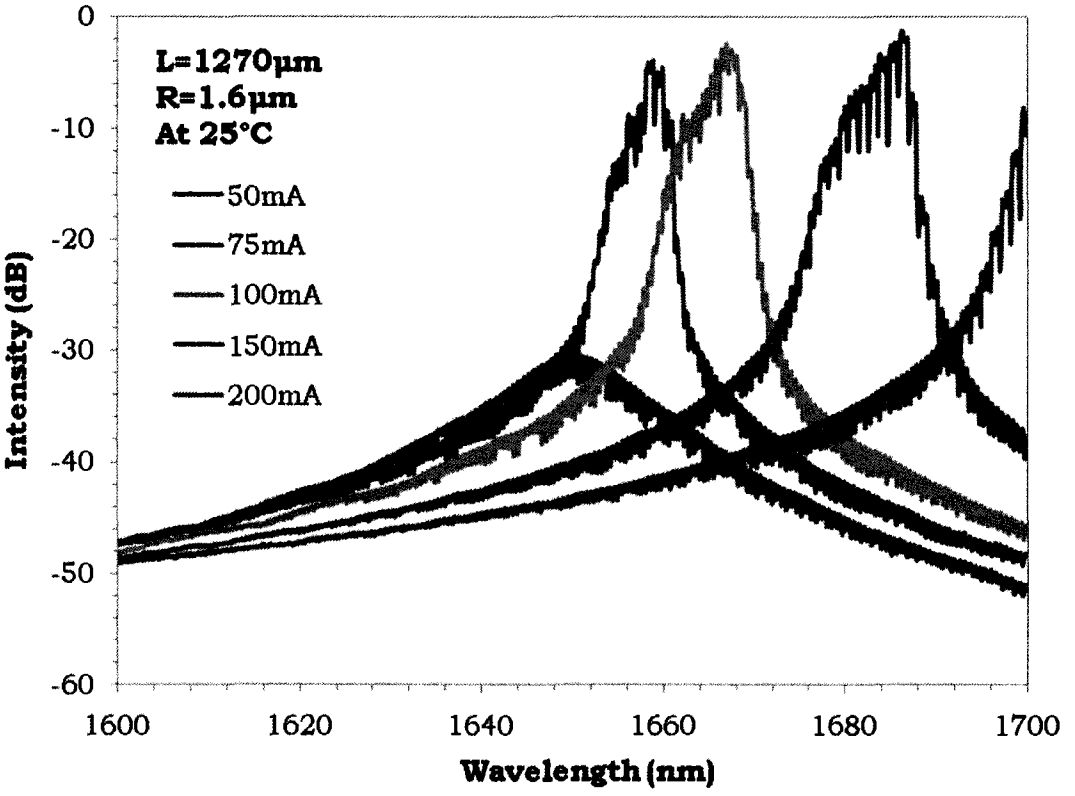

Fig. 4-21 The emission spectra from a 1.6 x 1270 μm laser device at 50 to 200 mA.

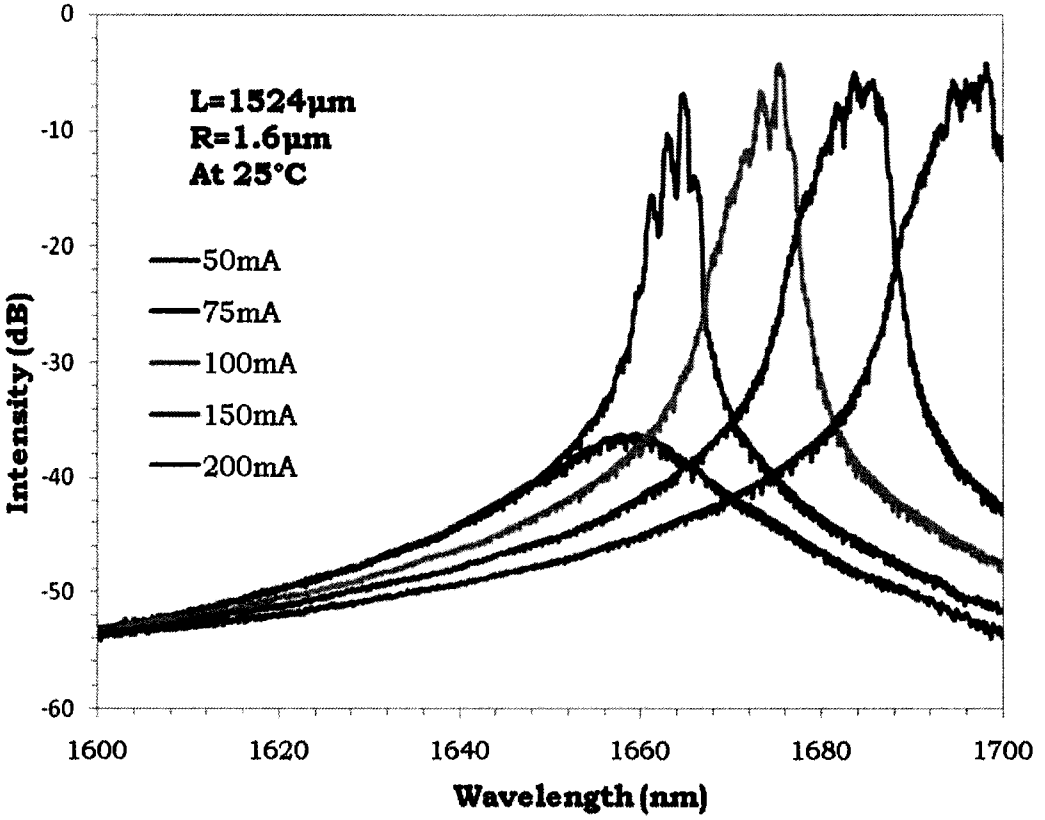

Fig. 4-22 The emission spectra from a 1.6 x 1574μm laser device at 50 to 200 mA.

Fig. 4-22 also shows strong red-shift of the emission wavelength with increasing bias currents.

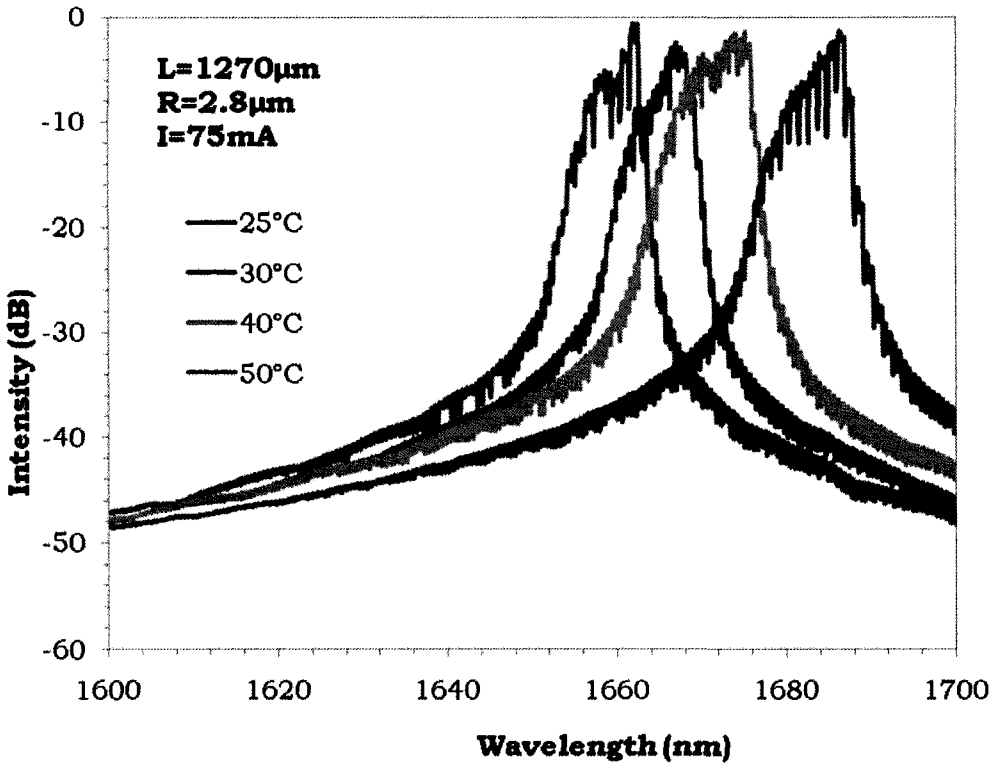

Fig. 4-23 The spectra of a 2.8 x 1270 µm device at $1.5xI_{th}$ measured from 25 to 50°C.

The temperature dependent spectroscopy (Fig. 4-23) was performed on the same device. During the measurement, the bias current was adjusted to 150% of the threshold current (75 mA) for each temperature measurements. The peak wavelength of a laser diode is directly proportional to its operating temperature. There is a linear relationship between temperature and peak wavelength. The temperature dependent spectroscopy in Fig. 4-23 shows this laser wavelength increase with emission temperature from 1658 nm at 25°C to 1686 nm at 50°C. This is due to gain shift which is as a result of bandgap reduction and weak mode hopping due to optical/index variation with temperature.

4.5 Conclusions

This chapter studied the properties of InAlGaAs/InP through L-I and spectral measurements. The material and the geometrical parameters of the InAlGaAs MQW lasers were extracted and analyzed and the the dependence of these parameters on the various cavity lengths and ridge widths of the laser is understood.

The lasers L-I characteristics shows a linear increase in threshold current with the cavity length. This agrees with theory because longer cavity length lasers require longer time for facet-to-facet reflection, and thus require higher injection current for gain to equal the losses. The threshold current increases almost linearly with the ridge width, excluding the 1.2 μm and 1.6 μm ridge widths which had high threshold currents. Thermal power roll-off also occurs at higher injection currents because of the heating of the laser device.

The slope and quantum efficiencies increase within the same cavity length for different ridge widths but decreases with increase in cavity length. Narrow ridge devices tend to have higher internal absorption due to higher carrier densities.

The laser devices were exposed to varying temperatures and the dependence of threshold current and efficiencies with temperature are calculated. The high temperature characteristics of InAlGaAs MQW lasers are evaluated. The temperature-dependent L-I measurement to a 2.0 x 2200 μm devices exhibits the characteristic temperature T_0 of 83°C and the 2.0 x 555 μm devices exhibits the characteristic temperature T_0

of 32°C. The high T_0 of 2.0 x 2200 μm devices indicates that these lasers are less sensitive to the temperature change.

The characteristic temperature T_0 of longer cavity length InAlGaAs lasers with larger ridge widths is higher than their shorter cavity counterparts due to the longer cavity allowing more area for thermal dissipation. This accounts for their better temperature stability characteristic. As the temperature increases, the threshold current of the laser increases. Maximum power degradation and thermal roll-off occurs at higher temperatures. There was a continual decrease in the slope efficiency and the external quantum efficiency as the temperature increased showing general degradation of laser devices at high temperatures.

Optical loss and gain properties of the InAlGaAs lasers were studied using the high resolution spectral measurements. The spectral properties of the laser devices demonstrate laser excitation by a transverse mode. Weak mode-hopping of the peak wavelength to the long-wavelength is observed, the red shift of emission wavelength is due to gain shift which occurs because of band gap reduction with increasing carrier injection, the emission wavelength changes from 1648 to 1670 nm. The temperature dependent spectroscopy also showed shifting of the emission wavelength to longer wavelengths from 1658 nm at 25°C to 1686 nm at 50°C for 75mA biased current, weak mode-hopping to the long-wavelength is observed due optical/index variation with temperature. The analysis shows that the InAlGaAs laser emission occurs between 1648 and 1700 nm wavelength. The dynamic range of the OSA limits the knowledge on how far into the long wavelength the InAlGaAs will emit, since the red-shifting is directly proportional to the biased current, it should be noted that high biased current might

degrade the laser devices through heating in which case will defeat the aim.

Chapter 5 Modeling and Simulation of InAlGaAs Lasers

5.1 Introduction

In this chapter the considerations in laser material modelling to better performance analysis and design are presented, such as the various material modelling parameters that include carrier dynamics, recombination, gain and temperature models. These different models and more are implemented in several available commercial simulation tools such as the the LAS2D simulator[57]. The chapter also describes the implementation of the InAlGaAs laser design in the Las2D simulator. The LAS2D simulator uses a two dimensional laser simulation methodology and method of analysis. The result of the analysis is presented to include its band structure, carrier consumption, carrier density, optical mode and optical gain. Sections 5.3 – 5.8 which discuss the different material models are taken from reference[15] and modified to fit this thesis.

5.2 LAS2D Simulator

Las2D is a two-dimensional non-isothermal laser simulation tool developed by the researchers in the Optoelectronics Laboratory, Ecole Polytechnique, Montreal, Canada. The capabilities of LAS2D include thermal effects, strain and multimode oscillation for a selection of widely used materials. It can calculate strained layer quantum well lasers made on InP with arbitrary alloy compositions. Las2D solves the Poisson

equation and the continuity equations for the electrons and the holes, in a non-isothermal and two-dimensional context, for bulk and multiple-quantum-well (MQW) devices[57]. There has been regular model and functionality upgrade to meet latest laser requirements.

The self-consistent calculation is based on classical models of carrier transport, optical gain, mode profile and heat flux. Three material systems are contained in LAS2D, these are InGaAsP/InP, InGaAlAs/InP and AlGaAs/GaAs. The InGaAsP and InAlGaAs material systems can be mixed within the same device because both assume an InP substrate. LAS2D has simple, tested physical models and the interface is user friendly.

One definition input file is required to describe the device structure in terms of the global, ionization, mobility, layer, quantum well and other parameters, the device can easily be modified to any structural change. The simulation can be run on Microsoft windows through Las2dManager or from a DOS-prompt. The 'viewsim' post-processing graphical user interface (GUI) is quite broad with many graphical options.

5.3 Parameter Models

A list of the basic physical parameters for III-V binary compounds is presented in Table 5-1. Several other ternary and quaternary alloy parameters are obtained by linear interpolation between the parameters of the relevant binary materials.

Table 5-1 Material parameters for some III-V binary compounds[15].

	Unit	InAs	GaAs	AlAs	InP	GaP	AlP
E_g^Γ	eV	0.354	1.414	3.099	1.424	2.886	3.63
α^Γ	meV/K	0.276	0.541	0.885	0.363	----	0.577
β^Γ	K	93	204	530	162	----	372
Δ_{so}	eV	0.39	0.341	0.28	0.108	0.08	0.07
m_c^*	m_0	0.023	0.067	0.15	0.08	0.13	0.22
E_p	eV	21.5	28.8	21.1	20.7	31.4	17.7
F	-----	-2.9	-1.94	-0.48	-1.31	-2.04	-0.65
γ_1	-----	20	6.98	3.76	5.08	4.05	3.35
γ_2	-----	8.5	2.06	0.82	1.6	0.49	0.71
γ_3	-----	9.2	2.93	1.42	2.10	2.93	1.23
a_c	eV	-5.08	-7.17	-5.64	-6.0	-8.2	-5.7
a_v	eV	1.0	1.16	-2.47	-0.6	-1.7	-3.0
b	eV	-1.8	-2.0	-2.3	-2.0	-1.6	-1.5
c_{11}	GPa	832.9	1221	1250	1011	1405	1330
c_{12}	GPa	452.6	566	534	561	620.3	630
σ_T	cmK/W	3.7	2.27	1.1	1.47	1.3	0.77
ε	-----	14.6	13.1	10.06	12.56	11.1	9.8
a_0	$\mathring{A}$	6.058	5.653	5.661	5.870	5.451	5.467

where;

m_c is the electron mass

γ_1 and γ_2 are Luttinger parameters.

F is the matrix element count for the higher band contributions to the conduction band

E_p is the matrix element count for the interaction between s-like conduction bands and p-like valence bands

Δ_{so} is the quantity for the interaction of electron spin and spin-orbit

5.4 Carrier Dynamics

The flow of electrons and holes is the current in semiconductor devices and described by the drift-diffusion model. The drift current is generated by an electric field, $\vec{E}$. The magnitude is proportional to the electron and hole conductivities that are related to the carrier concentration in materials as $\sigma_n = q\mu_n n$ and $\sigma_p = q\mu_p p$, where μ_n and μ_p are the electron and hole mobility, q is the charge, n and p represent the concentration of electrons and holes.

The concentration gradient of electrons and holes drive the diffusion current and the magnitude is proportional to the diffusion coefficient D_n and D_p. In a uniform semiconductor, the total current density of electrons and holes is:

$$\vec{j}_n = q\mu_n n\vec{E} + qD_n\nabla n \quad \text{and} \quad \vec{j}_p = q\mu_p n\vec{E} + qD_p\nabla p \qquad 5\text{-}1$$

The current densities are controlled by the charge continuity equation and their changes are driven by the spatial change in current flow and by the electron-hole pairs generated or recombined in the spatial space and time. The expressions are:

$$q\frac{\partial n}{\partial t} = \nabla \cdot \vec{j}_n - q(R-G) \qquad 5\text{-}2$$

$$q\frac{\partial p}{\partial t} = -\nabla \cdot \vec{j}_p - q(R-G) \qquad 5\text{-}3$$

where G and R are the carrier generation and recombination rates.

The electric field $\vec{E}$ is affected by the charge distribution, which includes the mobile carriers, fixed charges of dopant ions, N_D^+ and N_A^-, (D for donor, A for acceptor) and the deep trap level of type j. The steady-state Poisson equation makes the connection:

$$\vec{\nabla}(\varepsilon\vec{E}) = q\left(p - n + N_D^+ - N_A^- + \sum_j N_{trap}(f_{Tj})\right) \qquad 5\text{-}4$$

In LAS2D the above three equations are solved self-consistently with material and structural properties as inputs and the carrier transport behaviour can be determined[15].

5.5 Carrier Mobility Model

Electron and hole mobility, μ_n and μ_p, are important parameters for carrier transport computation. Studies of mobility have been carried out experimentally and theoretically and empirical mobility models have been developed by combining these theories with experimental observation on mobility measured by the Hall Effect. An accurate model suitable for III-V materials is the low-field Caughey-Thomas-like mobility model [58]. In this model, carrier mobility is a function of temperature and doping in the form:

$$\mu(N,T)=\mu_{\min}+\frac{\mu_{\max}(300K)(300/T)^{\theta_1}-\mu_{\min}}{1+\left(\frac{N}{N_{ref}(300K)(T/300)^{\theta_2}}\right)^{\lambda}} \qquad 5\text{-}5$$

Where N is the carrier concentration and T is temperature. Their influence on mobility is evaluated by the factors of λ and θ_1, θ_2. $\mu_{\max}$ is the maximum mobility that is usually measured in un-doped materials. "The six parameters are best fitted for the specified III-V compounds to the available Hall measurement data in a large range of carrier concentration and temperature using least-squares method"[15]. Reference[59] lists the parameters for the common III-V binary and ternary materials.

5.6 Recombination Model

Electron-hole recombinations as explained in chapter 2 are physical mechanisms that are either radiative recombinations (spontaneous and stimulated) or non-radiative recombinations (mainly from Auger and Shockley-Read-Hall recombination). The sum of all these recombination rates make up the total recombination rate.

The spontaneous recombination rate is given by:

$$R_{spon}=B(np-n_0p_0) \qquad 5\text{-}6$$

where B is the material coefficient, and $np - n_0 p_0$ is the excess carrier concentration which vanishes in thermal equilibrium.

Stimulated emission is also a radiative event that occurs as a result of the optical field. The recombination rate is related to the intensity of the optical field by:

$$R_{stim} = v_g g(n,p) \cdot S \cdot I(x,y) \qquad 5\text{-}7$$

where v_g is the group velocity, $g(n,p)$ is the material gain, S is the photon density, and $I(x,y)$ is the optical field.

The excess energy in Auger recombination is transferred to another electron within either the valence band or conduction band, relating to c_p and c_n, respectively. Three particles are involved in an Auger event therefore Auger recombination rate is determined by the third-order polynomial fit to the recombination rate measurement and it is a function of carrier concentration[9]:

$$R_{Aug} = (c_n n + c_p p)(np - n_0 p_0) \qquad 5\text{-}8$$

Shockley-Read-Hall (SRH) recombination is the last recombination process usually considered in carrier dynamics. Unlike the other recombination processes, the SRH process is the interaction between electrons and ionized energy levels deep inside the semiconductor band gap. Those energy levels are normally generated by crystal defects (deep traps). It is normally significant only in low quality crystals and in semi-insulating materials. Its rate is proportional to the trap density that is parameterized by carrier life times of τ_n and τ_p. The properties of existing

traps can be very different depending on their local environment. The calculation of the SRH recombination rate can be a very complicated process. However, in good quality crystals where the deep trap density is much less than the doping concentration, SRH recombination rate can be approximated as:

$$R_{SRH} = \frac{np - n_0 p_0}{\tau_p (n + n_1) + \tau_n (p + p_1)} \qquad 5\text{-}9$$

where n_1 and p_1 depend on the intrinsic carrier density and the energy level of the trap acting as a recombination center.

5.7 Gain Model

The gain is proportional to the probability that a given photon triggers an electron transition from a higher energy level j to a low energy level i[14]. Quantum mechanical calculation for the probability has been well established. The simple gain function is derived as [60]:

$$g_{ij}(h\nu) = \left(\frac{q^2 h}{2m_0^2 \varepsilon_0 n_r c}\right)\left(\frac{1}{h\nu}\right)\left|M(E_{ij})\right|^2 D_r(E_{ij})(f_j - f_i) \qquad 5\text{-}10$$

where $M(E_{ij})$ is the transition matrix element. $M(E_{ij})$ determines the transition strength between electron levels in a given material; $D_r(E_{ij})$ is the reduced density of electron states. It is the density of allowed transition between the two bands; $f_j - f_i$ is the Fermi function which gives the probability that the electrons occupy the energy levels of

E_i and E_j. The total optical gain will be the integral of all transitions to heavy and light holes, respectively, within the k-selection rule.

5.8 Temperature Model

Temperature elevation of the material causes band gap shrinkage, therefore many parameters in semiconductors are temperature dependent. The temperature model can be implemented in 2 ways; the complete model with temperature effects included in each parameter or the temperature independent parameter with the generic temperature model added in. Las2D applies the generic temperature model in which the user provides the temperature dependency for the parameters based on two generic temperature models. The first one is a power law model:

$$P_i(T) = P_i(300)\left(\frac{T}{300}\right)^{\alpha} \qquad 5\text{-}11$$

where P_i is a given parameter, $P_i(300)$ is its value at 300K and α is the exponent of the power law. This generic model is suitable for the parameters that exhibit a strong temperature dependency such as the radiative recombination constant, the intra-band relaxation time and the carrier mobility.

The second generic model is an exponential law in the form:

$$P_i(T) = P_i(300)\exp\left(\frac{T-300}{\beta}\right) \qquad 5\text{-}12$$

where β is the critical temperature. For a critical temperature that is not too far from 300K, the exponential law is close to a linear law and is suitable for parameters that show a weak temperature dependency. Examples of the experimental laws are the Auger coefficients and the absorption coefficients[15].

5.9 Simulation Results of InAlGaAs/InP Laser

The laser under simulation is the same device structure as discussed in chapter 1 section 1.4

In summary, the InAlGaAs epitaxial structures were grown on a 3-inch sulphur- (n-)doped InP substrate by digital alloy molecular beam epitaxy. The Fabry-Perot laser MQW active region consists of six 5 nm thick $In_{0.69}Ga_{0.31}As$ quantum wells (1.0% compressive strain) separated by seven 10 nm thick unstrained $In_{0.52}Al_{0.36}Ga_{0.12}As$ barriers. The MQW region has a measured photoluminescence (PL) peak near 1.648 - 1.700 μm. Each laser bar contains several devices of the same cavity length and has cleaved-cleaved facets which mean both facets have same reflectivity of approximately 0.32, the cavity lengths ranges between 600 and 2000 μm. The devices ridge widths are 1.6 and 2.8 μm.

The devices were simulated at various temperatures and bias current of up to 60mA. It was observed that Las2D simulator did not fully solve for higher bias currents specified, this is a glitch that was not yet resolved as at the end of the thesis. However this does not affect the overall results of the simulation since we are mostly interested on results below, at and after threshold current.

5.9.1 Band Structure

The population inversion phenomenon in which more electrons are present in the conduction band than the valence band gives rise to stimulated emission. To maintain the energy inversion state, current has to be injected into the p-n junction. In Las2d the drift diffusion model is used to calculate the bands and the carrier distribution at different applied electrical field.

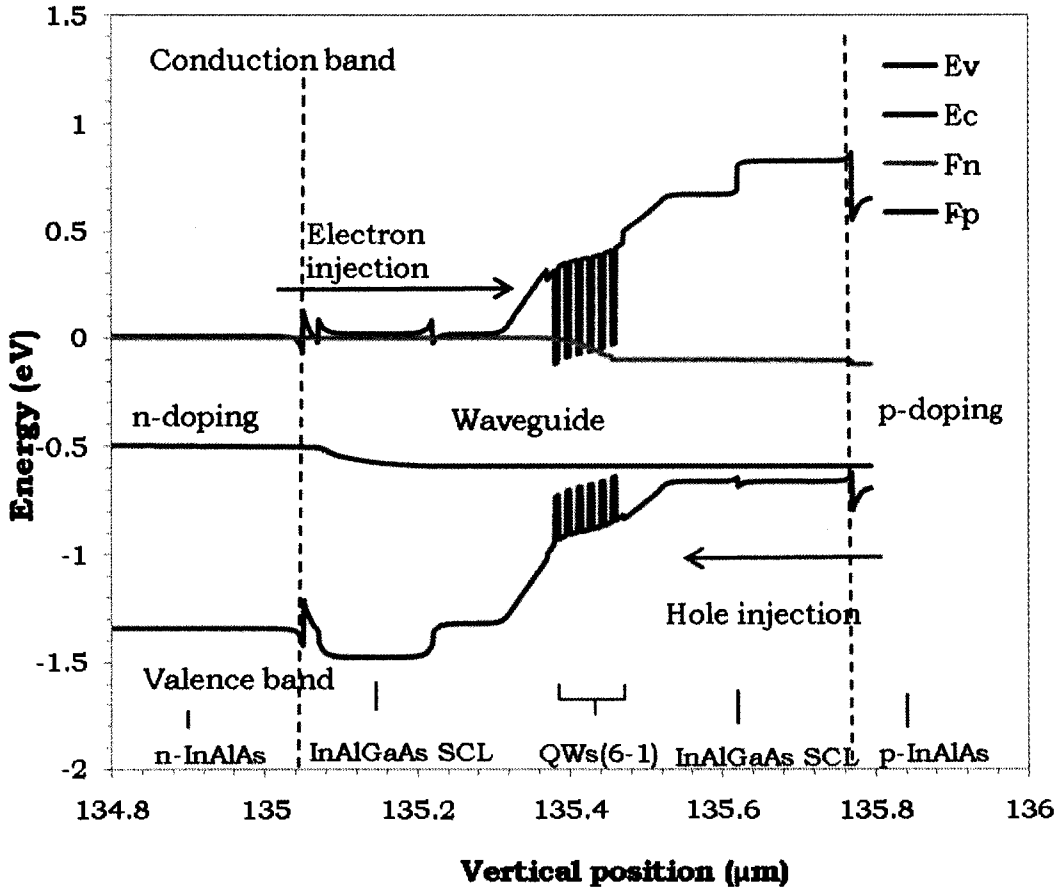

Fig. 5-1 The conduction bands, the valence bands and the Fermi levels at zero bias.

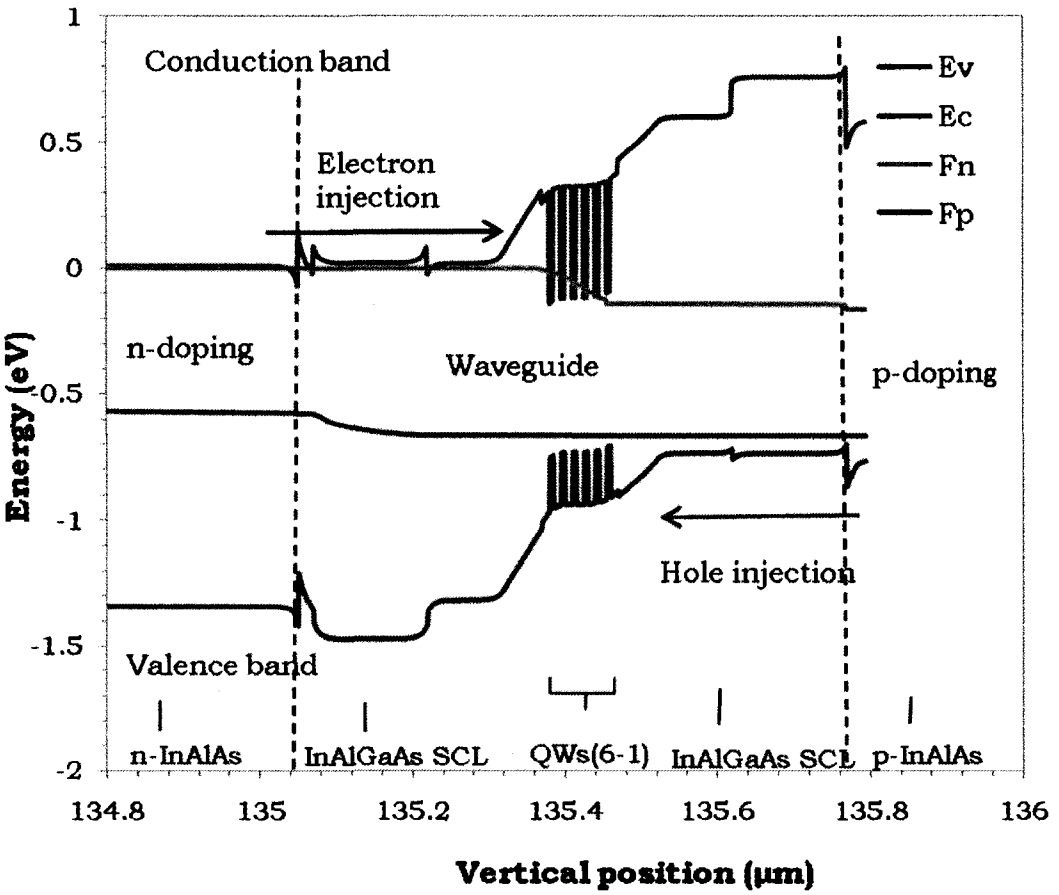

Fig. 5-2 The conduction bands, the valence bands and the Fermi levels at threshold.

where;

Ev is valence band edge (eV)

Ec is conduction band edge (eV)

Fn is electron quasi-Fermi level (eV)

and Fp is hole quasi-Fermi level (eV)

Fig. 5-1, Fig. 5-2, and Fig. 5-3 illustrates the change in conduction and valence bands for the InAlGaAs MQW laser detailed in Table 1-1 from zero bias below threshold to 0.7 V at threshold and finally to 4.22 V after threshold. The figure also indicates the Fermi levels of the electrons and holes.

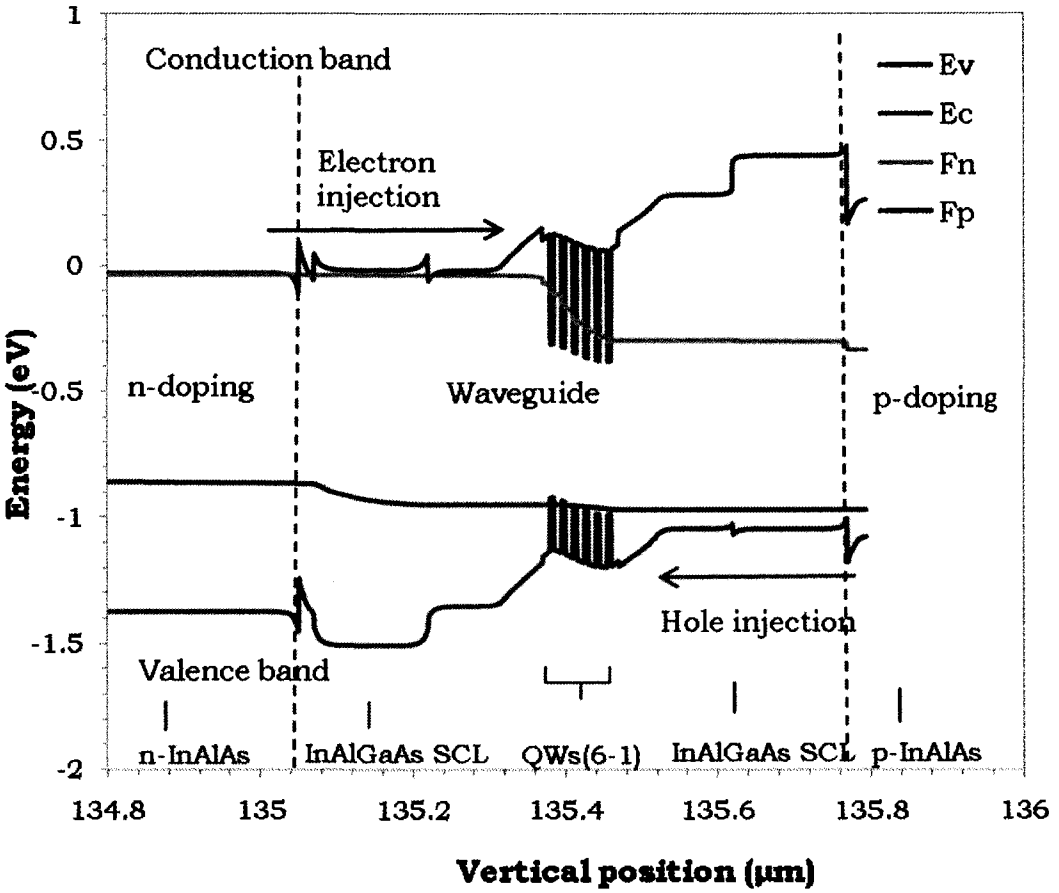

Fig. 5-3 The conduction bands, the valence bands and the Fermi levels after threshold.

When carriers are injected, the laser is considered forward biased, electrons are injected from the n-cladding layer and holes from p-cladding layer, these carriers then drifts and diffuses across the separate confinement layers before being captured by the QWs.

The drift-diffusion model of carrier transport considers Fermi statistics and thermionic emission at hetero-barriers. The offset of the conduction band (ΔEc) and the valence band (ΔEv) controls thermionic emission. For the AlGaInAs material system, a band offset ratio of 0.72 eV is commonly assumed[21]. The energy band diagram in Fig. 5-2

illustrates the large conduction band offset of approximately 0.5ΔEg eV within the MQW. The valence band offset is approximately 0.2ΔEg eV, due to the compressive strain within the quantum wells.

5.9.2 Carrier Density

The threshold carrier density in diode lasers is affected by Shockley-Read-Hall (SRH) recombination, spontaneous emission, Auger recombination, vertical leakage and lateral leakage. Spontaneous emission and lateral leakage consume most of the injection carriers below threshold; SRH and Auger recombination are weak due to the high purity material and the relatively wide band gap hetero-junctions[14]. Stimulated emission dominates the carrier density above threshold.

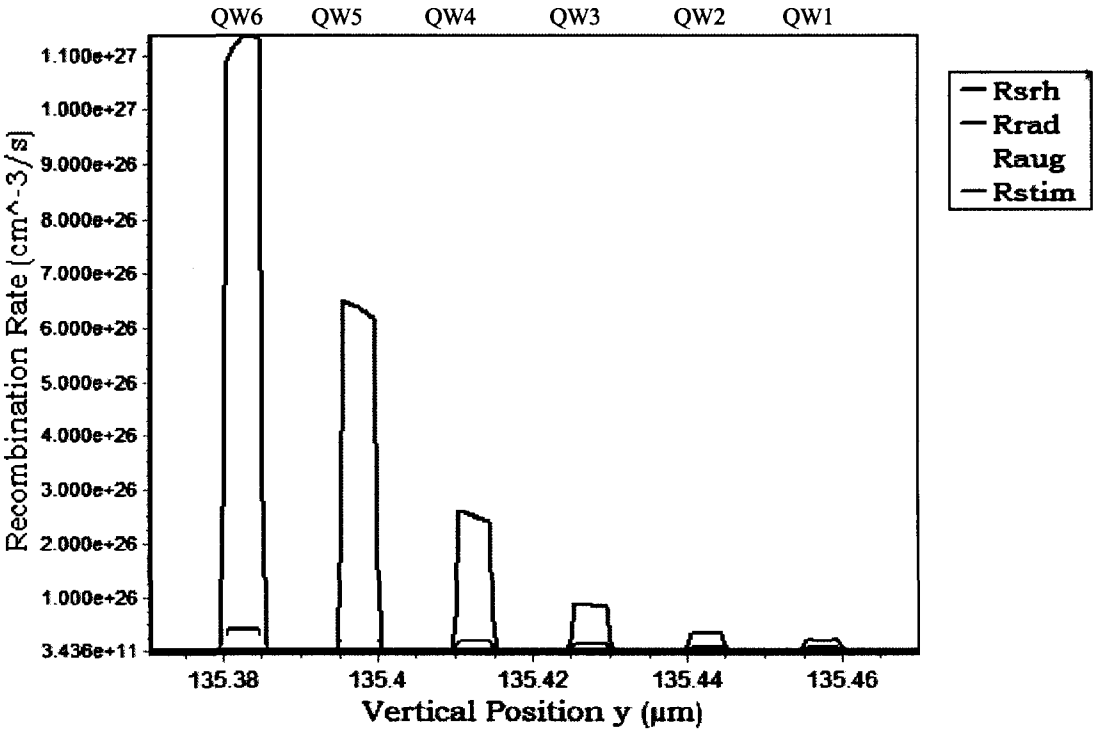

Fig. 5-4 The different recombination rates for the 6 QWs below threshold at 3.567V at room temperature.

where;

Rsrh is the QW Shockley-Read-Hall recombination rate ($cm^{-3}s^{-1}$)

Rrad is the QW spontaneous radiative recombination rate ($cm^{-3}s^{-1}$)

Raug is the QW Auger recombination rate ($cm^{-3}s^{-1}$)

and Rsrh is the QW Stimulated radiative recombination rate ($cm^{-3}s^{-1}$)

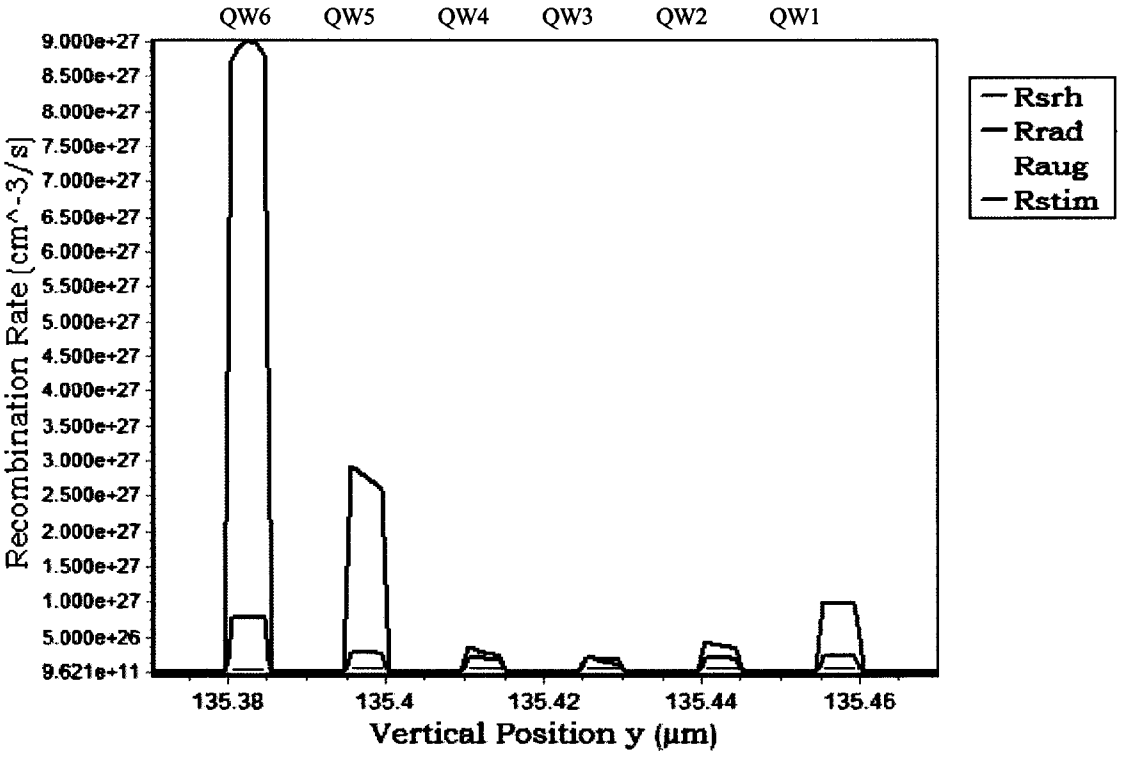

Fig. 5-5 The different recombination rates for the 6 QWs above threshold at 4.216V at room temperature.

As earlier discussed in the theory chapter, radiative or non-radiative recombinations consume injected carrier depending on the band structure, material quality, and operating temperature. Fig. 5-4 shows the carrier consumption mechanism rates in the QW below threshold, here there is no light output because spontaneous emission dominates, the Auger recombination, the SRH recombination are relatively small.

Above threshold as shown in Fig. 5-5 most of the carriers are recombined in the QW in the form of stimulated emission.

Carrier injection, both below and above threshold show non-uniform carrier injection. Below threshold the Rrad is highest at QW6 and deteriorates down to QW1. Above threshold, the largest stimulated recombination rate occurs in QW6, and quite dominant in QWs (5 and 1) but in QWs (2, 3 and 4) the Rstim are comparable with other recombination rates.

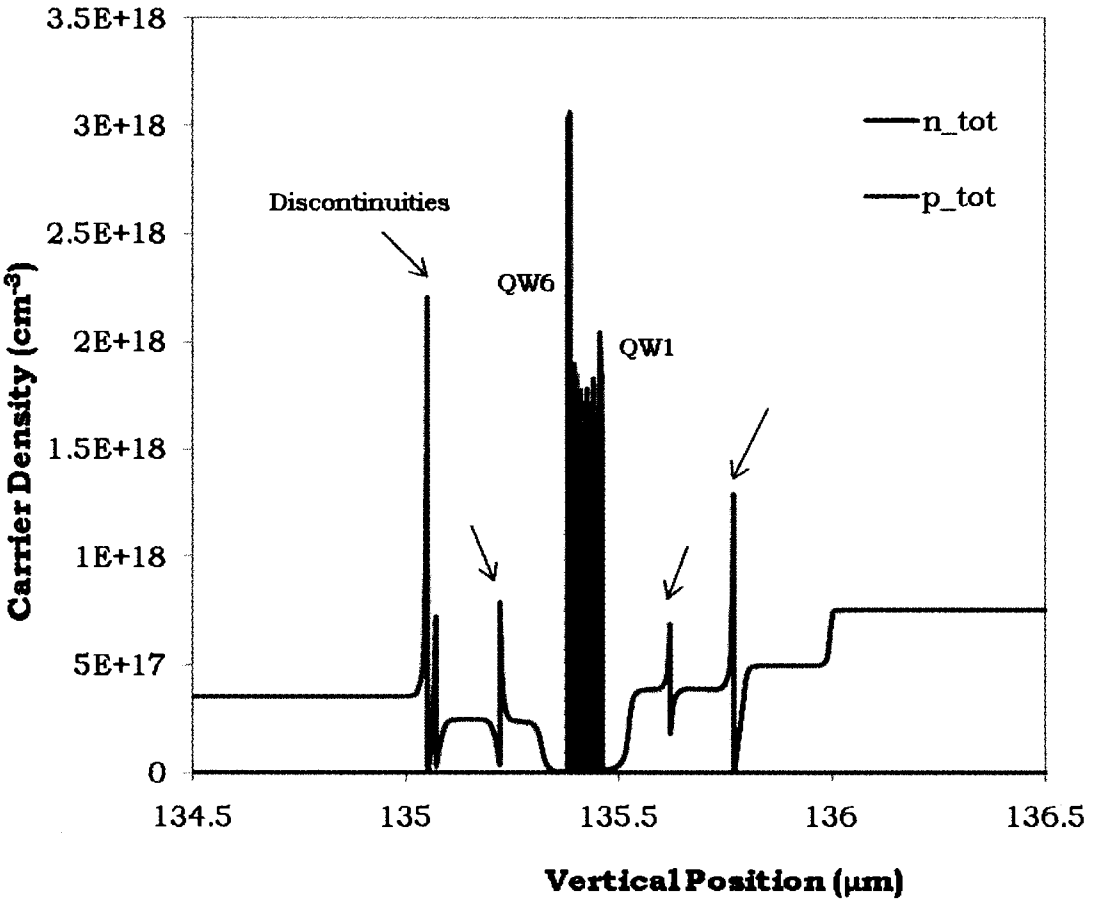

Fig. 5-6 Vertical profile of the electrons and holes carrier density at 60mA.

where;

n_tot is the total electron current density (cm^{-3})

p_tot is the total hole current density (cm^{-3})

Fig. 5-6 shows the sum of the bulk and the confined carrier densities for both the electron and holes in the quantum wells. The carrier density is concentrated in the quantum well region. The InAlAs claddings and InAlGaAs separate confinement layers provide large potential steps to ensure carrier confinement in the QW region.

There is non-uniform carrier distribution across the active region, the carrier density in QW6 is higher than in the other QWs. As reported by Tessler et al, Hangleiter et al and Ban et al, band discontinuities are prominent in InAlGaAs lasers.

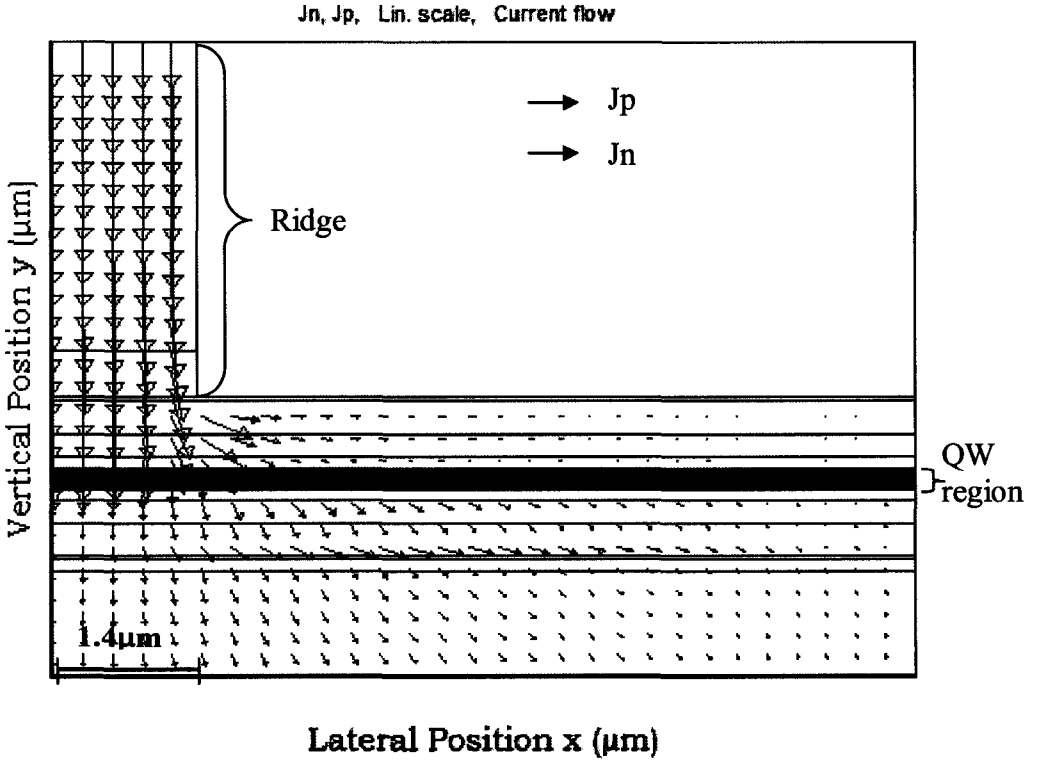

Fig. 5-7 Vector plot of the electrons, holes current density at 300K.

where;

Jn is electron current density (Acm^{-2})

Jp is hole current density (Acm^{-2})

The vector plot of both the electron and hole current densities showing the current flow in the laser device is shown in Fig. 5-7.

5.9.3 Optical Mode

The fundamental optical mode calculated using the effective index approximation is shown in Fig. 5-8. The vertical refractive index profile of the laser device and the normalized optical wave profile are shown in Fig. 5-9.

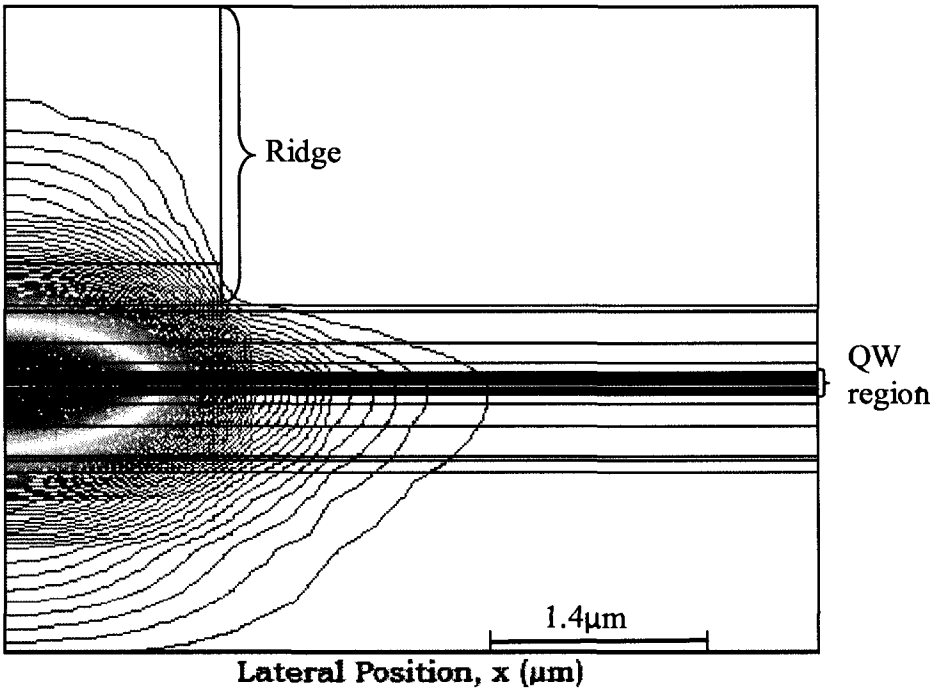

Fig. 5-8 The fundamental optical mode. Highest intensity of the mode is in red, lowest intensity is in blue.

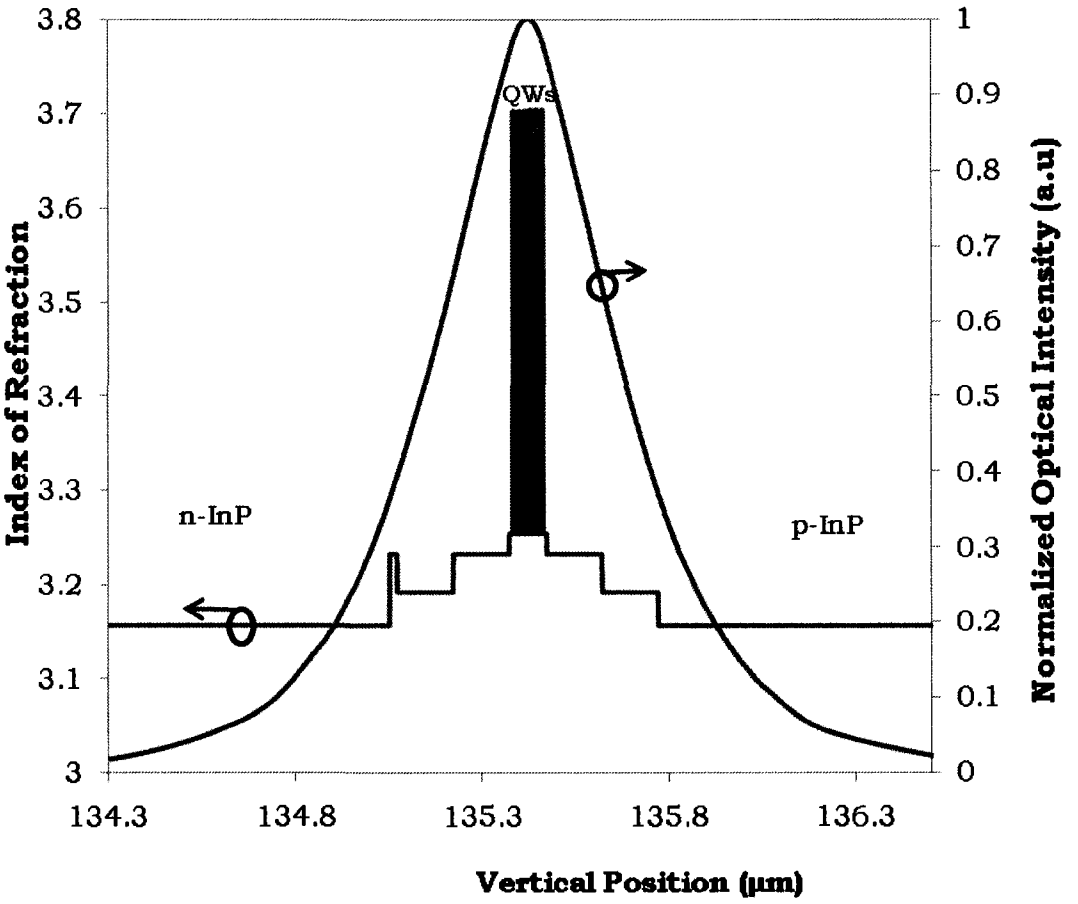

Fig. 5-9 The vertical profile of the calculated refractive index and optical intensity in laser active region.

The refractive index profile near the active region at the biasing carrier density determines the optical confinement factor which is the ratio of the optical volume in the active layer to the volume of the total optical mode in the QWs, the confinement factor is determined to be 0.043.

5.9.4 Optical Gain and Loss

Las2D's simulation uses a self-consistent carrier drift-diffusion model and an optical model to show the peak of the emission spectrum. The

mirror loss α_m and the internal loss α_i quantify the amount of absorption. The mirror loss is dependent of the cavity length and facet reflectivity but the internal loss is dependent on the carrier density, optical field intensity and cavity defects.

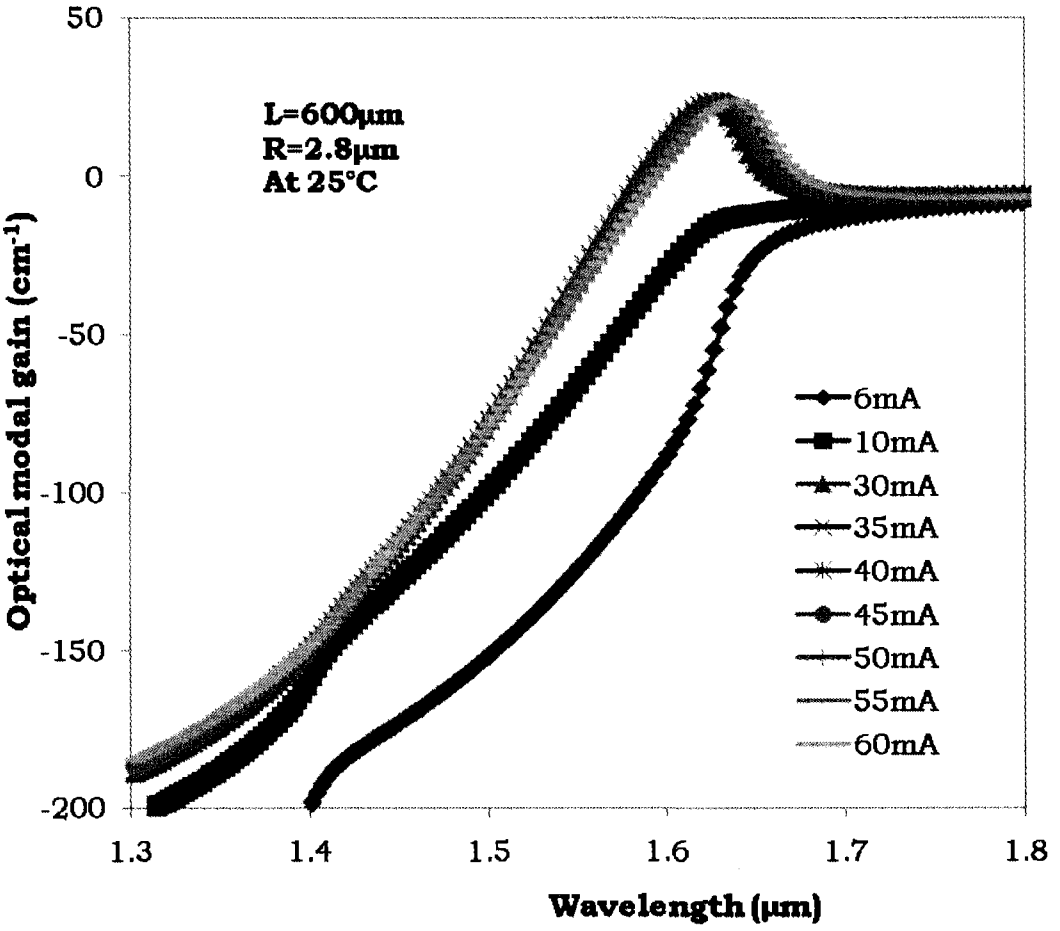

Fig. 5-10 Modal gain spectra at 25°C calculated by Las2D. Gain saturation is clearly observed above the threshold current.

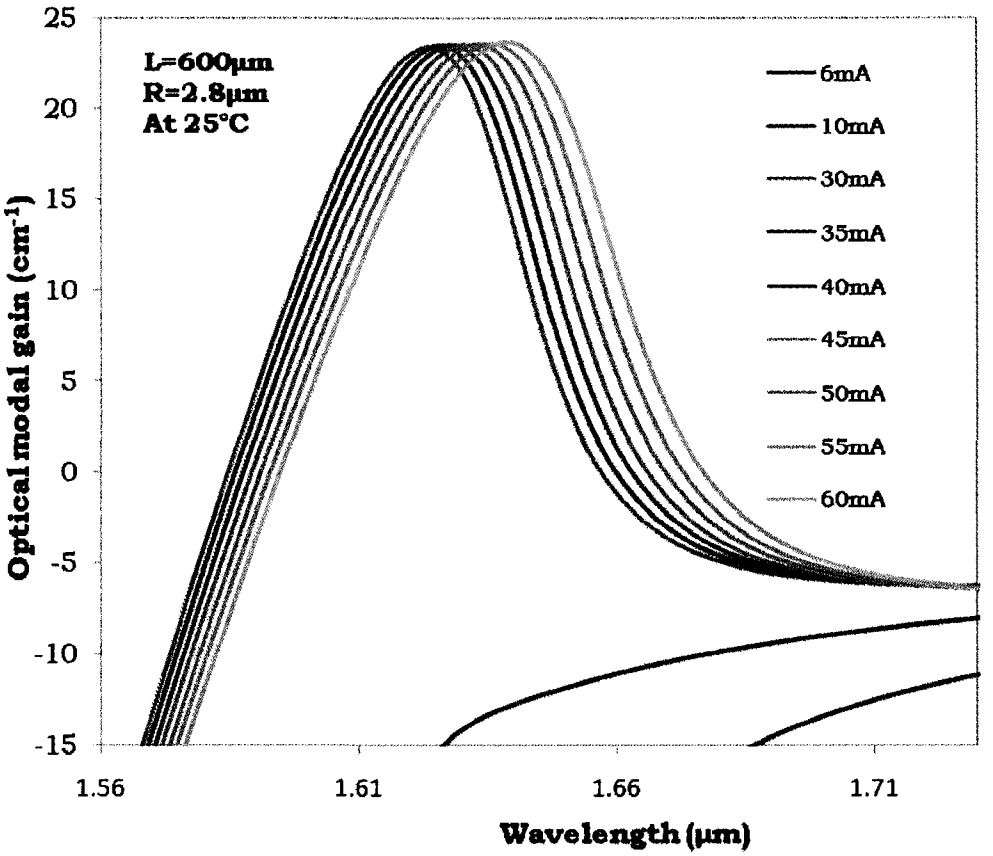

Fig. 5-11 The modal gain spectra zoomed in to clearly show the red-shift.

The red-shift of the emission wavelength is observed as bias current increases, this gain shift is as a result of increasing bias current, when the bias current is increased it means more carriers are injected to fill out the energy level, this reducesza the band gap slightly. Fig. 5-10 and Fig. 5-11 shows the gain spectra of the InAlGaAs laser at different bias currents. The gain peak immediately above threshold (30 mA) is at 1648 nm, at 50 mA the emission wavelength peaks at 1650 nm, this red-shift of the emission wavelength agrees with the experimental results shown in Fig. 4-20, Fig. 4-21, and Fig. 4-22. It is therefore assumed that if the 200mA bias current were to be reached, the wavelength would reach the 1686 – 1700 nm range obtained in the experimental results. Below

threshold (6 mA and 10 mA bias) the gain is less than 0 cm^{-1}, and after threshold, the gain peaks at approximately 23 cm^{-1}.

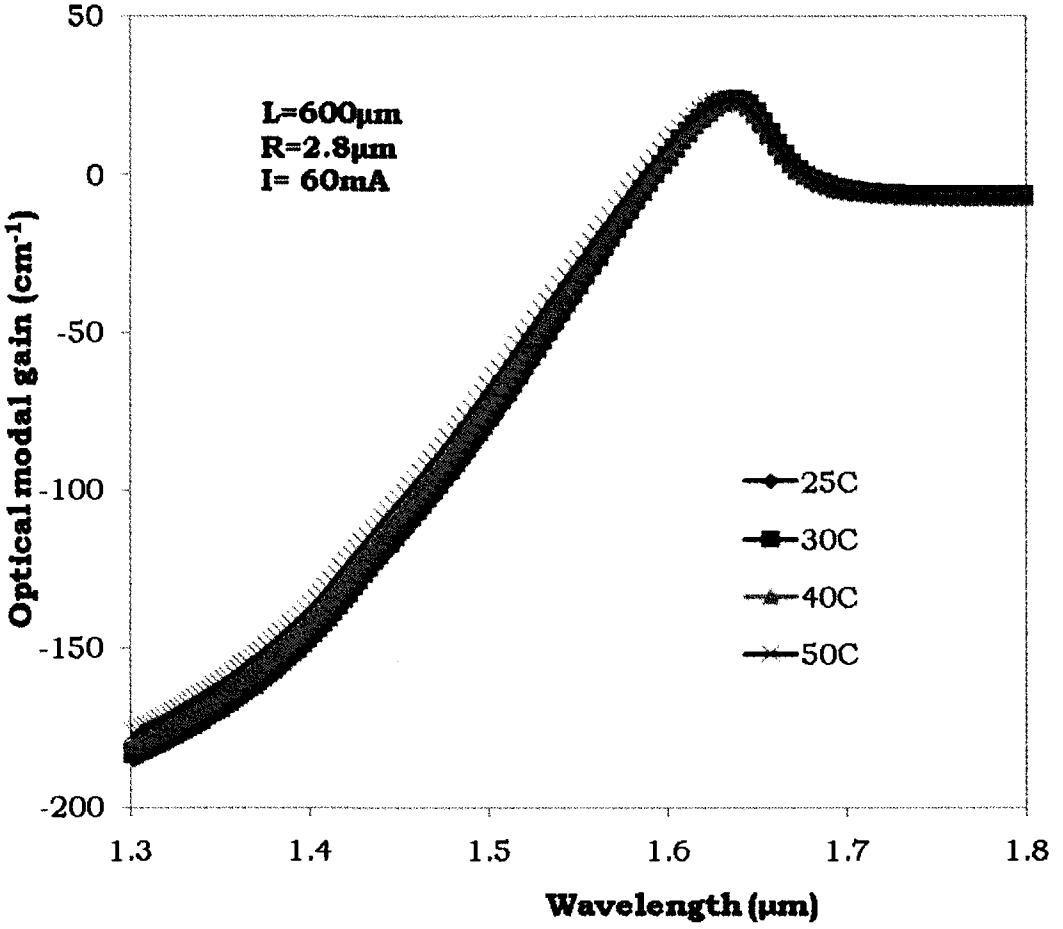

Fig. 5-12 Modal gain spectra calculated by Las2D at four operating temperatures.

Fig. 5-12 shows the gain spectra of the InAlGaAs laser at different operating temperatures with the peak at the 1650 nm wavelength. The laser emission wavelength increases with temperature, the red-shift of the gain peak as a function of temperature is determined to be 0.38 nm/°C. This temperature tuning rate is very low and almost unobservable when compared to the rate of shift in the experimental result.

Las2D does not take into account junction self-heating effect, unlike the gain experimental measurements which included the current-induced junction heating since the laser was biased at different currents. Therefore it seems LAS2D does not completely solve the thermal model of the lasers. This poor temperature gain shift is also reported by another LAS2D user when simulating the GaInNAs laser[15].

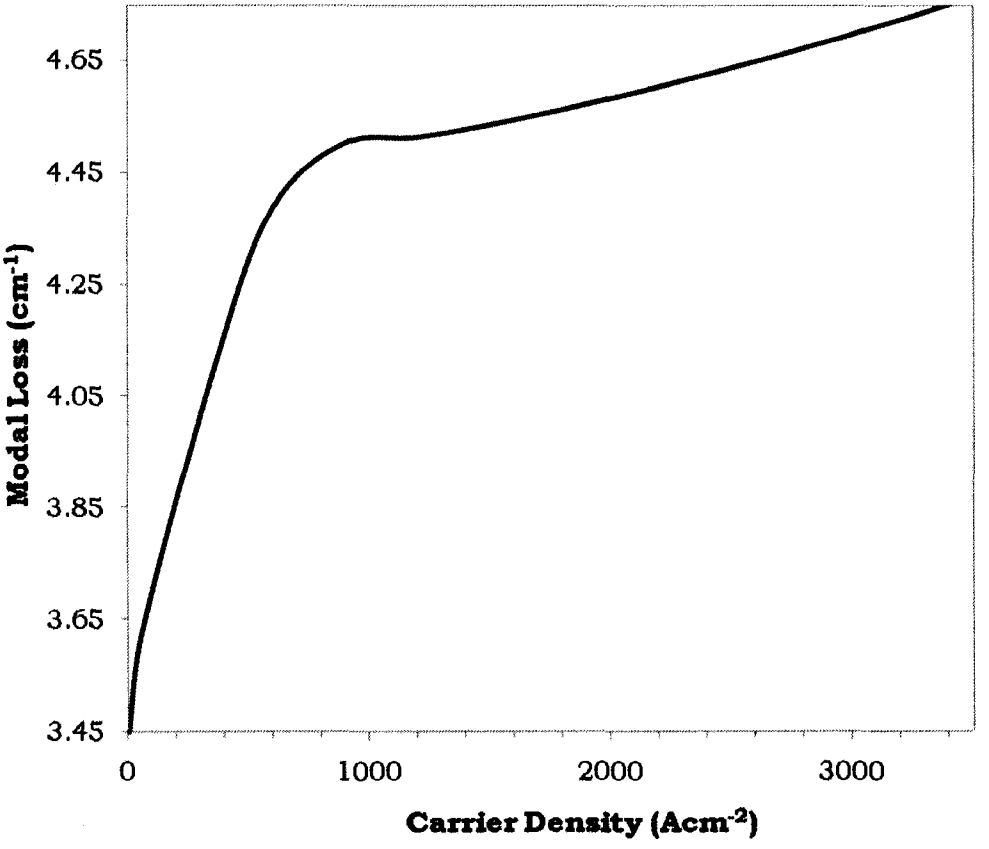

Fig. 5-13 Modal optical loss as a function of the carrier density

Fig. 5-13 shows the internal loss which is calculated in Las2D by integration of the free carrier and scattering loss times the optical intensity. The lower optical loss observed in the simulation as compared

to experimental results could be as a result of the way LAS2D calculates its thermal model, and also because the calculation of its model loss does not include the mirror loss.

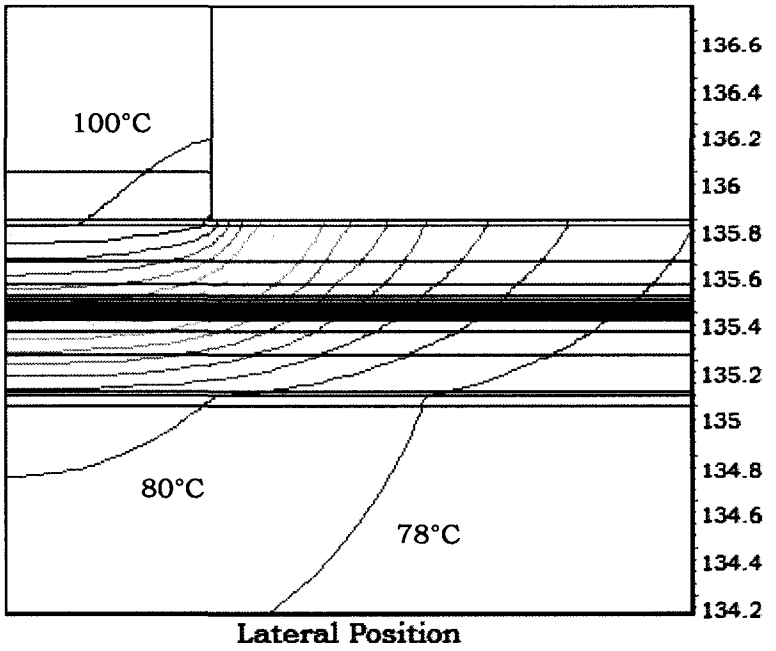

Fig. 5-14 Temperature distribution within the laser device at 60°C.

Fig. 5-14 displays the temperature distribution at 60°C. The active region temperature increase is about ΔT 40°C above the operating temperature and dissipates outwards. This high temperature difference could be due to other heating effects such as the recombination heat and optical absorption heat in the QWs as well as heating in the doped layers surrounding it.

This heating can explain the roll-offs observed in the experimental L-I curves. This can also explain why the optical modal gain red-shift as a function of temperature in Fig. 5-12 does not agree with what is observed

experimentally since the inside of the device structure is hotter. This self heating can reduce the gain of the QW and subsequent degradation of the device if it does not have a good characteristic temperature.

5.9.5 Geometry Dependent Simulation

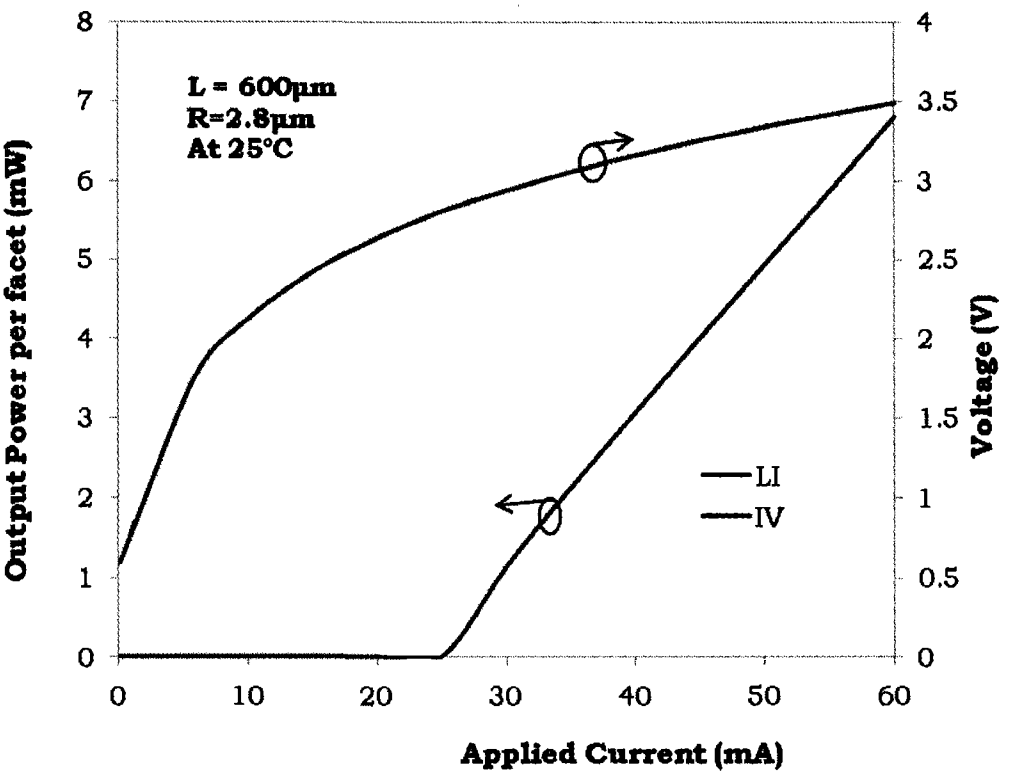

Fig. 5-15 The L-I-V characteristics for the 2.8 x 600 μm laser device at 25°C.

Fig. 5-15 shows the L-I-V characteristic for a 2.8 x 600 μm laser with a threshold current of 25 mA. This relationship is comparable with the experimental data but with a higher output power and better wallplug efficiency. The output power at an applied current of 60 mA is 6.79 mW with a voltage of 3.49 V. Therefore, for the electrical input power of 209 mW, the wallplug efficiency is 3.2% for a single facet and 6.5% for both

facets. The simulation result indicates that lower optical loss laser devices have better output power.

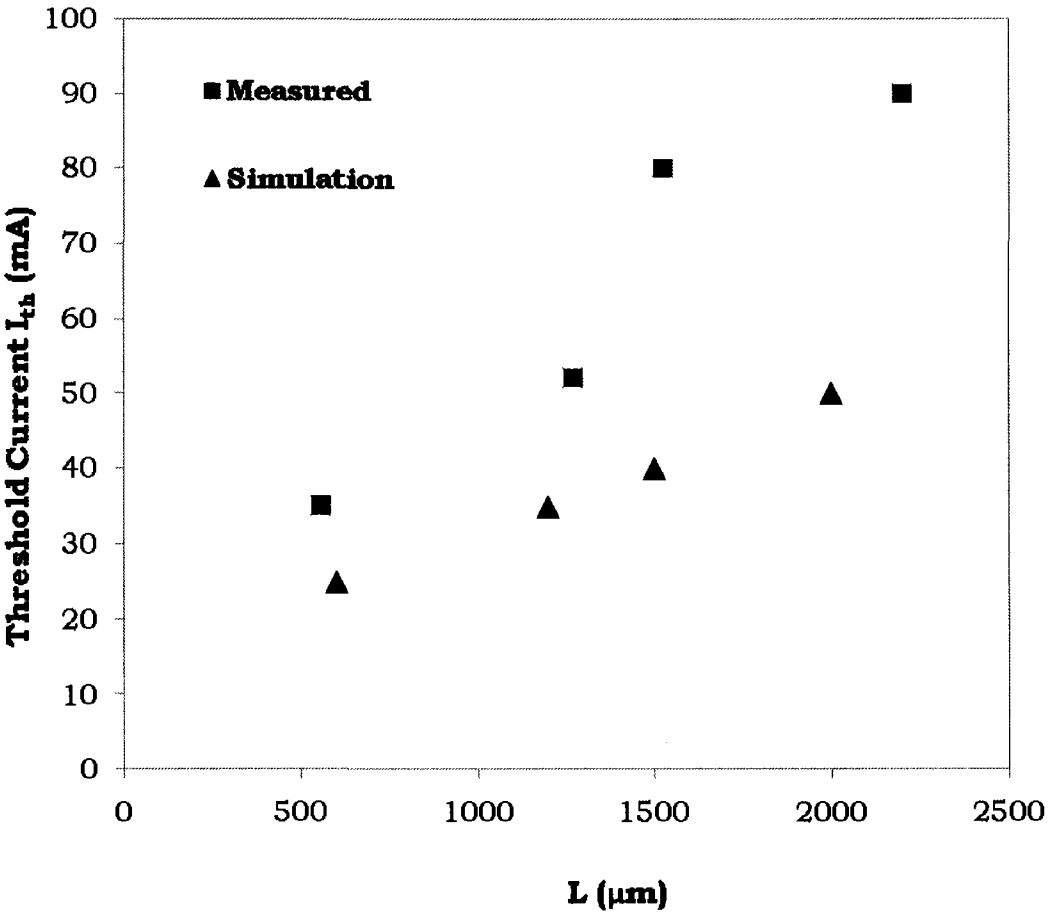

Fig. 5-16 Threshold current as the function of cavity length for several cavity lengths showing the comparison between the measured and simulation results.

Fig. 5-16 shows the threshold current increases linearly with the cavity length since longer cavity length lasers require more time before lasing. The measured data is higher than the simulation data; this could be due to the lower calculated losses in the simulation data. Nonetheless, we observe the same trends for both measured and simulation data

5.10 Conclusions

This chapter presented the modeling of quaternary InAlGaAs material for laser simulations which take into account band gap energy engineering. The electron-hole recombination includes various physical mechanisms that are categorized as radiative recombination (spontaneous and stimulated) and non-radiative recombination (mainly from Auger and Shockley-Read-Hall recombination). The total recombination rate is the sum of all recombination rates that involve electrons. Material parameters are temperature dependent because of the changes that occur to the band gap (shrinkage) due to changes in temperature.

This chapter also used the LAS2D software to simulate the characterized InAlGaAs laser. The energy band diagram analysis confirms a large conduction band offset which is typical of InAlGaAs lasers. The InAlAs claddings and InAlGaAs separate confinement layers provide large potential steps to ensure carrier confinement in the QW region. The recombination mechanisms that consume most of the injection carriers below and above threshold are analyzed with the radiative spontaneous emission dominating below threshold and stimulated emission dominating above threshold. The high purity laser materials only allow for low SRH and Auger recombinations.

The simulation result agrees to a certain degree with the experimental result, their difference can be because of the method LAS2D uses to calculate its material models especially the gain and temperature models, it can also be due to measurement error in the experiment. For the

experimental and simulation results that do not completely agree, there is however a strong trend. The temperature distribution shows strong self heating in the QW region close to the ridge which is higher than the operating temperature implying the need for a heat sink to dissipate the heat in order to preserve the quality and functionality of the laser device. The threshold current increases linearly with injection current and the red-shift of the emission wavelength is observed as the bias current increases with threshold lasing starting at 1648 nm wavelength.

Chapter 6 Conclusions and Future Work

6.1 Introduction

The conclusion chapter presents an overall summary of the research work carried out based on the materials presented in previous chapters. The chapter summarizes the experimental and simulation results and draws conclusions based on the analysis.

The chapter also discusses the future work based on exploring the design improvement of the InAlGaAs laser with focus on threshold current reduction and gain enhancement and better output power.

6.2 Summary

This thesis studied the characterization and design of long wavelength indium aluminium gallium arsenide (InAlGaAs) lattice-matched to indium phosphide (InP) diode laser emitting between 1.65 to 1.7 μm in wavelength. This could be the longest wavelength range possible for the material system. The active region of one laser diode sample consists of six $In_{0.69}Ga_{0.31}As$ quantum wells (1.0% compressive strain) and seven $In_{0.52}Al_{0.36}Ga_{0.12}As$ unstrained barriers. The lasers are grown using digital alloy molecular beam epitaxy (MBE), this technique uses lattice-matched binary/tenary superlattices to achieve high quality tenary and quartenary alloys

In this thesis, the material and the geometrical parameters of the InAlGaAs/InP MQW lasers have been studied through experimental

measurements and simulations. The dependence of these parameters on the various cavity lengths, ridge widths and temperature is evaluated.

The lasers L-I characteristics shows that the threshold current increase with cavity lengths and ridge widths with thermal roll-off occurring at higher injection currents due to self-heating of the laser device. The slope efficiency as well as external differential quantum efficiencies increases for different ridge widths within the same cavity length laser device but decreases with increase in cavity length.

The temperature analysis shows that longer cavity length lasers exhibits better temperature characteristic than the shorter cavity length laser devices indicating the better thermal stability of the longer cavity length lasers. Temperature variations also affected the output power with thermal roll-off occurring at higher temperatures. Increase in threshold current was observed as well as continual decrease in the slope efficiency and the external differential quantum efficiency for increasing temperature. All these confirm the general degradation of laser devices at high temperatures.

The optical spectrum exhibits red-shifting of the emission wavelength due to gain shift which occurs because of band gap reduction with increasing carrier injection, the peak wavelength also exhibits weak mode hopping due optical/index variation with temperature. All these shows the InAlGaAs laser under investigation lases between the 1648 to 1700 nm wavelength with exception to the OSA limit range of 1700 nm.

The band diagram analysis using Las2D simulation tool shows a large conduction band offset which is typical of InAlGaAs lasers. The various recombination mechanisms that consume the injection carriers below and above threshold are analyzed and the concentration of carrier

density in the QW region is explicitly shown. The optical modal gain and the red-shift of the emission wavelength at increasing bias current is studied and shows agreement with the experimental results to a certain degree. The temperature distribution shows a higher temperature in the active region than the operating temperature due to self heating thus requiring a form of heat dissipation, using a heat sink will work to maintain the functionality of the laser device.

6.3 Recommendation

The same laser should be re-designed, fabricated and characterized with the following considerations in mind.

6.3.1 Laser Design Optimization

Considerations for laser design improvement will include intensive theoretical and research studies in quantum well and band gap engineering, doping as well as strain effects for an optimized laser device. Several design variations should also be explored.

An efficient carrier injection and good carrier confinement can be achieved with a band structure that has good material combination of quantum wells and barriers, studies should be carried on varying the present material combination such as designing the same material combination for both the QWs and barriers (the present structure has different material systems). Changes in the doping levels and layer thicknesses of other layers should be considered. Increasing the doping near the active region might reduce the resistance and subsequent self-heating of the device. Limits on the size of both the cavity lengths and

ridge widths for thermal stability should be evaluated. Larger ridge widths as opposed to the very narrow ones used in this thesis should be considered because this will allow heat to dissipate from the device easily thereby reducing threshold current. Using graded layers to ease the transition between the highly p-doped upper layer and the layer below to the barrier layer will reduce the dynamic resistance[61].

The low output power observed can be improved by using anti-reflection coated laser devices to replace the cleave-cleave facet laser devices measured in the thesis. With this in mind, the back facet reflectivity can be modified with higher reflectivity value than the front facet.

Differences in the threshold current as well as efficiencies measured and calculated performance indicate that further refinement on crystal growth conditions could also lead to performance improvement.

All these and more can produce a better performance InAlGaAs laser if specific requirements are in view such as adequate output power, low threshold operation and a good differential gain.

6.3.2 Experimental Improvement

The experimental setup used is standardized but I would recommend using an optical spectrum analyzer that is not limited by the 1700 nm range in which most OSAs are known. This will enable us see how far into the infra-red region the laser will emit.

It is to be noted that InGaAsP/InP based longer wavelength lasers (>1.6 μm) are known to have longer material losses than their shorter

wavelength counterpart[62]. Larger losses are also observed here for InAlGaAs/InP laser devices compared with what has been published in the literature for 1.3 and 1.55 μm devices. A more detailed study should be done to confirm the origin of these larger losses for long wavelength InAlGAs/InP lasers but with improved fabricated laser devices for conclusive report.

Appendix

The LAS2D code below is the basic simulation code but modified to fit different simulations such as changing the cavity length, ridge width, temperature and bias points.

Other LAS2D parameters that were experimented with to get optimal results were the heat models, waveguide core doping, Auger recombination coefficients "cn", "cp" "taun" and "taup", the gain "fgain" or "tau_in" and the loss parameters "alfn", "alfp", "alfvb" and "alfa_scat". All the material parameters used are defined in the LAS2D user guide reference

Note: The Optical model type is fp-half, implying that only the right half of the laser is simulated to save computing time and memory. However, it solves for the whole structure because it assumes a two-dimensional Fabry-Perot laser which has a symmetric structure with respect to its center[57].

LAS2D Code

```
% Julie Nkanta 2008
% 6QW_5nm, 7Barriers_10nm FP structure
% layers: InP, InAlAs, InGaAs, InGaAlAs
% -1.0 pct (compressive QW)
%  In(1-x)Ga(x)As(y)P(1-y) and In(1-x-y)Ga(x)Al(y)As
%-------------------------------------------------------------------------
%
/global
    temp= 298.0      length=600d0
```

```
    taun= 4.0d-8     taup= 4.0d-8
    mesh_dens= 2     lambda= 1.65
    alfa_scat=2.0    fan=1.0
    fup= 1.0         fap=1.0
    faugern=1.0      faugerp=1.0
    front_facet=0.32  rear_facet=0.32
    default_mater=   InGaAlAs
%-------------------------------------------------------------------------------
/heat
    Model= non-isothermal
%-------------------------------------------------------------------------------
/ionization
  incomplete= Yes  d_degf= 2.0d0  Ed= 0.010  a_degf= 4.0d0  Ea= 0.010
%-------------------------------------------------------------------------------
/mobility
  n_model = field  exp_un=-0.5 p_model = field  exp_up=-3
%-------------------------------------------------------------------------------
%  Layer definition
%-------------------------------------------------------------------------------
%  Ridge layers
%  P-doped InGaAs layer
/layer  mater=InGaAlAs   thickness=  0.200
  /rect dop=  1.0d19   x=0.47      y= 0.0000
  /rect oxide_eps=2.25 thermal_cond= 0.014
%
% P-doped InP layer
/layer  mater=InGaAsP   thickness=  1.4000
  /rect dop=  1.0d18   x= 0.0000 y= 0.0000
  /rect oxide_eps=2.25 thermal_cond= 0.014
%
% P-doped InP layer
/layer  mater=InGaAsP   thickness=  0.2000
  /rect dop=  6.0d17   x= 0.0000 y= 0.0000
  /rect oxide_eps=2.25 thermal_cond= 0.014
%
% P-doped InP layer
/layer  mater=InGaAsP   thickness=  0.0250
```

```
  /rect dop=  4.0d17    x= 0.0000 y= 0.0000
  /rect dop=  4.0d17    x= 0.0000 y= 0.0000
%
% P-doped InAlAs layer
/layer   mater=InGaAlAs    thickness=   0.1500
 /rect dop=  5.0d17    x=0.000    y= 0.480000
 /rect dop=  5.0d17    x=0.000    y= 0.480000
%-------------------------------------------------------------------------------
% Upper cladding
% P-doped InGaAlAs layer
/layer   mater=InGaAlAs    thickness=   0.1000
  /rect dop=  5.0d17    x= 0.0800 y= 0.4000
  /rect dop=  5.0d17    x= 0.0800 y= 0.4000
%-------------------------------------------------------------------------------
% Laser WG core
% InGaAlAs layer
/layer   mater=InGaAlAs    thickness=   0.0500
  /rect dop= 0 x= 0.0800     y= 0.4000
  /rect dop= 0 x= 0.0800     y= 0.4000
%
%  Barrier 7
/layer   mater=InGaAlAs    thickness=   0.0100
  /rect dop= 0 x= 0.1200     y= 0.3600
  /rect dop= 0 x= 0.1200     y= 0.3600
%
% QW6
/layer   mater=InGaAlAs    thickness=   0.0050
  /rect dop= 0 x= 0.3100     y= 0.0000 qw= Yes
  /rect dop= 0 x= 0.3100     y= 0.0000 qw= Yes
%
%  Barrier 6
/layer   mater=InGaAlAs    thickness=   0.0100
 /rect dop= 0 x= 0.1200     y= 0.3600
 /rect dop= 0 x= 0.1200     y= 0.3600
%
% QW5
/layer   mater=InGaAlAs    thickness=   0.0050
```

```
  /rect dop= 0 x= 0.3100    y= 0.0000 qw= Yes
  /rect dop= 0 x= 0.3100    y= 0.0000 qw= Yes
%
%  Barrier 5
/layer  mater=InGaAlAs  thickness=  0.0100
  /rect dop= 0 x= 0.1200    y= 0.3600
  /rect dop= 0 x= 0.1200    y= 0.3600
%
% QW4
/layer  mater=InGaAlAs  thickness=  0.0050
  /rect dop= 0 x= 0.3100    y= 0.0000 qw= Yes
  /rect dop= 0 x= 0.3100    y= 0.0000 qw= Yes
%
%  Barrier 4
/layer  mater=InGaAlAs  thickness=  0.0100
  /rect dop= 0 x= 0.1200    y= 0.3600
  /rect dop= 0 x= 0.1200    y= 0.3600
%
% QW3
/layer  mater=InGaAlAs  thickness=  0.0050
  /rect dop= 0 x= 0.3100    y= 0.0000 qw= Yes
  /rect dop= 0 x= 0.3100    y= 0.0000 qw= Yes
%
%  Barrier 3
/layer  mater=InGaAlAs  thickness=  0.0100
  /rect dop= 0 x= 0.1200    y= 0.3600
  /rect dop= 0 x= 0.1200    y= 0.3600
%
% QW2
/layer  mater=InGaAlAs  thickness=  0.0050
  /rect dop= 0 x= 0.3100    y= 0.0000 qw= Yes
  /rect dop= 0 x= 0.3100    y= 0.0000 qw= Yes
%
%  Barrier 2
/layer  mater=InGaAlAs  thickness=  0.0100
  /rect dop= 0 x= 0.1200    y= 0.3600
  /rect dop= 0 x= 0.1200    y= 0.3600
```

```
%
% QW1
/layer  mater=InGaAlAs   thickness=  0.0050
  /rect dop= 0 x= 0.3100    y= 0.0000 qw= Yes
  /rect dop= 0 x= 0.3100    y= 0.0000 qw= Yes
%
%  Barrier 1
/layer  mater=InGaAlAs   thickness=  0.0100
  /rect dop= 0 x= 0.1200    y= 0.3600
  /rect dop= 0 x= 0.1200    y= 0.3600
%
% InGaAlAs layer
/layer  mater=InGaAlAs   thickness=  0.0500
  /rect dop=  0   x= 0.0800 y= 0.4000
  /rect dop=  0   x= 0.0800 y= 0.4000
%-------------------------------------------------------------------------
%Lower cladding
% n-doped InGaAlAs layer
/layer  mater=InGaAlAs   thickness=  0.1000
  /rect dop= -5.0d17   x= 0.0800 y= 0.4000
  /rect dop= -5.0d17   x= 0.0800 y= 0.4000
%
% n-doped InAlAs layer
/layer  mater=InGaAlAs   thickness=  0.1500
  /rect dop= -5.0d17   x= 0.0000 y= 0.4800
  /rect dop= -5.0d17   x= 0.0000 y= 0.4800
%
% n-doped InGaAlAs layer
/layer  mater=InGaAlAs   thickness=  0.0200
  /rect dop= -1.0d18   x= 0.0800 y= 0.4000
  /rect dop= -1.0d18   x= 0.0800 y= 0.4000
%-------------------------------------------------------------------------
% Buffer
% n-doped InP
/layer  mater=InGaAsP   thickness=  0.0500
  /rect dop= -1.0d18   x=0.0000 y= 0.0000   thermal_cond=0.6
  /rect dop= -1.0d18   x=0.0000 y= 0.0000   thermal_cond=0.6
```

```
%-------------------------------------------------------------------------
% Substrate
%InP
/layer  mater=InGaAsP   thickness=   135.0000
  /rect dop=  -1.0d18   y=0.0000   thermal_cond=0.6
  /rect dop=  -1.0d18   y=0.0000   thermal_cond=0.6
%-------------------------------------------------------------------------
/qw-data
      B0= 1.0e-10      exp_rad= -1.5
      cn= 1.0e-30     cp= 1.0e-30     t_augern= 350     t_augerp= 350
      alfn= 3.0e-18    alfp= 7.0e-18    alfvb= 5.0e-18
      t_alfn= 325      t_alfp= 325      t_alfvb= 325
%-------------------------------------------------------------------------
/qw-gain
    model= Asada         fgain= 1.00
    tau_in= 0.10e-12     exp_tin= -2.0
%-------------------------------------------------------------------------
% x-mesh
/columns
      width=    1.400   dxmin= 0.020  dxmax= 0.100
      width=    7.000   dxmin= 0.020  dxmax= 0.500   Fine= Left
%-------------------------------------------------------------------------
/contacts  toplx= 0.0   toprx= 1.400
%-------------------------------------------------------------------------
/Optical-Model
          Type= fp-half
%-------------------------------------------------------------------------
/bias
    V=  0.6 0.7 0.8 0.85
    I=  1.0 6.0 10.0:5.0:60.0
%-------------------------------------------------------------------------
```

References

[1] P. Bhattacharya, "Semiconductor Optoelectronic Devices," Prentice hall, Second Edition, 1997

[2] J. C. L. Yong, J. M. Rorison, I. H. White, "1.3-μm Quantum-Well InGaAsP, AlGaInAs, and InGaAsN Laser Material Gain: A Theoretical Study," IEEE J. Quantum Electron., Vol. 38, No. 12, 1553-1564, 2002.

[3] A. Villeneuve, M. Sundheimer, N. Finlayson, G. I. Stegeman, S. Morasca, C. Rigo, R. Calvani, C. De Bernardi, "Two-photon absorption in In1-x-yGaxAlyAs/InP waveguides at communications wavelengths," Appl. Phys. Lett., Vol. 56, No. 19, 1865-1867, 1990.

[4] R. Rajasekaran "Dependence of LASER Performance on Number of Quantum Wells in InAlGaAs Semiconductor LASERS" Masters Thesis, Department of Electrical and Computer Engineering and Computer Science of the College of Engineering, University of Cincinnati, February 2006

[5] J. O'Gorman, A. F. J. Levi, T. Tanbun-Ek, D. L. Coblentz, and R. A. Logan, "Temperature Dependence of Long Wavelength Semiconductor Lasers", Oct. 1992

[6] K. Prosyk, J. G. Simmons, and J. D. Evans, "Well number, length, and temperature dependence of efficiency and loss in InGaAsP-InP compressively strained MQW ridge waveguide lasers at 1.3 μm," IEEEJ. Quantum Electron., vol. 33, pp. 1360–1368, 1997

[7] A. J. SpringThorpe, M. Extavour, D. Goodchild, E. M. Griswold, G. Smith, J. K. White, K. Hinzer, R. Glew, R. Williams, F. Robert "A forbidden temperature region for the growth of planar strained InAlGaAs MQW structures for 1.3 μm lasers" Journal of Crystal Growth 251, pp760–765, 2003

[8] A. J. SpringThorpe, T. Garanzotis, P. Paddon, G. Pakulski, J. K. White "Strained 1.3 μm AlGaInAs MQW laser grown by digital alloy MBE" Elect Lett Vol 36 No 12, pp1031-1032, June 8 2000

[9] J. I. Davies, A. C. Marshall, M. D. Scott, and R. J. M. Griffiths, "Structural and optical properties of GaAlInAs lattice matched to InP grown by low-pressure metalorganic vapor phase epitaxy", Applied Physics Letters, Vol. 53, No. 4, p276-278, July 1988

[10] J. Piprek, P. Abraham, and J. E. Bowers, "Self-consistent analysis of high-temperature effects on strained-layer multi-quantum well InGaAsP/InP lasers," IEEE J. Quantum Electron., vol. 38, pp. 366–374, Mar. 2000.

[11] D. Olego, T. Y. Chang, E. Silberg, E. A. Caridi, and A. Pinczuk, "Compositional dependence of band-gap energy and conduction-band

effective mass of In1-x-yGaxAlyAs lattice matched to InP", Applied Physics Letters, Vol. 51, No. 5, p476-478, 1982.

[12] M. Jain, J. Roberts, and C. N. Ironside "Analysis of the gain distribution across the active region of InGaAs-InAlGaAs multiple quantum well lasers." IEE Proceedings in Optoelectronics 152:pp. 209-214. 2005

[13] O. Issanchou, J. Barrau, E. Ediart-Alhor, and M. Quillec, "Theoretical comparison of GaInAs/GaAlInAs and GaInAs/GaInAsP quantum-well lasers", Journal of Applied Physics, Vol. 78, No. 6, p3925-3930, September 1995

[14] J Piprek ""Semiconductor Optoelectronic Devices: Introduction to Physics and Simulation" Academic Press, San Diego, 2003

[15] X. Zhang "Dilute Nitride Long Wavelength Semiconductor Diode Lasers" PhD Thesis, Ottawa-Carleton Institute for Electrical and Computer Engineering, University of Ottawa. March 2007

[16] I. Vurgaftman, J.R. Meyer, and L.R. Ram-Mohan, "Band parameters for III-V compound semiconductors and their alloys", J. Appl. Phys., Vol. 89, pp. 5815-5875, 2001.

[17] S. Y. Hu, S. W. Corzine, K.-K. Law, D. B. Young, A. C. Gossard, L. A. Coldren, and J. L. Merz, "High-efficiency and low-threshold InGaAs/AlGaAs quantum-well lasers" J. Appl. Phys. **76**, 4479 (1994)

[18] M. Legge, G. Bacher, S. Bader, A. Forchel, H.-J. Lugauer, A. Waag, and G. Landwehr, "Strongly index-guided II-VI laser diodes" IEEE Photonics Technol. Lett. **12**, 236 (2000)

[19] D. Ban, E. H, Sargent, K. Hinzer, St. J. Dixon-Warren, A. J. SpringThorpe, J. K. White "Direct observation of lateral current spreading in ridge waveguide lasers using scanning voltage microscopy" J. Appl. Phys. Lett. 82, 4166 (2003)

[20] M. Achtenhagen and A. Hardy, "Lateral current spreading in ridge waveguide laser diodes" Appl. Phys. Lett. **74**, 1364 (1999)

[21] J. Piprek, J. K. White, and A. J. SpringThorpe, "What Limits the Maximum Output Power of Long-Wavelength AlGaInAs/InP Laser Diodes" J. Quantum Electron. **38**, 1253 (2002)

[22] G. H. B. Thompson, Physics of Semiconductor Laser Devices, Chichester, Wiley, (1980)

[23] G. J. Letal, J.G. Simmons, J.D. Evans, and G.P. Li, "Determination of active-region leakage currents in ridge-waveguide strained-layer quantum-well lasers by varying the ridge width", IEEE J. Quantum Electron., Vol. 34, pp. 512-518, 1998.

[24] L. A. Coldren and S. W. Corzine, Diode Lasers and Photonic Integrated Circuits (New York, NY: John Wiley & Sons, Inc., 1995),

[25] N. Tessler, and G. Eisenstein "On Carrier Injection and Gain Dynamics in Quantum Well lasers," IEEE J. Quantum Electron. vol. 29, pp. 1586-1596. Jun. 1993

[26] K. S. Mobarhan "Test and Characterization of Laser Diodes: Determination of Principal Parameters" 1996-2008, Newport Inc. USA

[27] B. W. Hakki and T. L. Paoli, "CW degradation at 300°K of GaAs double-heterostructure junction lasers. II. Electronic gain", J. Appl. Phys., Vol. 44, pp. 4173, 1973.

[28] D. T. Cassidy "Comparison of rate-equation and Fabry-Perot approaches to modeling a diode laser", Appl. Opt., Vol. 22, pp. 3321-3326 , 1983.

[29] N. Tessler, and G. Eisenstein "On Carrier Injection and Gain Dynamics in Quantum Well lasers," IEEE J. Quantum Electron. vol. 29, pp. 1586-1596. Jun. 1993

[30] W. Rideout, W. F. Sharfin, E. S. Koteles, M. 0. Vassell, and B. Elman. "Well barrier hole burning in quantum well lasers." IEEE Photon. Technol. Lett., vol. 3, pp. 784-786, Sept. 1991

[31] S. C. Kan, D. Vassilovski. T. C. Wu, and K. Y. Lau. "On the effects of carrier diffusion and quantum capture in high speed modulation of quantum well lasers," Appl. Phgs. Lett., vol. 61, pp. 752-754, 1992

[32] S. L. Chuang, "Physics of Optoelectronics devices", John Wiley & Sons Inc., New York, 1995.

[33] S. D. Hersee, B. de Cremoux, J. P. Duchemin, "Some characteristics of the GaAs/GaAlAs graded-index separate-confinement heterostructure quantum well laser structure" Appl. Phys. Lett 44, 476 (1984)

[34] E. P. O'Reilly and M. Silver, "Temperature sensitivity and high temperature operation of long wavelength semiconductor lasers", Sep.1993

[35] X. H. Zhang, S. J. Chua, S. J. Xu, W. J. Fan, "Band offsets at the InAlGaAs/InAlAs (001) heterostructures lattice matched to an InP substrate", Journal of Applied Physics, Vol.83, No. 11, p5852-5854, June 1998.

[36] M. Jain "An investigation of broad gain spectrum InGaAs/InAlGaAs quantum well lasers lattice matched to InP" PhD Thesis, Faculty of Engineering, University of Glasgow, UK 2002

[37] J. Minch, S.H. Park, T. Keating, and S.L. Chuang, "Theory and Experiment of In1-xGaxAsyP1-y and In1-x-yGaxAlyAs long-wavelength Strained Quantum-well lasers", IEEE Journal of Quantum Electronics, Vol. 35, No. 5, p771-782, May 1999

[38] E. H. Li, "Material parameters of InGaAsP and InAlGaAs systems for use in quantum well structures at low and room temperature", Physica E 5, p215-273, November 1999.

[39] S. R. Selmic, T.M. Chou; J. Sih, J.B. Kirk, A. Mantle, J.K. Butler, D. Bour, G.A. Evans," Design and characterization of 1.3-μm AlGaInAs-InP multiple-quantum-well lasers", IEEE Journal of selected topics in Quantum Electronics, Vol. 7, No. 2, pp.340 – 349, March-April 2001

[40] J-W Pan, and J-I Chyi, "Theoretical Study of the Temperature Dependence of 1.3mm AlGaInAs-InP Multiple-Quantum-Well Lasers", IEEE Journal of Quantum Electronics, Vol. 32, No. 12, p2133-2138, December 1996.

[41] W. J. Keeler, G. A. Keeler, and D. A. Harrison, "Raman investigation of molecular beam epitaxy grown InGaAlAs epilayers lattice matched to InP for low Al concentrations", Journal of Applied Physics, Vol. 83, No. 4, p2266-2271, February 1998.

[42] E. Yablonovitch and E. O. Kane, "Band structure engineering of semiconductor lasers for optical communications," J. Lightwave Technol., vol. 6, no. 8, pp. 1292-1299, 1988

[43] J. Piprek, P. Abraham, and J. E. Bowers, "Self-consistent analysis of high-temperature effects on strained-layer multi-quantum well InGaAsP/InP lasers," IEEE J. Quantum Electron., vol. 38, pp. 366–374, Mar. 2000.

[44] Y. Zhang, W. Chen, A. Wang, H. Jiang, C. Liu, and S. Liu, "Design of the Active Structure of High-Performance 1.55-_m In1 x yGayAlxAs Strained MQW Lasers," IEEE J. Quantum Electron., vol. 37, NO. 7, pp. 923–927, July 2001.

[45] G. J. Letal, J. G. Simmons, J. D. Evans, and G. P. Li, IEEE J. Quantum Electron. 34, 512 (1998)

[46] G. Belenky, L. Shterengas, C. L. Reynolds, Jr., M. W. Focht, M. S. Hybertsen, and B. Witzigmann, IEEE J. Quantum Electron. **38**, 1276 ~2002!.

[47] D. Ban, E. H. Sargent, K. Hinzer, St. J. Dixon-Warren, A.J SpringThorpe, J. K. White "Direct observation of lateral current spreading in ridge waveguide lasers using scanning voltage microscopy" Appl. Phys. Lett Vol 82, Number 23 9 June 2003

[48] M. Jain, J. Roberts, and C. N. Ironside "Analysis of the gain distribution across the active region of InGaAs-InAlGaAs multiple quantum well lasers." IEE Proceedings in Optoelectronics 152:pp. 209-214. 2005

[49] M. Jain, C. N Ironside "Internal Optical Loss Measurements in InGaAs–InAlGaAs Quantum-Well Lasers Operating Around 1550 nm." IEEE Photonics Technology Letters, VOL. 15, NO. 5, 152:pp. 631-633. May 2003

[50] T. J Houle, J. C. L. Yong, C. M. Marinelli, S. Yu, J.M. Rorison, I. H. White, J. K. White, "Characterization of the temperature sensitivity of gain and recombination mechanisms in 1.3-μm AlGaInAs MQW lasers" IEEE J. Quantum Electron., vol. 41, Issue 2, pp. 132–139, February 2005

[51] N. Tessler and G. Eisenstein, "Distributed nature of quantum well lasers," Appl. Phys. Lett., Vol. 63, pp. 10-12, 1993.

[52] A. Hangleiter, A. Grabmaier, and G. Fuchs, "Damping of the relaxation resonance in multiple-quantum-well lasers by slow interwell transport", Appl. Phys. Lett., Vol. 62, pp. 2316-2318, 1993.

[53] D. T. Cassidy, "Technique for measurement of the gain spectra of semiconductor diode lasers", J. Appl. Phys., Vol. 56, pp. 3096, 1984.

[54] H. Wang, D.T. Cassidy, "Gain measurements of Fabry-Perot semiconductor lasers using a nonlinear least-squares fitting method.", IEEE J. Quantum Electron., Vol. 41, pp. 532-540, 2005.

[55] B. W. Hakki and T.L. Paoli, "Gain spectra in GaAs double-heterostructure injection lasers", J. Appl. Phys., Vol. 46, pp. 1299-1302, 1975.

[56] K. S. Mobarhan "Test and Characterization of Laser Diodes: Determination of Principal Parameters" 1996-2008, Newport Inc. USA

[57] A. Champagne and R. Maciejko, Las2D users manual, The Optoelectronic Laboratory, Ecole Polytechnique de Montreal, 2006.

[58] M. Sotoodeh, A.H. Khalid, and A.A. Rezazadeh, "Empirical low-field mobility model for III-V xompounds applicable in device simulation codes", J. Appl. Phys., Vol.87, pp. 2890-2900, 2000.

[59] M.L. Cohen and J.R. Chelikowsky, Electronic Structure and Optical Properties of Semiconductors, Springer Series in Solid-State Sciences, Springer, Berlin, 1998

[60] R. Yan, S. Corzine, L. Coldren, and I. Suemune, "Corrections to the expression of gain in GaAs", IEEE J. Quantum Electron., Vol.26, pp. 213-216, 1990.

[61] A. Champagne, "RE: LAS2D", Email Communication, The Optoelectronic Laboratory, Ecole Polytechnique de Montreal, August 2008.

[62] K. Hinzer, "Private Communication" School of Information Technology and Engineering, University of Ottawa, August 2008